Distributions of Gas and Galaxies From Galaxy Clusters to Larger Scales

Distributions of Gas and Galaxies from Galaxy Clusters to Larger Scales

A dissertation presented

by

Anna Patej

to

The Department of Physics

in partial fulfillment of the requirements

for the degree of

Doctor of Philosophy

in the subject of

Physics

Harvard University

Cambridge, Massachusetts

April 2016

Dissertation Advisors: Professors Abraham Loeb and Daniel Eisenstein Anna Patej

Distributions of Gas and Galaxies from Galaxy Clusters to Larger Scales

Abstract

This thesis addresses the distributions of baryonic matter on three scales: the outskirts of the gas and galaxy profiles in galaxy clusters, the clustering of galaxies of galaxies on large scales and its relation to the underlying matter distribution, and the extremes of the galaxy distribution: the connections between the most distant galaxies ever discovered and the closest galaxies to our own, the Local Group Dwarfs. We begin with investigations of the outskirts of galaxy clusters, where long-standing analytical models of structure formation as well as recent simulations predict the existence of steep density jumps in the gas (the 'virial shock') and dark matter profiles near the virial radius. We describe a new method for deriving models for the gas distribution in galaxy clusters, which relies on a few basic assumptions — including the existence of the virial shock and a coincident density jump in the dark matter — and show a resulting profile for the gas that is in good agreement both with X-ray observations of cluster interiors and simulations of the outskirts, and requires fewer parameters than the traditional three-parameter β-model.

Recent simulations have strengthened the arguments in favor of the existence of a dark matter density jump, arising from the accumulation of particles at the apocenter of their first orbit. Since cluster member galaxies are expected to follow similar collisionless dynamics as the dark matter, the galaxy density profile should show a steep density

jump as well. We present evidence for a feature consistent with a density jump in galaxy density profiles constructed from photometry from the Sloan Digital Sky Survey and Hectospec (MMT) spectroscopy of cluster members and discuss avenues for probing the density jumps with future data sets.

Moving to larger scales where massive galaxies of different types are expected to trace the same large-scale structure, we present a test of this prediction by measuring the clustering of red and blue galaxies at $z \sim 0.6$ using the CMASS sample of galaxies from the 12th Data Release of SDSS-III. The stochasticity between these two samples is quantified via the correlation coefficient r, which can be constructed from two different statistics. Both statistics indicate that on intermediate scales ($20 \lesssim R \lesssim 100\ h^{-1}$Mpc) there is low stochasticity between the two samples of galaxies, providing a constraint on a key systematic in using large galaxy redshift surveys for cosmology.

In cosmology, dense redshift surveys permit the measurement of the scale of baryon acoustic oscillations (BAO), which appear as a modest amplification at scales of about $R = 105\ h^{-1}$Mpc in the two-point auto-correlation function of galaxies, provided that there is a sufficiently high density of galaxies with accurately measured three-dimensional positions. As a result, due to the expense of spectroscopic observations, to date most BAO analyses have been performed at fairly low redshifts where present surveys can attain the requisite densities without sacrificing efficiency. We present a new method of measuring the BAO using the cross-correlation of a sparse spectroscopic sample with a denser, photometric sample of galaxies that will allow us to extend BAO measurements to higher redshifts than are presently accessible with spectroscopy alone. We discuss applications of this new method to current and upcoming datasets.

Finally, we connect galaxies both near — the Local Group dwarf galaxies — and far — the high-redshift galaxies discovered by space-based observatories like *Hubble* and *Spitzer*. We evolve the local dwarfs back in time using stellar population synthesis code and juxtapose the properties of their ancient selves against those of the galaxies already discovered at high redshift. We additionally compare the properties of the dwarfs' progenitors with the detection limits of the future *James Webb Space Telescope* (*JWST*), finding that *JWST* should be able to detect the progenitors of galaxies similar to a few of the brightest local galaxies.

Contents

Acknowledgments

I am very fortunate to have had my thesis work advised by two wonderful mentors, Abraham (Avi) Loeb and Daniel Eisenstein.

It has been both a privilege and an absolute pleasure to have worked with my advisor Avi Loeb for over three years. Avi's enthusiasm for astrophysics and his wide-ranging interests have been an inspiration to me, as has his incredible mentorship, which has provided a strong foundation for my research career. I am extremely thankful for all of his support and encouragement; his warm and patient guidance made this thesis possible.

It is likewise a pleasure to thank Daniel Eisenstein, my advisor for my more observational endeavors for the past two years. I truly appreciate Daniel's kindness, dedication, and insights, and I am greatly thankful for having had the opportunity to work with him. His detailed and thorough advice has been invaluable to me, and I am very grateful for all the time he has invested in making my graduate career successful.

I would additionally like to thank Doug Finkbeiner and Erel Levine for serving on my thesis committee and providing helpful discussions over the past few years. I also appreciate Jim Moran's encouragement over the course of my graduate career.

I am also very grateful to Arjun Dey and Joan Najita, who have provided a great deal of kindness, support, and encouragement over the past few years. They have made my trips to Tucson extremely fun and memorable, and I am looking forward to joining them and my other Arizona-based collaborators for my next adventure. In addition to Arjun and Joan, as part of my work with the DECam Legacy Survey, I have been extremely fortunate to work with an exceptional group of collaborators. In particular,

I am very grateful to David Schlegel for his excellent advice and support; he and Arjun were extremely welcoming PIs. I have benefited greatly from my interactions with both Arjun and David and hope to continue collaborating with them in future projects. I have also enjoyed having the chance to work with the incredible DECaLS core and observing teams, including Bob Blum, Dustin Lang, Adam Myers, Brian Nord, and Greg Rudnick, as well as a number of other collaborators.

My education in graduate school has also benefited from the insights and support of several other individuals, particularly Brian Stalder, who took me on my first observing run and taught me most of what I know about observing (and photometric redshifts); Maureen Conroy, who led me through the reduction of my Megacam data and helped me set up a Megacam PSF analysis pipeline at Magellan; Matt Bayliss, who was an excellent resource for me in my early work with galaxy clusters and provided extremely helpful feedback on my qualifying exam practice talk; Henk Hoekstra, who kindly hosted me in Leiden for a few weeks while I was working on weak lensing; as well as numerous other faculty, staff, and postdocs with whom I have interacted during my time in graduate school.

I would additionally like to thank the staff of the Physics and Astronomy Departments. In Physics, Jacob Barandes, Lisa Cacciabaudo, Carol Davis, Dayle Maynard, and Jan Ragusa (and Isaac and Magoo) have gone out of their way to help me with various matters and are always willing to listen and chat. In Astronomy, Lisa Catella, Peggy Herlihy, Uma Mirani, Mark Palmer, Robb Scholten, and Nina Zonnevylle have been wonderful resources and have made the Astronomy Department a fantastic second department for me.

My time in graduate school would have been very different if not for the support of many friends and colleagues. In particular, my original Astronomy officemates, Dawn Graninger and Ben Montet, made working in the dreary Tower fun and helped introduce me to the wider Astronomy community, including the CfA Country Club. I am extremely grateful for the friendship of the Astronomy students, as well as the students in Physics and other departments beyond at Harvard. I am also very happy that I could share many memories at Harvard with friends from college and earlier who have joined me here.

Finally, I would like to thank my parents, Barbara and Edward Patej. My parents have always been supportive of me as I have pursued various trajectories that we could not have foreseen when we first moved to the United States in the mid-1990s. None of this would have been possible without their constant love and encouragement.

As a last note, I would also like to thank the various agencies that have provided financial support for my work, the details of which are enumerated in the chapters of this thesis: the National Science Foundation, through the NSF Graduate Research Fellowship Program; the U.S. Department of Energy, through a grant to Daniel Eisenstein; and the Harvard Physics Department, through the Van Vleck Travel Fund.

Chapter 1

Introduction

Optical and infrared observations of the extragalactic sky yield seas of luminous galaxies that exhibit a variety of colors, morphologies, and sizes. The distributions of these galaxies are studied extensively via galaxy redshift surveys such as the CfA Redshift Survey (Geller & Huchra 1989), the Sloan Digital Sky Survey (York et al. 2000), and the 2dF Galaxy Redshift Survey (Colless et al. 2001). These surveys provide the three-dimensional positions of galaxies in the universe and have revealed that galaxies are distributed along filaments, with galaxy clusters — large groups of hundreds to thousands of galaxies — arising at the nodes where the filaments intersect.

At the same time, cosmological investigations have firmly established that baryonic matter, or the ordinary matter that makes up the luminous content of galaxies that these surveys observe[1], comprises only a small fraction — about 5% — of the universe's

[1]It is worth noting that in cosmology, the term "baryons" includes not just protons and neutrons but also electrons, which are actually leptons.

mass-energy density. The vast majority is in the form of dark energy ($\sim 70\%$) and dark matter ($\sim 25\%$) (Ade et al. 2015), two unknown quantities whose natures modern cosmology and astrophysics aim to determine. Dark energy drives the acceleration of the expansion of the universe, whereas dark matter, whose influence is imparted in the form of gravitational attraction, tends to counteract the effect of dark energy on small scales by clumping matter together.

The standard model of cosmological structure formation stipulates that galaxies form in the potential wells of dark matter halos. Accordingly, the filaments of galaxies at large scales are expected to trace massive threads of dark matter, and the galaxy cluster nodes are themselves embedded in dark matter halos. The nodes continue to grow to the present day via the accretion of matter onto the cluster from the filaments and from mergers of clusters, physical processes that, as we shall see, are expected to impart signatures on the outer profiles of clusters.

In what follows, we explore in detail the distributions of matter in these regimes and the questions that they present. We begin in the nodes of the matter distribution, galaxy clusters, which have played a fundamental role in the development of modern astrophysics, and then transition to galaxy distributions on large scales, which are at present one of the primary and most competitive probes of cosmology. Lastly, we consider galaxies at two extremes: the dwarf galaxies that surround the Milky Way and Andromeda on small scales in the Local Group, whose nearness to our galaxy implies that we can attempt detailed studies of stellar contents and star formation histories, and the high-redshift galaxies discovered by the *Hubble Space Telescope* and *Spitzer*, which are the most distant galaxies yet discovered and thus serve as an important means of probing the universe at very early times.

1.1 Clusters of Galaxies

Studies of galaxy clusters have been intertwined with the development of modern cosmology from the outset (for recent, comprehensive reviews of various aspects of galaxy cluster astrophysics and cosmology, see Voit 2005; Allen, Evrard, & Mantz 2011; Kravtsov & Borgani 2012; we will discuss only the most salient aspects here). The first evidence for dark matter came from Swiss astronomer Fritz Zwicky's observations of the nearby Coma Cluster in the 1930s. He found a discrepancy between the mass he estimated from the stellar content of the cluster's constituent galaxies and the mass that he determined from their velocity dispersions and referred to the missing matter as "dark matter," the name it still bears today. While subsequent observations reinforced and continue to support Zwicky's conclusions, some of the missing matter ended up being accounted for in the 1970s with the advent of X-ray astronomy. Results from the first X-ray astronomy mission, the *Uhuru* satellite, indicated that galaxy clusters have extended X-ray halos arising as thermal bremsstrahlung from hot gas of about 10^7 K in the clusters (e.g., Cavaliere, Gursky, & Tucker 1971; Gursky et al. 1971), revealing the final component of the cluster mass.

Today, galaxy clusters are often termed the "laboratories" of astrophysics. As discussed at the beginning, these objects are agglomerations of galaxies, but the galaxies themselves make up only a minority of the total mass of the cluster. Most of the mass is in the form of dark matter, but even up to about 90% of the luminous, baryonic matter is in the form of this hot, intracluster gas that continues to be studied with modern X-ray missions like *Chandra* and *Suzaku*. The baryonic and dark components of galaxy

clusters coexist in the same proportions within clusters as in the universe as a whole, making each galaxy cluster effectively a "mini-universe" that provides an invaluable glance into the processes that have shaped the universe on a manageable scale.

The three components of galaxy clusters — dark matter, gas, and galaxies — are probed in various ways. In the next few sections, we discuss how these components permit various methods of detecting clusters and, in turn, empower clusters as probes of cosmology. Lastly, we will turn to the next frontier in galaxy cluster astrophysics, the outskirts of galaxy clusters, which have demanded increasing attention in recent years due to the enhanced ability of simulations to capture features at such low densities as well as the availability of data from wide-field imagers and spectrographs that permit efficient observations of these regions.

1.1.1 Detection of Galaxy Clusters

The earliest major catalog of galaxy clusters was the Abell catalog, compiled by astronomer George Abell from the Palomar Observatory Sky Survey, a large extragalactic survey conducted using the 48 inch Schmidt telescope on Mount Palomar, California (Abell 1958). These 1,682 Abell clusters (out of an initial sample of 2,712) were selected and classified as such on the basis of their richness and compactness; in particular, he stipulated that a cluster must have at least 50 member galaxies no more than two magnitudes fainter than the third brightest galaxy and that these member galaxies need to be within a radius of 1.5 h^{-1}Mpc of the cluster's center. Follow-up studies of these and other clusters found that cluster members tend to be early type galaxies, with redder colors and old stellar populations, with the population of blue, star-forming galaxies

increasing towards the outskirts of the cluster (e.g., Dressler 1980).

Optical and infrared survey data continue to provide a valuable means of detecting galaxy clusters. The fact that cluster members are primarily red ellipticals led to the development of a new method of cluster detection, the red sequence method (e.g., Gladders & Yee 2000), that can be automated to quickly process survey data looking for clusters. The $z = 0$ spectrum of an elliptical galaxy features a prominent break at 4000 angstroms arising from the dearth of young blue stars in the galaxy. As the galaxy is redshifted, the location of the break moves to increasingly red wavelengths. If one chooses filters that straddle the 4000 angstrom break at a given cluster cluster redshift and then constructs a graph of galaxy color, where "color" is defined as the difference in magnitudes measured in each filter, against magnitude, the cluster members occupy a linear feature in this color-magnitude space whose color-intercept depends on the redshift of the cluster (examples of such diagrams are furnished in Chapter 3); identification of this feature then provides a sample of prospective cluster members, and the cluster can be detected as an overdensity of these red sequence galaxies on the sky.

Methods based on the red sequence have yielded large catalogs of galaxy clusters down to fairly low masses and richnesses; for instance, Hao et al. (2010) used this method combined with the brightest cluster galaxy (BCG) feature in galaxy clusters to present a catalog of over 55,000 rich galaxy clusters from SDSS DR7. Given the wealth of deep, multiband optical and infrared data that is becoming available from current and upcoming extragalactic surveys such as the Dark Energy Survey (DES) and the Large Synoptic Survey Telescope (LSST), substantial effort is being expended into optimizing and extending the red sequence algorithm to efficiently cover the extent of such large surveys and to make use of the multiband photometry, resulting in the recent redMaPPer

algorithm (Rykoff et al. 2014).

Other catalogs of galaxy clusters have been produced by detecting signatures of the gas content of galaxy clusters. Galaxy clusters have been detected using their X-ray emission in large X-ray surveys, such as in the ROSAT All-Sky Survey (Voges et al. 1999; Piffaretti et al. 2011) and, serendipitously, in the XMM Cluster Survey (Mehrtens et al. 2012), which have yielded catalogs of these objects. Due to cosmological surface brightness dimming, the detection of clusters using X-ray emission depends on redshift, so that the minimum mass required for detection increases at higher redshifts; this is accordingly an inefficient method for detecting high-redshift clusters. However, the galaxy cluster gas can also be probed at millimeter wavelengths as it leaves a signature known as the Sunyaev-Zel'dovich effect (SZE) in the CMB (Sunyaev & Zel'dovich 1972). The thermal SZE arises from inverse Compton scattering of CMB photons off of electrons in the gaseous intracluster medium of galaxy clusters and appears as a temperature decrement at frequencies less than about 218 GHz and an increment at higher frequencies; this signal, unlike the X-ray surface brightness, is redshift-independent. This has allowed the major SZE surveys, the Atacama Cosmology Telescope (ACT) and the South Pole Telescope (SPT), to produce large catalogs of massive galaxy clusters out to redshifts $z \gtrsim 1$ with a nearly uniform selection function (Hasselfield et al. 2013; Bleem et al. 2015).

These preceding methods of cluster detection have focused on the baryonic components of galaxy clusters. However, wide-field imaging surveys can also indirectly probe the dark matter halos of galaxy clusters. The technique of weak gravitational lensing is sensitive to the total mass distributions of galaxy clusters, which act as lenses that distort the shapes of background galaxies. In the weak lensing regime, these distortions are too small to be distinguished from intrinsic variations in shape and

orientation for any individual background galaxy but can be measured statistically for an ensemble of background galaxies. In practice, this has primarily been used to measure masses for individual clusters that were already discovered via another method, but more recently, the weak lensing signal has been considered as a promising means of detecting clusters by mapping the background distortions. Several surveys, including the Deep Lens Survey (Wittman et al. 2006) and the Subaru Weak Lensing Survey (Miyazaki et al. 2007), have successfully employed this method to detect galaxy clusters in small patches of sky.

These methods, taken together, have provided catalogs of thousands of objects. Most of these approaches, in addition to yielding the location of the cluster, can also be used to estimate the cluster mass. As we will see in the next section, both of these quantities are essential for using clusters of galaxies as cosmological probes.

1.1.2 Galaxy Cluster Cosmology

The standard model of structure formation in the universe holds that galaxy clusters arise from the gravitational collapse of matter surrounding the largest peaks in the primordial density field; accordingly, the distribution and abundance of clusters is sensitive to the properties of this field, which are determined by the underlying cosmology (e.g., Press & Schechter 1974; Kaiser 1984; Bardeen et al. 1986). Accordingly, construction of the cluster mass function, $N(M, z)$, which describes the number of clusters above a given mass M in a given redshift bin centered on z provides a powerful cosmological probe. The dominant source of systematic uncertainty comes from the determination of the cluster mass, which can be done in a number of ways, each with its

own challenges and assumptions.

For instance, spectroscopy of cluster members can be used to measure velocity dispersions, which yield the mass of the cluster via the virial theorem. However, this assumes that the cluster galaxy orbits are in equilibrium, an assumption that can be violated in highly disturbed clusters and in cluster outskirts (e.g., Rines et al. 2013). The X-ray emission from galaxy clusters can be used to construct the gas density profile and the radial temperature profile of the cluster; these two quantities yield the total mass of the cluster under the assumption of hydrostatic equilibrium, which has been done for several large samples of clusters (e.g., Vikhlinin et al. 2006, 2009a; Martino et al. 2014). Weak gravitational lensing probes the total mass distribution in galaxy clusters but is susceptible to several sources of uncertainty, among them issues of halo triaxiality, the intrinsic alignments of background galaxies, and uncorrelated structure along the line of sight (Becker & Kravtsov 2011). On the other hand, weak lensing is free of many of the assumptions required to use the baryonic methods of mass estimation (i.e. X-rays), so weak lensing masses are often compared to other masses in order to quantify the biases inherent in these other methods (e.g., Hoekstra et al. 2012; Mahdavi et al. 2013; Gruen et al. 2014).

However, an even more fundamental issue than the method of mass determination is the *definition* of the mass. Galaxy clusters are extended structures that do not have a clearly defined edge or end to their mass distributions. Accordingly, the sizes of clusters are defined in terms of overdensities with respect to a given background density;R_Δ, where Δ is a constant, is the radius within which the mean mass density enclosed is equal to Δ times the background density ρ_b at the cluster redshift, or $\bar{\rho}(R < R_\Delta) = \Delta\rho_b(z)$. The values typically employed in galaxy cluster studies are $\Delta = 200, 500$. The background

density is taken to be either the critical density $\rho_c(z) \equiv 3H(z)^2/8\pi G$, where $H(z)$ is the Hubble parameter at redshift z, or the mean matter density $\rho_m(z) = \rho_c(z)\Omega_m(z)$, the latter of which is usually only used with $\Delta = 200$. The radius often includes a subscript c or m (i.e., R_{200c}, R_{200m}) to clarify which background density is being used. The mass of the cluster can then be parametrized as M_Δ, the mass enclosed within a sphere of radius R_Δ. Typical sizes and masses of clusters are about $R_{200c} \sim 1 - 2\ h^{-1}$Mpc and $M_{200c} \sim 10^{14} - 10^{15}\ h^{-1}M_\odot$, where $M_\odot$ is the mass of the sun.

The virial radius is a similar quantity often used in galaxy cluster cosmology and astrophysics. This term is meant to denote the radius within which matter in the cluster is virialized, or stable and gravitationally bound, and outside of which matter is infalling, but in practice it is often used interchangeably with R_{200c}, implying that $\Delta_{\mathrm{vir},c} \approx 200$. However, there exist approximate analytical formulas for the true virial density contrast $\Delta_{\mathrm{vir},c}$ that depend on cosmological parameters (e.g., Bryan & Norman 1998); these prefer a value of $\Delta_{\mathrm{vir},c} \approx 100$ for the most recent cosmological parameters (Ade et al. 2015). In general, $R_{200c} < R_{\mathrm{vir},c} < R_{200m}$, and all three measures are in widespread use in reference to the galaxy cluster outskirts.

1.1.3 The Outskirts of Galaxy Clusters

The outskirts of galaxy clusters contain a wealth of information about astrophysical processes. Among the diverse and compelling set of investigations that can be conducted in the outskirts are tests of cosmological theories of structure formation (e.g., Fillmore & Goldreich 1984; Bertschinger 1985; Diemer & Kravtsov 2014; Lau et al. 2015), examinations of the evolution of galaxies as they enter the dense environments of clusters

(e.g., Haines et al. 2013; Just et al. 2015), and probes of the environmental dependence of how luminous matter traces the mass distribution of the universe (e.g., Bahcall & Kulier 2014). However, the low matter densities in the outskirts as well as the large areas that they cover on the sky make these regions extremely challenging to probe observationally (for a recent summary of the prospects and challenges, see Reiprich et al. 2013). Recent advances, both in observations and simulations, have reinvigorated the study of these regions.

Simple analytical models of structure formation have long predicted that the outskirts of galaxy clusters should feature steep density jumps in the gas and dark matter profiles (e.g., Fillmore & Goldreich 1984; Bertschinger 1985). The density jump in the gas profile is a strong shock that arises from the accretion of gas onto the cluster. This shock is referred to as the 'virial shock' as it is expected to be located around the virial radius, but it has yet to be detected in galaxy clusters. Past R_{500}, the X-ray surface brightness falls off quickly, making it difficult to detect features in the outskirts using standard observation strategies. Kocsis, Haiman, & Frei (2005) predicted the signature of the virial shock in observations of the thermal SZE, but thus far those measurements have not been able to constrain this feature either. However, the most recent hydrodynamical simulations have reaffirmed the predictions of accretion shocks at around $\sim 1.3R_{200c}$ (at $z = 0$) with Mach numbers of about $\mathcal{M} \sim 2.7$ (Schaal & Springel 2015).

Recent dark matter simulations have strengthened the arguments in favor of a density jump in the outer dark matter profiles as well. The analysis of Diemer & Kravtsov (2014) identified a density jump corresponding to the accumulation of recently-accreted particles at the apocenter of their first orbit. The location of the jump depends on the

mass accretion rate but generally occurs near the virial radius. These density jump features, if detected in observations, would provide confirmation of our understanding of cosmological structure formation. Furthermore, detecting the dark matter jump would provide a new test of the collisionless nature of dark matter, and its location could serve as a physically-motivated definition of cluster boundaries in place of R_Δ (e.g., More, Diemer, & Kravtsov 2015). These implications make the infall regions at the outskirts of clusters, where large-scale filaments connect to the clusters, a compelling focus for both observational campaigns and further theoretical investigations, which this thesis will provide in Chapters 2 and 3.

1.2 The Clustering of Galaxies on Large Scales

Moving beyond galaxy clusters, on large scales the distribution of galaxies in the universe provides an important cosmological probe under the assumption that the galaxies trace the underlying mass distribution. More specifically, galaxy redshift surveys assume that the population of galaxies that they target are tracers of the large-scale mass distribution; for instance, the SDSS-III Baryon Oscillation Spectroscopic Survey (BOSS; Dawson et al. 2013), targets luminous red galaxies (LRGs), while the upcoming Dark Energy Spectroscopic Instrument (DESI; Levi et al. 2013) will target LRGs and emission line galaxies (ELGs). A key source of systematic uncertainty in such surveys is understanding the extent to which each target population traces large-scale structure.

We can expect that galaxies demonstrate a variety of clustering behaviors. For instance, as has already been discussed, red galaxies — which form the bulk of galaxy cluster members — tend to be more clustered than blue galaxies, which are more

typically found in the field. Several studies have split samples of galaxies according to color or luminosity (e.g., Swanson et al. 2008; Ross et al. 2014) and studied their relative clustering to place constraints on this systematic and analyze its effects on one of the primary cosmological probes from redshift surveys, the baryon acoustic oscillations (BAO).

BAO refer to sound waves in the early universe that were able to travel a certain distance before recombination, leaving an overdense shell at a characteristic acoustic scale of about $R = 100\ h^{-1}$Mpc. This scale results in a preferred location for galaxies to cluster today and serves as a "standard ruler" (for a review of this method and its principles, see Weinberg et al. 2013). The first detection of the BAO occurred in 2005 (Cole et al. 2005; Eisenstein et al. 2005) using data from the 2dFGRS and SDSS. At present, the BAO method is one of the most competitive cosmological probes and has allowed percent level measurements of the distance scale at $z = 0.57$ (Anderson et al. 2014). However, the detection of this feature requires a sufficient density of spectroscopically observed galaxies, which can represent a significant investment of observing time. More formally, as described in Weinberg et al. (2013), the error on each Fourier mode in a survey is given by $\sigma_P/P = (nP + 1)/nP$, where P is the power spectrum and n is the density of spectroscopic galaxies; for $n < 1/P$, the error becomes large, decreasing the information imparted by the mode.

In subsequent chapters, we will consider these issues in more detail. In particular, in Chapter 4, we will present a detailed study of the key systematic in galaxy redshift surveys — the extent to which certain types of galaxies trace large-scale structure — by examining the stochasticity between red and blue samples of galaxies. In Chapter 5, we address the other difficulty in using the BAO method, the need for sufficiently dense

spectroscopy, by presenting a new method of measuring the BAO in sparse spectroscopic data sets via cross-correlations with dense photometry.

1.3 High Redshift Galaxies & Dwarf Galaxies

Lastly, we consider galaxies at two extremes — the most distant galaxies ever discovered and the closest neighbors of the Milky Way, the Local Group dwarf galaxies. The current major optical and infrared space observatories, the *Hubble Space Telescope* and the *Spitzer Space Telescope*, have pushed the boundaries of observations of galaxies to the first hundreds of Megayears after the Big Bang, a period known as the epoch of reionization ($z \gtrsim 6$). These observations have not found enough galaxies to reionize the universe, suggesting that there must be a fainter population of high-redshift galaxies that these current missions are not able to probe (e.g., Alvarez et al. 2012; Finkelstein et al. 2012; Bouwens et al. 2015; Robertson et al. 2015). The upcoming 6.5 meter *James Webb Space Telescope* (*JWST*) will be able to detect galaxies to fainter limits.

On the other hand, the dwarf galaxies of the Local Group are believed to be similar to the most abundant galaxies at the epoch of reionization, as their old stellar populations and low masses suggest that they formed their stars at early times, making them relics of the early universe (e.g, Bullock et al. 2000; Ricotti & Gnedin 2005; Loeb & Furlanetto 2013). The proximity of these dwarf galaxies empowers detailed studies of their star formation histories. These investigations have found mixed results, with some dwarfs showing significant late-time star formation (Brown et al. 2014; Weisz et al. 2014; Weisz, Johnson, & Conroy 2014); nevertheless, some of the galaxies may be true relics, and their progenitors await discovery at higher redshifts. In Chapter 6, we address this

issue, aiming to determine whether *JWST* will, in fact, be able to reveal the progenitors of these populous galaxies.

We will address a number of the questions raised here in the subsequent chapters. Beginning on small scales, we will explore density jumps in the outskirts of galaxy clusters in Chapters 2 and 3, before transitioning to larger scales in Chapters 4 and 5. On these large scales, we will investigate a key systematic in galaxy redshift surveys as well as develop a new method to measure the cosmic distance scale with sparse datasets. Finally, in Chapter 6, we will move to the extremes of the universe to discuss the prospects for detecting analogues of the most familiar local galaxies at high redshifts.

Chapter 2

A Simple Physical Model for the Gas Distribution in Galaxy Clusters

Anna Patej & Abraham Loeb, 2015, *The Astrophysical Journal Letters*, 798, L20

2.1 Introduction

Gas hotter than 10^7 K permeates the intergalactic media of galaxy clusters and constitutes the dominant baryonic component of these virialized objects. Understanding the properties and distribution of this intracluster gas yields insights into cosmology and the physics of galaxy clusters. For example, knowledge of the density and temperature profiles of the gas from X-ray data, coupled with the assumption of hydrostatic equilibrium, provides an estimate of the total mass of the cluster, which can be used statistically to constrain cosmological parameters (Vikhlinin et al. 2009b; Ettori et al. 2013). High-resolution hydrodynamical simulations incorporate the physical phenomena

– supernova, AGN feedback, as well as radiative cooling – that shape the observed density and temperature profiles of galaxy clusters (see Kravtsov & Borgani 2012; and references therein).

At the intersection of the observational and theoretical fronts lies analytical modeling of the density profiles of X-ray emitting intracluster gas. The gas density has been described by a variety of functions, most notably the β-model (Cavaliere & Fusco-Femiano 1976) and modifications thereof (Vikhlinin et al. 2006). Such functions are either ad hoc models with many parameters to provide fitting flexibility or motivated using unfounded physical assumptions (the popular β-model, for example, is derived assuming the isothermality of the cluster gas). More recent works have attempted to establish physically motivated models via the assumptions of hydrostatic equilibrium and, for instance, a polytropic equation of state (Ostriker, Bode, & Babul 2005; Bulbul et al. 2010) or an analytical temperature profile tailored to data (Ascasibar & Diego 2008). However, these models still typically require more parameters than the simple β-profile to model the range of cluster features observed in X-ray data and impose quite stringent constraints on the physics of the gas. Our goal is to provide a prescription for a new family of profiles that satisfies a set of simple physical assumptions and that has sufficient fitting flexibility to improve upon – but as many or fewer parameters as – the standard β-model.

2.2 Background

2.2.1 Gas Density Profiles

Galaxy cluster gas density profiles have been traditionally described by the three-parameter β-model,

$$\rho_{\rm g}(r) = \frac{\rho_0}{(1 + (r/r_c)^2)^{3\beta/2}}, \tag{2.1}$$

with a standard value of $\beta = 2/3$. The β-model is physically motivated; that is, it may be derived from the equation of hydrostatic equilibrium assuming that the gas is isothermal and that the total matter distribution is described by a King model (Cavaliere & Fusco-Femiano 1976). However, the cluster gas is not isothermal (Vikhlinin et al. 2005; Pratt et al. 2007; Leccardi & Molendi 2008). Furthermore, the β-model is limited in its ability to describe the observed features of galaxy cluster gas density distributions. Many clusters, particularly the relaxed clusters most often targeted for X-ray measurements, feature cuspy profiles, while the β-model produces a central core, which is more typical of merging systems (Vikhlinin et al. 2006). Accordingly, analyses relying on the β-model often exclude data in the centers out to large radii in order to obtain good fits (e.g., Pointecouteau et al. 2004).

To circumvent this issue, many papers have built upon the β-model by adding more parameters to increase modeling flexibility. One such model is the double β-model (e.g., Mohr, Mathiesen, & Evrard 1999), which simply adds an additional β-profile with a different core radius and β parameter to separately fit the inner and outer regions. Another, more recent model is that of Vikhlinin et al. (2006), who modified a β-model

base by adding functional features to match observations, yielding a ten-parameter model:

$$\rho_{\rm g}^2(r) = \frac{\rho_{0,1}^2}{(1+(r/r_s)^\gamma)^{\epsilon/\gamma}} \frac{(r/r_{c,1})^{-\alpha}}{(1+(r/r_{c,1})^2)^{3\beta_1-\alpha/2}} + \frac{\rho_{0,2}^2}{(1+(r/r_{c,2})^2)^{3\beta_2}}. \tag{2.2}$$

However, although such models greatly improve the fit to data, their forms are no longer motivated by physical principles but are rather constructed from knowledge of variations in cluster gas profiles. Our approach is different; rather than starting with a knowledge of gas profiles, we begin with a few physical and cosmological requirements, in particular that the virialized baryon content of the cluster is representative of the universe and that the cluster features a virial shock.

2.2.2 The Virial Shock

Cosmological theories of structure formation predict that matter accreting onto galaxy clusters should experience a shock, termed the 'virial shock,' coinciding roughly with the virial radius of the cluster (e.g., Bertschinger 1985). Detection of such a shock around a cluster would serve as an important probe of cosmological infall and accretion. Previous work has examined the impact of shocks on relations between X-ray observables such as the luminosity-temperature relation (Cavaliere, Menci, & Tozzi 1997), but we will instead relate the physics of the shock and the dark matter content of the cluster in deriving families of gas density profiles.

To do so, we will rely on the Rankine-Hugoniot shock jump conditions, which, for the gas density, state that (Landau & Lifshitz 1987):

$$\Gamma_{\rm g} \equiv \frac{\rho_2}{\rho_1} = \frac{(\gamma+1)\mathcal{M}^2}{(\gamma-1)\mathcal{M}^2+2}, \tag{2.3}$$

where γ is the gas adiabatic index, $\mathcal{M}$ denotes the shock Mach number, and ρ_2 and ρ_1 are the densities of the cluster gas and the infalling gas, respectively, at the shock. For a monatomic gas with $\gamma = 5/3$, the maximum value of the jump is $\Gamma_{\rm g} = 4$ as $\mathcal{M} \to \infty$.

Diemer & Kravtsov (2014) have recently found that dark matter profiles in fact exhibit a similar jump near the virial radius of the cluster (see also Adhikari, Dalal, & Chamberlain 2014) . In analogy to the gas shock jump parameter $\Gamma_{\rm g}$, we will parameterize the jump in the dark matter density by $\Gamma_{\rm DM}$.

2.3 Method

We seek to obtain gas density profiles not from an ad hoc prescription tailored to suit a data set, but rather from making only a few simple assumptions about the structure and physics of the galaxy cluster, including the virial density jumps discussed above. As shall be explored further in §2.4, the result is a family of profiles with up to as many parameters as the β-model, but better able to accommodate the diversity of features observed in cluster gas profiles.

2.3.1 Assumptions

Our model galaxy cluster is spherically symmetric, with a virial shock occurring at a radius s and a known dark matter profile $\rho_{\rm DM}(r)$. We define $f_g = \eta\Omega_b/\Omega_{DM}$, where η is a parameter fixing the fraction of baryons in the gas phase within s, and Ω_b and Ω_{DM} are the cosmological density parameters of baryons and dark matter, respectively. We then assume the following three conditions:

I. $M_{\rm g}(< s) = f_g M_{\rm DM}(< s)$

II. $\rho_{\rm g}(s^-) = \Gamma_{\rm g}\rho_{\rm g}(s^+)$

III. $\rho_{\rm g}(r) = f_g\rho_{\rm DM}(r)$ for $r > s$, and for all r if $\Gamma_{\rm g} = 1$

where the minus and plus indicate the regions just to the inside and outside of the shock, respectively, and we assume that a dark matter jump is coincident with the gas shock, so that $\Gamma_{\rm DM} = \rho_{\rm DM}(s^-)/\rho_{\rm DM}(s^+)$; hereafter, for simplicity, we will refer to the dark matter profile with this jump by the name of the unperturbed dark matter model, so we note that, for a given dark matter model $\rho_{\rm m}(r)$ internal to s, the profile external to s is in fact $\rho_{\rm DM}(r) = \rho_{\rm m}(r)/\Gamma_{\rm DM}$.

Lastly, to allow us to solve for a profile, we introduce one additional assumption: denoting $x = r/r_s$, where r_s is a scale radius in a given model, and referring to condition I, we employ the following ansatz:

$$\frac{1}{f_g}M_{\rm g}(x) = M_{\rm DM}(\xi x^n), \tag{2.4}$$

where ξ and n are parameters to be found. This choice of parametrization has the benefits of being mathematically simple and preserving scale invariance. We now apply these conditions to find profiles for the gas internal to the virial shock.

2.3.2 General Derivation

Beginning with the relation defined by equation (2.4), we obtain the gas density profile as:

$$\rho_{\rm g}(x) = \frac{1}{4\pi x^2}\frac{dM_{\rm g}}{dx} = \frac{f_g}{4\pi x^2}\frac{d}{dx}M_{\rm DM}(\xi x^n), \tag{2.5}$$

$$\rho_{\rm g}(x) = f_g n \xi^3 x^{3n-3}\rho_{\rm DM}(\xi x^n). \tag{2.6}$$

Now, using conditions II and III, we see that:

$$\rho_{\rm g}\left(\frac{s}{r_s}\right) = f_g n \xi^3 \left[\frac{s}{r_s}\right]^{3n-3} \rho_{\rm DM}\left(\xi\left[\frac{s}{r_s}\right]^n\right); \tag{2.7}$$

the argument of the dark matter function then yields:

$$\xi\left[\frac{s}{r_s}\right]^n = \frac{s}{r_s} \Rightarrow \xi = \left[\frac{s}{r_s}\right]^{1-n}, \tag{2.8}$$

and the normalization gives:

$$n\xi^3\left[\frac{s}{r_s}\right]^{3n-3} = \frac{\Gamma_{\rm g}}{\Gamma_{\rm DM}} \equiv \Gamma. \tag{2.9}$$

Combining these two expressions then provides us with ξ and n in terms of our physical variables:

$$n = \Gamma, \tag{2.10}$$

$$\xi = \left(\frac{s}{r_s}\right)^{1-\Gamma}. \tag{2.11}$$

This means that our final expression for the gas density is simply:

$$\rho_{\rm g}\left(\frac{r}{r_s}\right) = \Gamma f_g \left(\frac{r}{s}\right)^{3\Gamma-3} \rho_{\rm DM}\left(\frac{s}{r_s}\left[\frac{r}{s}\right]^\Gamma\right). \tag{2.12}$$

2.3.3 Power Law Profile

To motivate our method, we first obtain a family of gas density profiles assuming a simple power law for the dark matter density profile,

$$\rho_{\rm DM}(r) = \frac{A}{r^k}, \tag{2.13}$$

with $k < 3$. This profile describes, for instance, the singular isothermal sphere with $k = 2$. For this profile, $r_s = 1$, and equation (2.12) yields:

$$\rho_{\rm g}(r) = \frac{\Gamma f_g A}{s^k (r/s)^{3+\Gamma(k-3)}}. \tag{2.14}$$

It is straightforward to verify that such a profile fulfills the conditions of §2.3.1.

2.3.4 Einasto Profile

We next consider the Einasto profile (Einasto 1965),

$$\rho_{\rm DM}(r) = A \exp\left[-\frac{2}{\alpha}\left(\frac{r}{r_s}\right)^{\alpha}\right], \tag{2.15}$$

which recent cosmological simulations have found to be a very good description of dark matter halos (e.g., Ludlow et al. 2013), but which has not yet enjoyed as widespread use as some other models, partly due to the lack of closed-form expressions for many quantities of interest, such as the surface density (Retana-Montenegro, et al. 2012). However, the gas density derived from this profile using our method does have an analytical form:

$$\rho_{\rm g}(r) = \Gamma f_g A \left(\frac{r}{s}\right)^{3\Gamma-3} \exp\left[-\frac{2}{\alpha}\left(\frac{s}{r_s}\right)^{\alpha}\left(\frac{r}{s}\right)^{\Gamma\alpha}\right]. \tag{2.16}$$

2.3.5 NFW Profile

We now apply our method to the widely-used Navarro-Frenk-White (NFW) (Navarro, Frenk, & White 1997) profile,

$$\rho_{\rm DM}(r) = \frac{A}{r/r_s(1+r/r_s)^2}, \tag{2.17}$$

which has been demonstrated to provide a good fit to dark matter halos in simulations. Using equation (2.12), we find:

$$\rho_{\rm g}(r) = \Gamma f_g A \frac{(r/s)^{2\Gamma-2}}{r/r_s\left(1+(s/r_s)\,(r/s)^{\Gamma}\right)^2}. \tag{2.18}$$

Our profile has two parameters fixed by the choice of an NFW dark matter profile, the amplitude $A = \rho_c\delta_c$ and the scale radius r_s. These can be obtained independently of the gas data (for instance, via weak lensing). The other three are free parameters: the gas fraction f_g, the shock radius s, and the jump ratio Γ. Qualitatively, our analytic expression for the gas density yields a cuspy inner profile for $1 < \Gamma < 1.5$, a pure core for $\Gamma = 1.5$, a core with an inner decline for $1.5 < \Gamma \lesssim 2$, and a central depression for $\Gamma \gtrsim 2$. Examples of these profile types are illustrated in Figure 1.

2.3.6 Generalized NFW Profiles

The NFW profile of the preceding section can be characterized by its behavior at two extremes – in the large r limit, $\rho_{\rm NFW} \sim r^{-3}$, while for small r, $\rho_{\rm NFW} \sim r^{-1}$. However, dark matter halos do exhibit some scatter, particularly in their internal structure. As a result, it is possible to consider the NFW profile as a special case of a broader family of

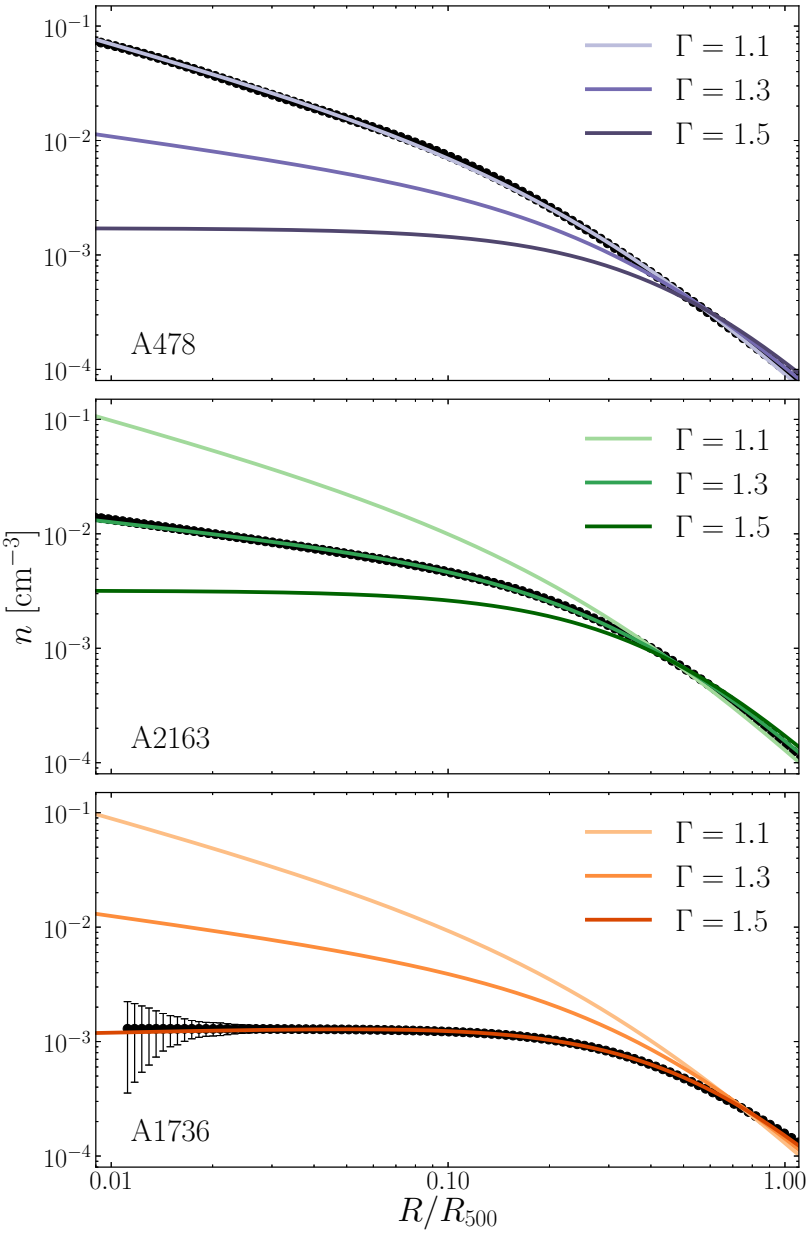

Figure 1.—: Gas profiles for various choices of Γ, assuming an NFW dark matter profile as described in §2.3.5, plotted against the deprojected gas density profiles of three clusters with various morphologies.

models, the generalized NFW profiles:

$$\rho(r) = \frac{A}{(r/r_s)^{\alpha}\,(1 + r/r_s)^{3-\alpha}}, \tag{2.19}$$

which ensure that for large r, $\rho \sim r^{-3}$, while allowing for variations in the central region, for which $\rho \sim r^{-\alpha}$.

Both cosmological simulations and observational data have yielded diverse estimates for the value of the α parameter. As discussed above, the work of Navarro, Frenk, & White (1997) yielded $\alpha = 1$, in good agreement with simulations and data. On the other hand, the simulations of Moore et al. (1999) suggested that $\alpha = 1.5$, which is an upper bound of the range of the recent results of Schaller et al. (2014), whose simulations found dark matter slopes that tend to be steeper than that of the NFW model for small clusters, and similar to NFW for large clusters. On the observational side, several efforts have obtained values of $\alpha < 1$ (Newman et al. 2013; and references therein), while other analyses have concluded that $\alpha \approx 0.9 - 1.2$ (Oguri et al. 2009; Richard et al. 2009; Saha & Read 2009).

We can test the implications of these variations for our method by deriving a family of profiles for the generalized NFW profile. From equation (2.12), we obtain:

$$\rho_{\rm g}(r) = \Gamma f_g A \frac{(r/s)^{(3-\alpha)\Gamma+\alpha-3}}{(r/r_s)^{\alpha}(1 + (s/r_s)(r/s)^{\Gamma})^{3-\alpha}}. \tag{2.20}$$

We immediately see that this profile reduces to equation (2.18) for $\alpha = 1$.

In principle, we are interested in the regime in which the profiles yield either cuspy or cored interiors, which are the two observed types of gas density profile, as will be explored further in §2.4. From equation (2.20), this condition can be expressed as:

$$(3 - \alpha)\Gamma - 3 \lesssim 0, \tag{2.21}$$

which imposes a constraint on the allowed values of Γ. We thus find that, for $\alpha = 1$, as before, $\Gamma \lesssim 3/2$, while for $\alpha = 3/2$, $\Gamma \lesssim 2$, and for $\alpha = 2$, $\Gamma \lesssim 3$. Accordingly, we see that by modifying the value of α, we can alter the range of acceptable Γ values. However, for the remainder of the paper, we will use the gas profile that we obtained from the standard NFW ($\alpha = 1$) dark matter profile, defined by equation (2.18).

2.4 Comparison with Observations

Having established the mathematical structure of our model (equation (2.18)), we now aim to test it against observational data. We use deprojected gas density profiles from Vikhlinin et al. (2006) (hereafter V06), which consists of 13 low-redshift, relaxed clusters and groups, and the low-redshift sample of Vikhlinin et al. (2009a) (V09), which provides a more representative sample of clusters, including both relaxed and disturbed systems. We defer to the above papers for additional details on the data, but we note that we adopt the same ΛCDM cosmological parameters: $h = 0.72$, $\Omega_\Lambda = 0.7$, and $\Omega_m = 0.3$.

We fit both our model and the β-model to the data, excluding USGC S152 since it has no listed r_{500} – the radius corresponding to a density of 500 times the critical density ρ_c – or c_{500} – the corresponding concentration parameter – value. For the clusters in the 2006 sample, we have all of the quantities – the redshift z, c_{500}, and r_{500} – needed to determine the NFW parameters of our model. For the V09 sample, we lack only individual c_{500} values, and instead assume a fixed value of $c_{500} = 3.5$ for all the clusters, which is reasonable for the mass range of these clusters (see V06 and V09 and references therein).

To transform the mass density to a number density, we use $\rho_g = 1.274 m_p (n_e n_p)^{1/2}$, where the conversion factor assumes a primordial abundance of helium and a $Z = 0.1 Z_\odot$ abundance of heavier elements. We additionally constrain our fits to 20 kpc $< r < r_{500}$; the lower limit is imposed to avoid the contribution of the central galaxy, and the upper limit excludes the data points that are beyond the field-of-view of *Chandra* and are instead extrapolated from the model of V06. The results of our fits to the clusters are summarized in Figure 2 and examples of our fits are shown in Figure 3 for relaxed clusters and Figure 4 for merging systems. We now discuss these in turn.

2.4.1 Fit Parameters

The top left panel of Figure 2 shows the distribution of fitted f_g parameters, which are generally reasonable gas fraction estimates. However, it is worth noting that the f_g parameter measured here is the gas fraction interior to the shock radius s, as per condition I, as well as the local gas fraction normalization of the profile exterior to s, following condition III. Interior to s, the gas fraction is not constant (except in the case where $\Gamma_{\rm g} = 1$ and the interior profile is simply a scaled NFW profile). The radial variation of the ratio of our profile to its progenitor NFW profile is shown in the bottom left panel of Figure 2 for four clusters with various values of Γ.

The distribution of fitted Γ parameters is given in the top right panel of Figure 2, from which it is clear that the data favor values of $\Gamma \lesssim 1.5$. This trend can be partly explained by the composition of our sample, which comprises primarily relaxed clusters with cuspy central profiles. This suggests that $\Gamma_{\rm g}$ and $\Gamma_{\rm DM}$ should be comparable. The recent simulations of Schaal & Springel (2015) favor $\mathcal{M} \approx 2.7$, which for a gas with

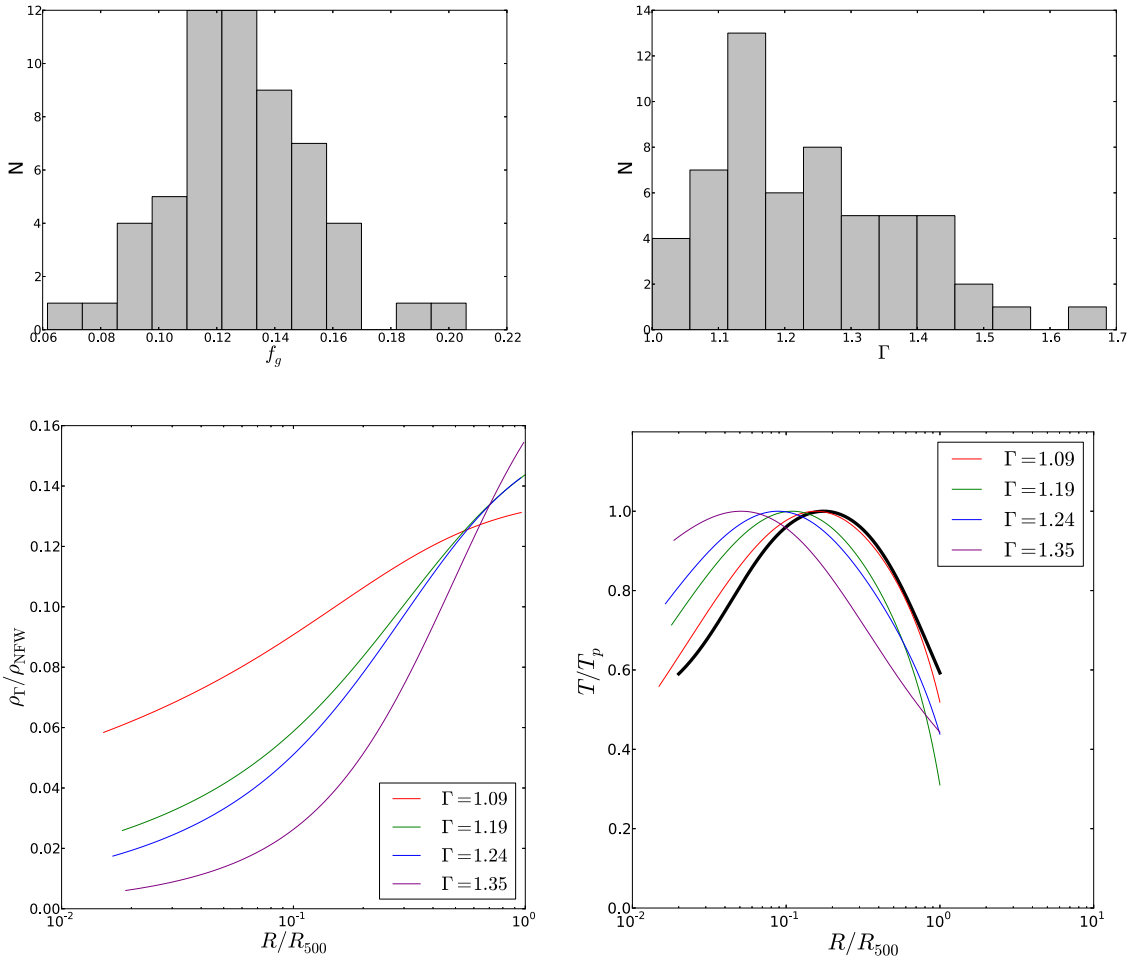

Figure 2.—: A summary of the results of fitting our model to the cluster sample. Top: the distribution of fitted f_g (left) and Γ values (right) for the V06 and V09 samples. The parameter s is poorly constrained and thus not included. Bottom: the radial variation of $\rho_\Gamma/\rho_{\rm NFW}$ (left) and the scaled temperature profiles (right) resulting from a numerical computation using the equation of hydrostatic equilibrium and our density model for four clusters alongside the average temperature profile from V06 in black.

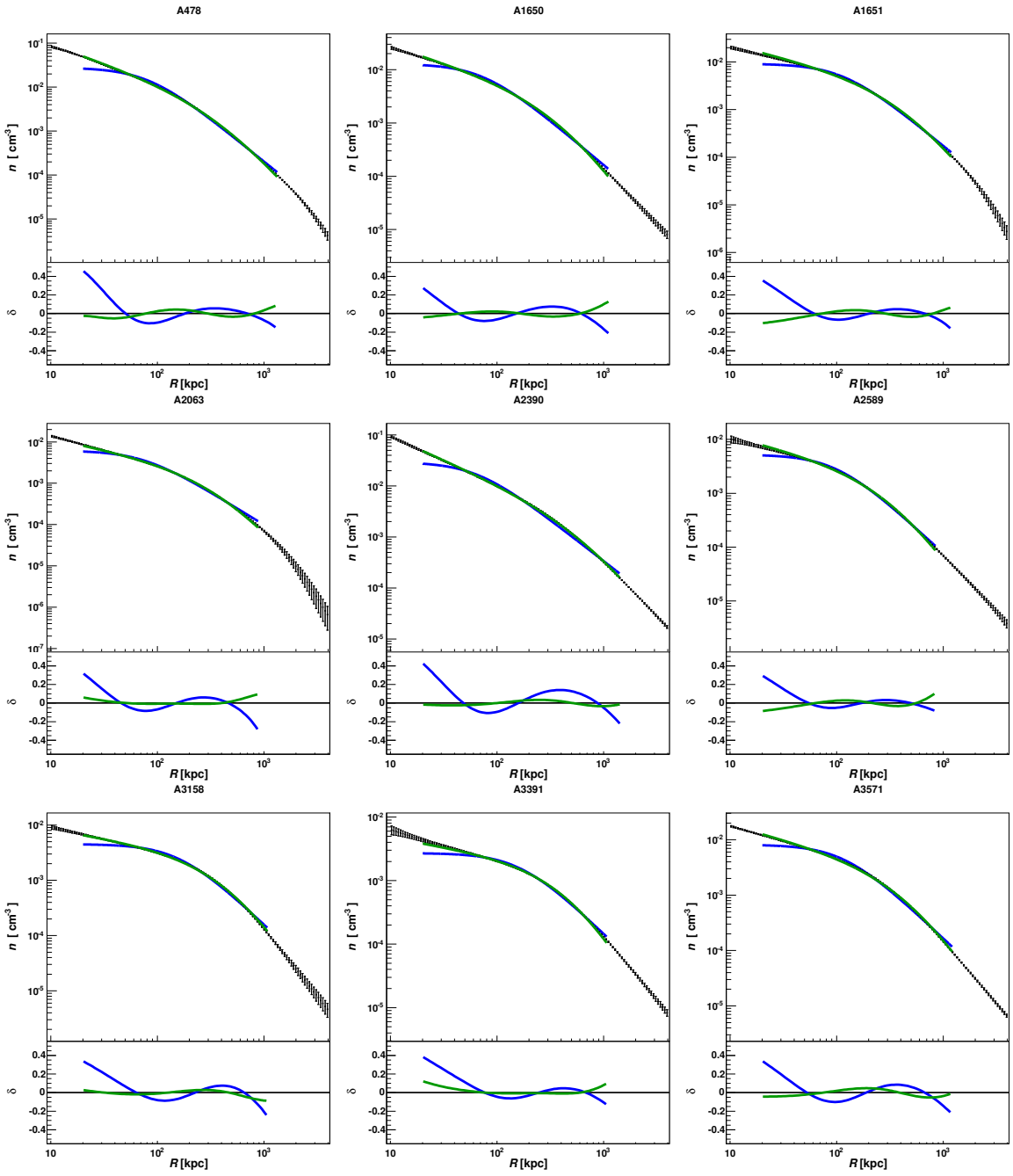

Figure 3.—: Examples of fits to a subsample of gas density profiles of relaxed clusters for which our model (green) provides a reasonable description over the range of radii considered; the β-model (blue) is shown for comparison. The lower panel shows the normalized residual, δ (see text).

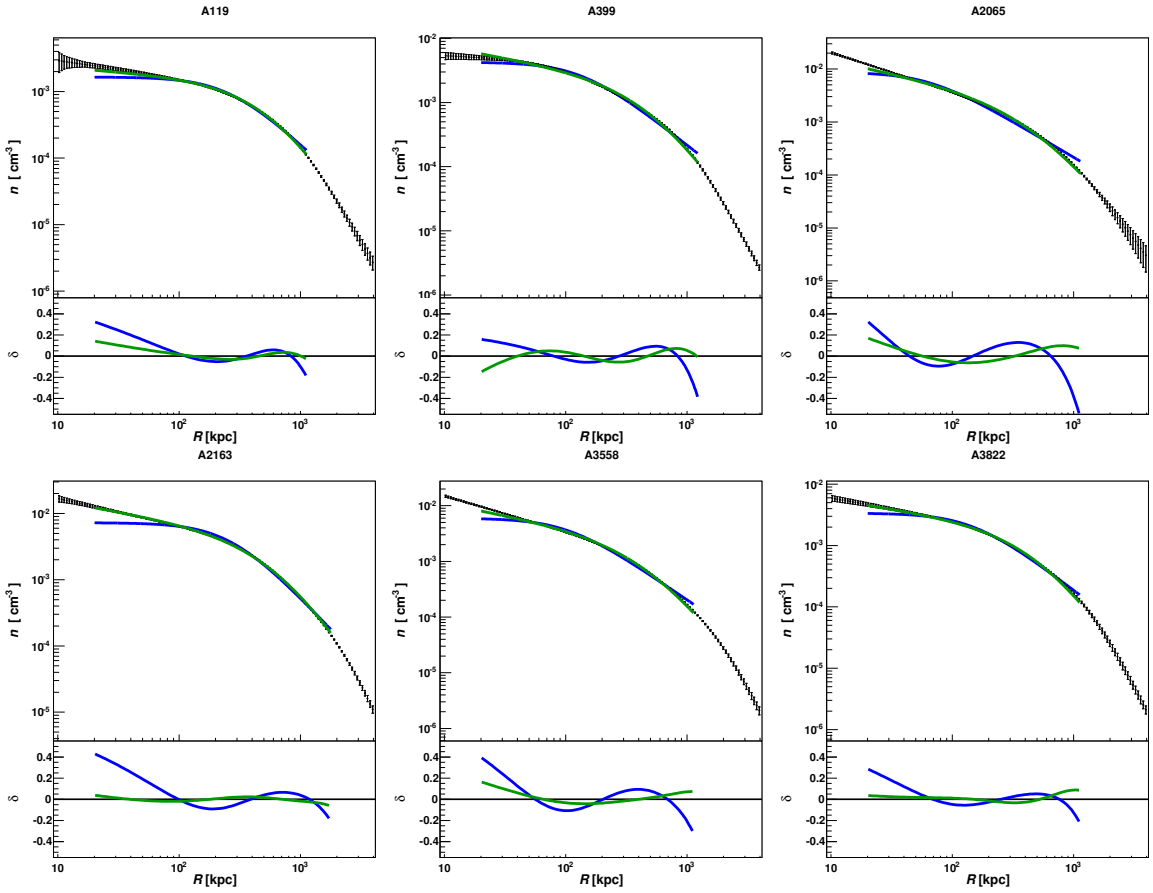

Figure 4.—: Same as Figure 3, but for systems identified as mergers by V09.

$\gamma = 5/3$ implies a shock jump of $\Gamma_g \approx 3$; these simulations coupled with our inferences from X-ray data thus suggest that $\Gamma_{DM} \approx$ 2-3.

An additional consequence of these low Γ values is that the model is not very sensitive to the value of s; indeed, by construction, if $\Gamma = 1$, the s parameter disappears from the model entirely. Accordingly, the s parameter is not well-constrained, and the fitting procedure typically chooses a value at one of the fitting limits. These results thus indicate that our model is really at most a two-parameter model; the use of our model with even fewer parameters is discussed further in §2.4.3.

We present one other result in Figure 2: in the bottom right panel, we show the temperature profiles obtained for four relaxed clusters by numerically solving the equation of hydrostatic equilibrium with sensible initial conditions for each cluster. For comparison, we scale all the temperature profiles by their peak value T_p and also plot the average analytical model of V06; we see good agreement between the analytical model and our numerical profiles for relaxed clusters. Since this suggests that our model is in agreement with the detailed prescriptions of V06, we now turn to comparisons with the traditional β-model.

2.4.2 Model Comparison

Figures 3 (relaxed clusters) and 4 (merging clusters) show a subset of clusters fitted with both our model and the β-model for which our model provides a good description of the behavior of the gas over the fairly wide range of radii we consider. The bottom panel in each of the plots shows the normalized residual $\delta = (\rho_m - \rho_d)/\rho_d$, where m and d refer to the model and data, respectively. These residuals provide a measure for

comparing the fits, as we cannot use the reduced χ^2, for not only are we fitting to data reconstructed via the analytical model of V06, but we are doing so with a model whose parameters are non-linear, rendering the statistic formally untenable.

We make such a comparison in Figure 5, in which we show the distribution of maximum normalized residuals $|\delta|$ for all clusters. The distributions are clearly more favorable for our model. If we compare the values of these maximum residuals, we find, as expected, that our model does better in the central regions where the β-model cannot accommodate a cusp, but we also see significant improvement using our model in the outer regions of the clusters, where the β-model yields several large outliers.

Accordingly, we find that our model provides a good description for many of the clusters in our sample, and improves upon the β-model for most clusters over the range 20 kpc $< r < r_{500}$, although our model does tend to not be a good description of the lowest mass clusters in our sample ($M_{500} \lesssim 3 \times 10^{14} M_{\odot}$). Additionally, as can be seen by way of comparing Figures 3 and 4, our model tends to be a better description for relaxed systems than merging ones. This is not particularly surprising, as our derivation assumes fairly basic properties (such as spherical symmetry and a simple NFW model for the dark matter) that may not hold in the case of mergers. Furthermore, compared to the β-model, we make substantial improvements to fitting the central regions of the relaxed clusters, primarily due to one parameter, Γ.

2.4.3 Extensions of the Model

The results of the preceding sections have indicated that our model is in fact most strongly dependent on the parameter Γ, which controls the shape of the profile.

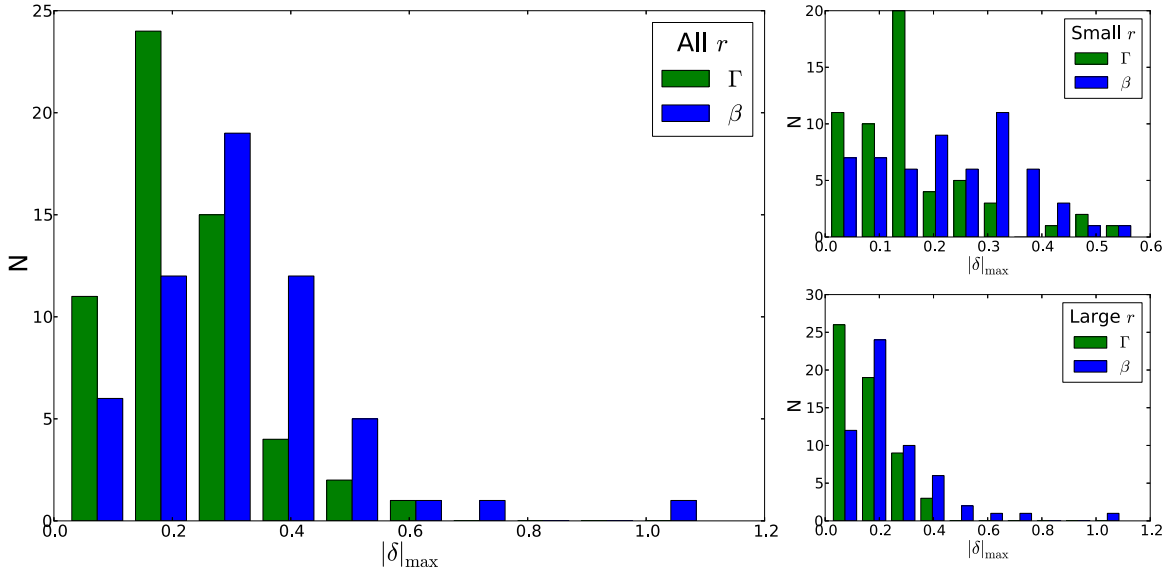

Figure 5.—: Histograms of the maximum normalized residual $|\delta|$ from fitting our model (green) and the β-model (blue) to all clusters. The lefthand panel considers the values of $|\delta|$ over the entire radial range of each cluster (20 kpc $< r < r_{500}$), while the righthand panels show the distributions using truncated ranges: the central region (top), 20 kpc $< r <$ 400 kpc, and the outer region (bottom), 400 kpc $< r < r_{500}$.

Accordingly, it is possible to use this model as a one-parameter family of profiles by fixing s to some reasonable value (for instance, for these low-redshift clusters, $s \approx$ 2-3 Mpc is acceptable since $s \sim r_{vir} \sim 2r_{500}$) and also fixing $f_g = \Omega_m/\Omega_{DM}(\Omega_b/\Omega_m - f_*)$, where f_* is the fraction of baryonic matter in stars and for which values can be estimated independently based on optical/infrared data.

Our model, having been derived from the NFW profile, is of course dependent upon the NFW parameters r_s and δ_c, for which r_Δ and corresponding c_Δ (where Δ indicates the overdensity with respect to the critical density) should be determined. These can be obtained through other means, such as weak lensing. However, one can also leave these parameters free in the fit and obtain a model with the three free parameters (Γ, r_s, δ_c) instead of (Γ, f_g, s). In any case, the model has significant freedom and yet enough simplicity to provide an attractive alternative to the β-model.

2.5 Discussion

By imposing only three simple cosmological and physical conditions that a gas density profile must satisfy, we have derived a family of profiles, characterized primarily by a single parameter Γ, that provide a good description of observational data over a wide range of radii. Our model can be used with 1-3 free parameters, each of which possesses a physical interpretation – Γ and s come from the condition that there exist a virial shock on the outskirts of the cluster and represent its strength (relative to the dark matter jump) and location, respectively, while f_g is a gas fraction parameter that fixes how much of the baryonic matter of the cluster is in the gas phase within s. However, upon comparison with X-ray data, we find that observations favor low values

of Γ, the main parameter controlling the shape of the profile, which in turn leads to the s parameter being poorly constrained. Additionally, average values of f_g can be estimated from the literature, and fixing both it and s to reasonable values leaves us with a one-parameter model.

The derivation of our model assumes that the dark matter distribution internal to s follows an NFW profile; accordingly, we have additional NFW parameters in our model. We do not necessarily count these as free parameters, since for many clusters they can be obtained from other data sets. However, in lieu of additional information, one can also consider an alternative model with the three parameters (Γ, r_s, δ_c) and s and f_g fixed, as discussed above.

Upon comparison with data, we find that our model provides enhanced flexibility over the β-model in the central regions of clusters, which can feature either prominent cores or cusps, while not introducing more parameters. Our model thus does not require an arbitrary radius cutoff, which is often necessary for modeling with the β profile. We find satisfactory agreement between our model and the data for both relaxed clusters and mergers, although as a whole our model is a better description for relaxed systems. This is understandable, since mergers can violate some of the assumptions that we make.

Overall, our family of functions provides a simple but accurate model of the galaxy cluster gas density distribution. We anticipate that it will have applications in both observational and theoretical work. From observations, we await confirmation of the virial shock, whose strength and location will provide an evaluation of our model parameters. On the theoretical side, our model can be used as a simple description of a wide range of cluster gas morphologies in numerical simulations. Furthermore, the

prescription we present herein is not limited to the model that we present; in addition to the other families of profiles that we derived in §4.3, there are numerous extensions and modifications of our conditions that can be imposed to generate yet other models. Future efforts may build upon this framework to introduce additional physics of galaxy clusters into the modeling of their gas distributions.

2.6 Acknowledgments

We would like to thank Alexey Vikhlinin for very helpful discussions and providing the data used in §2.4. We also greatly appreciate Bill Forman's thoughtful comments on a draft of this paper, and thank Andrey Kravtsov for bringing to our attention the recent papers on dark matter jumps. A.P. is supported by the National Science Foundation Graduate Research Fellowship under Grant No. DGE-1144152. This work was also supported by NSF Grant No. AST-1312034.

Chapter 3

Density Jumps Near the Virial Radius of Galaxy Clusters

Anna Patej & Abraham Loeb, accepted for publication in *The Astrophysical Journal* (2016)

3.1 Introduction

Galaxy clusters contain a representative sample of the matter in the universe: the dominant constituent is dark matter, while the baryonic components include hot gas and the galaxies themselves (for a review, see Voit 2005). A longstanding analytical prediction for cosmological structure formation is the existence of a shock bounding the hot, gaseous intracluster medium and a corresponding jump in the dark matter profile, both near the virial radius of the galaxy cluster (e.g., Bertschinger 1985; Lau et al. 2015). More recently, simulations by Diemer & Kravtsov (2014) (hereafter DK14) have

reinforced the expectation that the dark matter halo itself should exhibit a sharp density steepening near the virial radius (see also Adhikari, Dalal, & Chamberlain 2014).

The member galaxies of a cluster are expected to trace the cluster's dark matter profile in the cluster outskirts, as they are subject to similar collisionless dynamics; accordingly, we may expect to see such a feature not just in the dark matter profile but also in the galaxy density profile. Tully (2010) examined the distributions of the galaxies in the Coma and Virgo clusters and detected sharp density cut-offs at radii of 3 and 2 Mpc, respectively, from the cluster centers, which he identified with the caustics of second turnaround. These correspond roughly to the virial radii of these clusters (e.g., Kubo et al. 2007; Karachentsev et al. 2014). The analysis of Trentham & Tully (2009) identified a similar feature in the galaxy group NGC 1023.

More, Diemer, & Kravtsov (2015) mentioned that hints of such a jump may have been seen in other data sets. For instance, Tully (2015) measured the second turnaround radius, which is associated with the aforementioned density jumps, of several groups and clusters. Additionally, Rines et al. (2013) (hereafter R13) presented spectroscopic velocities for cluster members in 58 galaxy clusters, from which they reconstructed the density profiles, which appear to show a deficit of galaxies with respect to an NFW profile (Navarro, Frenk, & White 1997). However, they noted that their results at large radii from the cluster center may be affected by having few spectroscopically observed cluster members in the exterior regions.

In this paper, we focus on the R13 sample of clusters and use public data from the Sloan Digital Sky Survey (SDSS) (York et al. 2000) to select cluster members photometrically. Rather than use spectroscopic velocities, we construct the radial number

density profiles of member galaxies and fit them with two functional forms to examine whether we can detect a feature consistent with the predicted density jump in any of the individual clusters using available data sets. We intend to see if there is any evidence for such a feature in order to inspire future, detailed investigations of bias and systematics using simulations. Where applicable, we assume the standard ΛCDM cosmology with $\Omega_\Lambda = 0.73$ and $\Omega_m = 0.27$, consistent with the parameters selected by DK14 to enable direct comparison. To compare results across clusters we also use the measure R_Δ, which is the radius within which the mean mass density $\bar{\rho} = \Delta\rho_b(z)$, where ρ_b is a specified cosmological background density and Δ is the density contrast with respect to $\rho_b(z)$.

3.2 Data

3.2.1 SDSS Catalogs

To probe the existence of the density jump predicted by DK14, we focus our attention on the sample of 56 low-redshift ($0.1 < z < 0.3$) galaxy clusters from R13 (of their original 58 clusters, we do not include MS0906/A750 in our samples, since these clusters are nearly coincident and hence it is difficult to make a clean selection of member galaxies for each). Since their cluster sample was selected from regions of sky covered by SDSS, we use publicly available data from the most recent Data Release 12 (Alam, et al. 2015) to select cluster members.

We obtain photometric catalogs from the SDSS SkyServer SQL server[1]. For each

[1]http://skyserver.sdss.org/dr12/en/tools/search/sql.aspx

cluster, we query galaxies within 1.5 degrees of the cluster center (which, from R13, is the X-ray center) in both right ascension (RA) and declination. We further restrict our query to sources in the 'Galaxy' view with observed r-band magnitude between 14 and 22 and which have 'clean' photometry as determined by the SDSS pipeline. For each galaxy, we obtain the dereddened 'model' magnitudes (which we will use throughout the remainder of this work), corrected for Galactic extinction according to Schlegel, Finkbeiner, & Davis (1998) by the SDSS pipeline, and we also select photometric redshift estimates and associated redshift quality estimates from the 'Photo-z' table.

3.2.2 Cluster Member Selection

We will test two cluster member selections. The first, which we will refer to as Selection A, is based solely on photometry, primarily comprising red cluster galaxies selected from their location on a color-magnitude diagram but also including some galaxies with sufficiently secure photometric redshift estimates that are blueward of the red sequence. The second, which we call Selection B, folds in the spectroscopy of R13 to include additional cluster members and to reject some of the photometrically selected galaxies whose redshift estimates place them beyond the cluster. These selection procedures are outlined in more detail in the following sections.

Red Sequence Cluster Member Selection

Both of our methods of cluster member selection are based upon the target selection process of R13, which relied on the red sequence method of Gladders & Yee (2000). The red sequence refers to a linear feature in the color-magnitude diagram of galaxies

in a cluster field that arises from the population of red, early-type galaxies that have been observed to comprise the majority of cluster members. By selecting galaxies within a range around this line, we can obtain a sample of cluster members. As in R13, we construct a diagram of $g - r$ vs r and fix the slope of the red sequence line to -0.04. We then select the appropriate intercept by examining the distribution of galaxies within 5 arcminutes of the cluster center. We can also use the spectroscopic data publicly available from R13; by matching their spectroscopic catalogs to SDSS photometry, we can additionally calibrate our red sequence selection, as will be described in Section 3.2.2.

Having thus identified the linear red sequence feature, we select galaxies that are within an offset of 0.1 magnitude above the red sequence line, and 0.15 magnitude below the red sequence line, as illustrated in Figure 3.1. This is in contrast to the choice of ± 0.3 magnitude in the photometric target selection process of R13, which was found to be much wider than the actual red sequence as indicated by the spectroscopy. The asymmetry of the limits above and below the red sequence is motivated by the results of Section 5.2 and Figure 16 of R13, which suggest that there are fewer cluster members above the red sequence than below it, as confirmed by the righthand panel of Figure 3.1, which shows the distribution of spectroscopically confirmed members.

Since the red sequence method selects a specific population of galaxies, it is worth examining whether the exclusion of other types of galaxies in the cluster affects our result. The analysis of Dressler (1980), which examined the galactic populations of over 50 galaxy clusters, found that blue, late-type galaxies comprise a small fraction of the populations of rich galaxy clusters, although this fraction increases as the density of galaxies decreases. This is supported by the spectroscopic data provided by R13, who

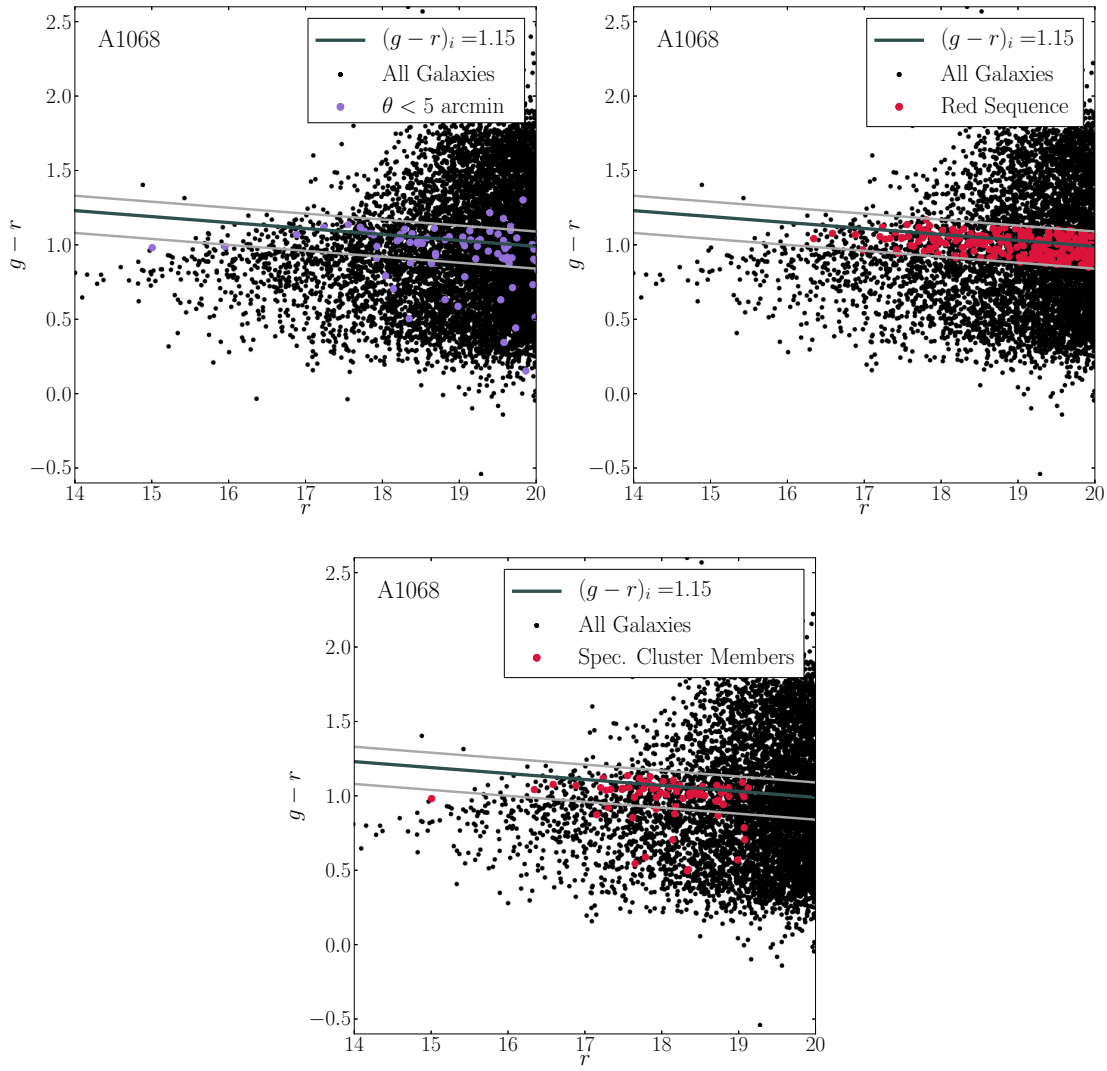

Figure 3.1.—: The red sequence cluster member selection for example cluster A1068. *Left*: in the color-magnitude diagram, we initially plot the location of galaxies within 5 arcminutes of the cluster center, which should be dominated by cluster members, to provide an indication of the red sequence. *Right*: The galaxies selected by the red sequence method using the limits described in Section 3.2.2; we plot the galaxies thus selected that are within 2.5 h^{-1}Mpc of the cluster center. The labelled intercept $(g-r)_i$ is selected to be the value at $r = 16$. *Bottom:* The cluster members as selected via the spectroscopy of R13, which can be used to verify the red sequence selection.

find that within the virial radius of the cluster the fraction of blue galaxies is $\lesssim 10\%$, while over the entire radial range for which they obtained spectra, the fraction is $\lesssim 15\%$.

Selection A

In Selection A, we add to the red sequence selection galaxies with photometric redshifts, primarily in order to also select cluster members that are blueward of the red sequence. We restrict our attention to galaxies that have secure photometric redshifts, as indicated by the 'photoErrorClass' (an SDSS quality marker that categorizes galaxies on the basis of their photometric errors) and 'zErr' tags; the former we select to be equal to 1, the highest class, and the latter we restrict to be less than 0.03, consistent with the photo-z scatter[2]. We then mark as additional cluster members galaxies that were not originally selected via the red sequence method and whose photometric redshift estimate is within 0.03 of the cluster redshift provided by R13.

The population of galaxies with photometric redshift estimates of sufficient quality as indicated by the SDSS pipeline is too small for most clusters to use as the basis for our analysis; within the central 1.5 h^{-1}Mpc, there are on average only about 60 galaxies with photometric redshifts satisfying $|z_c - z_g| < 0.03$ and subject to the above quality cuts, many of which were already picked up via the red sequence method. Additionally, basing a selection on these redshifts would exclude most cluster members with $r \gtrsim 19$. Accordingly, as noted above, we must combine them with the galaxies selected via the red sequence method. This final selection, denoted Selection A, for an example cluster is shown in the lefthand panel of Figure 3.2.

[2]http://www.sdss.org/dr12/algorithms/photo-z/

As an additional step in verifying our cluster member selection, we construct a projected radial density plot consisting of the total radial density profiles of all sources in our catalog (subject to $r < 20$) as well as the non-cluster density profile, computed by subtracting the counts of cluster members from the total number of galaxies in each bin. In the total profile, we expect to see a steep increase in galaxies at small radial distances that flattens out at large R. After subtracting out the contribution from these cluster members, the resulting non-cluster member profile should be roughly flat. Figure 3.3 shows these density plots for four example clusters, using Selection A.

Selection B

While neither the SDSS photometric redshifts nor the spectroscopy of R13 identify enough cluster members for our analysis, we can use this additional information to refine the red sequence selection in a second selection. As before, after selecting red sequence cluster members using the procedure outlined in Section 3.2.2, we add in bluer cluster members based on SDSS photometric redshifts as described in Section 3.2.2. However, in this case, we can further refine the selection by also rejecting cluster members if the SDSS photometric redshifts are sufficiently secure and the members in question have redshifts in the range $|z_c - z_g| < 0.03$, where z_c is the cluster redshift and z_g is the photometric redshift estimate.

We can use the spectroscopic data of R13 similarly. After matching their tables to the SDSS catalogs, we add in cluster members as identified by the spectroscopy and reject galaxies that were originally selected by the red sequence method or photometric redshifts but are identified as non-members by R13. This method of cluster member

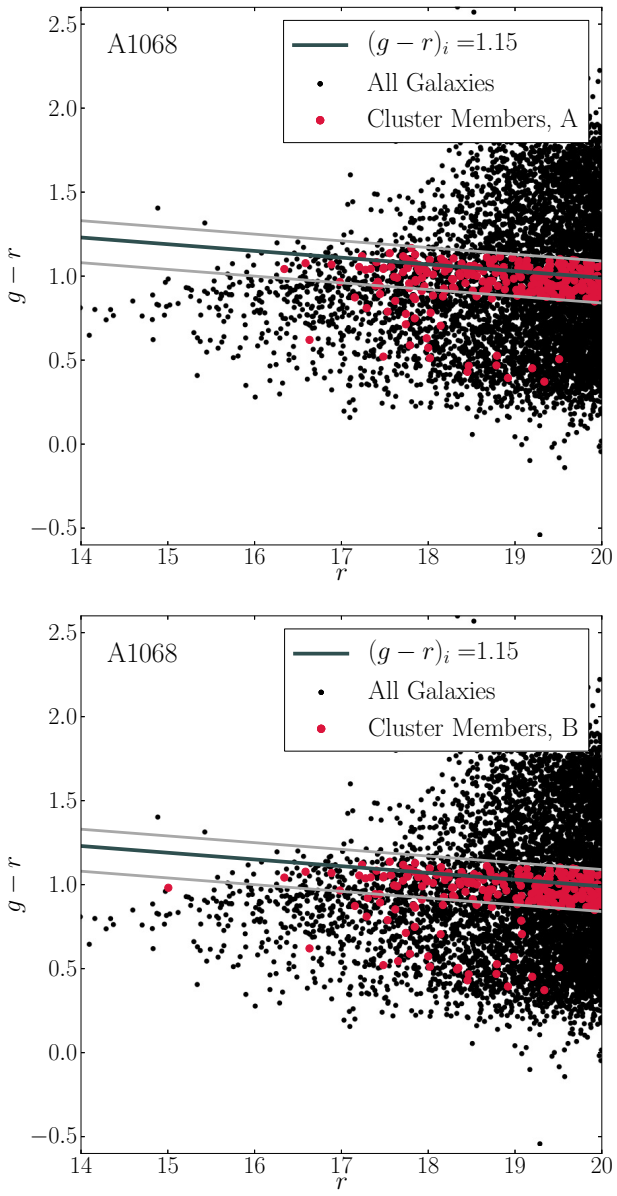

Figure 3.2.—: *Top:* The cluster member selection for example cluster A1068 using Selection A, which comprises galaxies selected using the red sequence method and galaxies with SDSS photometric redshifts, which add in some galaxies blueward of the red sequence. *Bottom:* The cluster member selection for this same cluster using Selection B, which combines the red sequence, photometric redshifts, and spectroscopic redshifts.

selection, which we term 'Selection B,' is summarized in the righthand panel of Figure 3.2. This selection is more observationally expensive than Selection A, so it is worth testing both methods to see whether the additional information makes a difference in the results. On average, the numbers of cluster members selected by these two methods differ by about 5% within 1.5 h^{-1}Mpc of the cluster center. We will test the effect of this selection on our analysis in Section 4.4.

We note, however, that both of our selection methods will still include some level of contamination, primarily arising from the red sequence selection, which cannot be wholly refined with the quantity of more secure data available. Nonetheless, we do not believe that this contamination will have a significant impact on positive results – that is, the contamination should not mimic the signature of the density jump, as the non-cluster member red sequence galaxies are expected to be distributed roughly uniformly over the sky. However, the contamination could potentially wash out a density jump if the background level approaches or exceeds the cluster density in the outskirts. This means that, while our results can suggest the existence of a potential density jump, the lack of a density jump feature in our data does not necessarily indicate that the cluster does not have such a feature but rather that the data are simply not clean enough to detect it.

3.3 Method

3.3.1 Approach

Our fiducial analysis relies on cluster members selected as described in Section 6.2, subject to a magnitude cut of $r < 20$. We determine the number counts of galaxies in

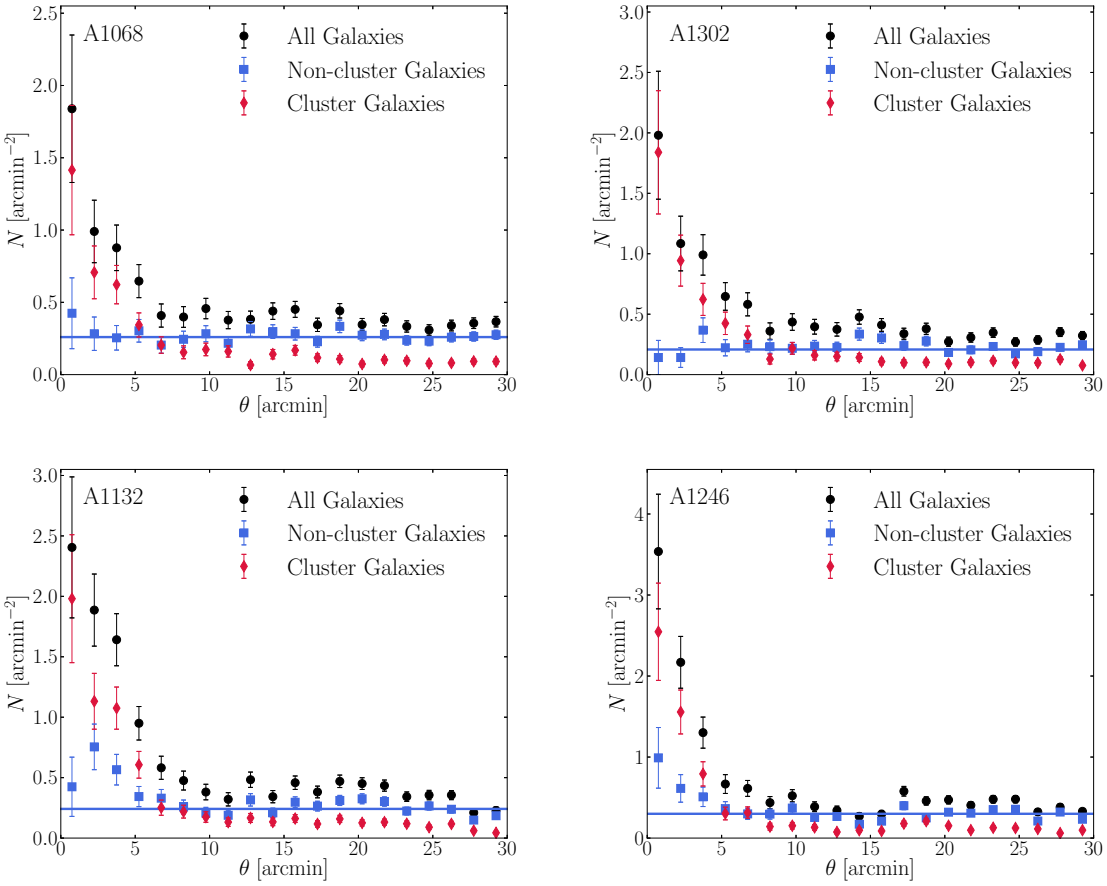

Figure 3.3.—: Plots of the projected densities of galaxies with $r < 20$ in four cluster fields: A1068, A1302, A1132, and A1246. Both the total galaxy density (black points) and the cluster density (red points) are expected to rise steeply towards the cluster center. The blue points show the density after removing cluster members from the total count, with a line drawn to indicate the average value beyond 20 arcminutes for comparison. The non-cluster galaxy distribution should be roughly flat if we have adequately selected cluster members, as for A1068 and A1302. A1132 and A1246, on the other hand, show some residual overdensity.

bins of 0.1 h^{-1}Mpc, from which we construct the projected number density profile of member galaxies, $N(R)$, with R indicating the projected radius, using the cluster centers listed in R13. We use Poissonian error bars.

We employ two methods to test for evidence of the density jump. The first is to try to detect a density jump in these profiles by fitting to them a cluster density model with a jump and compare it to a fit using a model without the jump. In the second, we avoid reference to a specific functional form and instead use non-parametric splines to see whether we can naturally extract a steepening of slope in the projected profiles, which would suggest the signature of a density jump.

In the first method, we fit the profiles using the fitting formula provided by DK14 to incorporate their predicted density steepening:

$$n_{\rm DK}(r) = n_{\rm in}(r)\left[1+\left(\frac{r}{r_t}\right)^{\beta}\right]^{-\frac{\gamma}{\beta}} + n_m\left[b_e\left(\frac{r}{5R_{200}}\right)^{-s_e}+1\right]. \tag{3.1}$$

As suggested by the results of the fits of DK14 to simulation data, we fix $\beta = 6$ and $\gamma = 4$, a choice that yields a dependence of r_t on the mass accretion rate, Γ:

$$r_t = \left(0.62 + 1.18e^{-2\Gamma/3}\right) \times R_{200} \tag{3.2}$$

We further select the NFW profile with two parameters, n_s and r_s, as our inner density profile $n_{\rm in}$:

$$n_{\rm NFW}(r) = \frac{n_s}{r/r_s\,(1+r/r_s)^2}. \tag{3.3}$$

We note that DK14 used the Einasto function (Einasto 1965) instead of the NFW for the inner profile, but in the regime of interest, the distinction between the two is negligible. We will refer to the model given by Equation 3.1 with $n_{\rm in}(r) = n_{\rm NFW}(r)$ as the 'Density

Jump' model, or 'DJ' model in abbreviation. We note that this model is a spherical one and thus may not be a good description of clusters undergoing mergers or featuring significant substructure, but there are only a few clusters potentially identified as such in R13, specifically A667, A773, A1758, A1902, A1914, and A2219, so that we do not expect this to have a significant impact on our analysis.

Since the density jump feature occurs around the virial radius, we use a fitting range of $R < 2R_{200}$, which is beyond the range that is typically fitted well by an NFW profile (we also exclude the inner $R < 0.1R_{\rm vir}$ in the fit, consistent with DK14). Accordingly, the two models that we will compare via fitting will be the DJ profile and a profile given by an NFW profile with an outer term:

$$n(r) = n_{\rm NFW}(r) + n_m \left[b_e \left(\frac{r}{5R_{200}} \right)^{-s_e} + 1 \right]. \tag{3.4}$$

These profiles are projected numerically and fitted to our galaxy density data. The free parameters in our fit are n_s, r_s, b_e, and s_e for both profiles; the full DJ formula has one additional free parameter, Γ. We restrict the fits to the range $0 < \Gamma < 5$ and to reasonable values of n_s (< 5000 gal/h^{-3}Mpc^3) and r_s, the latter of which is restricted by the value of the NFW concentration parameter, $c = R_{200c}/r_s$. Observations have suggested that this value is lower for galaxy profiles than for dark matter (e.g., Lin, Mohr, & Stanford 2004; Hansen et al. 2005; Budzynski et al. 2012), and we set the range as $2.0 < c < 6.0$ in our fits. We refer to the Appendix of DK14 for appropriate ranges for s_e $(0.5 - 2.0)$ and b_e $(0.1 - 4.0)$. We additionally fix n_m, which will be discussed further in Section 3.3.2, and we select as our upper limit of integration $R = 10R_{\rm vir}$, same as used by DK14.

We then examine the results of the fits using the Akaike Information Criterion

(AIC; Akaike 1974) and the Bayesian Information Criterion (BIC; Schwarz 1978), which provide a means of comparing models fitted to data. As the use of these methods in astrophysics and cosmology has been discussed in a number of papers (e.g., Takeuchi 2000; Liddle 2007; Broderick et al. 2011; Tan & Biswas 2012), we simply mention the most salient qualities here and refer the reader to these works for further details. To apply these criteria, we compute the following statistics for each fit:

$$\mathrm{AIC} = \chi^2 + 2p + \frac{2p(p+1)}{\mathcal{N} - p - 1}, \tag{3.5}$$

$$\mathrm{BIC} = \chi^2 + p\ln(\mathcal{N}), \tag{3.6}$$

where p is the number of parameters in the fit, $\mathcal{N}$ is the number of data points being fitted, and χ^2 is the standard minimized goodness-of-fit parameter. In the case of the AIC, we have also included a correction term of $2p(p+1)/(\mathcal{N} - p - 1)$ which is recommended for small values of $\mathcal{N}$ (Burnham & Anderson 2002, 2004). The model that is preferred by these criteria is the one with the lower IC = AIC, BIC value. If we compute $\Delta\mathrm{IC} = \mathrm{IC}_{\mathrm{high}} - \mathrm{IC}_{\mathrm{low}}$, then, roughly, values of $\Delta\mathrm{IC} = 1 - 5$ are indicative of 'positive' evidence in favor of the model with lower IC and values of $\Delta\mathrm{IC} > 5$ denote 'strong' evidence (e.g., Liddle 2007; Broderick et al. 2011).

Our second method consists of smoothing the profiles by fitting a smoothing cubic spline to our data. For a data set with measured values y_i and errors σ_i at a set of points r_i, the smoothing spline $f(r_i)$ is constructed to satisfy the condition

$$\sum_{i=1}^{N} \left(\frac{y_i - f(r_i)}{\sigma_i} \right)^2 \leq S, \tag{3.7}$$

where S is a constant that interpolates between smoothing and fitting: that is, when $S = 0$, the spline is forced to pass through every data point, so that there is no

smoothing, whereas as S is increased, the curve becomes smoother at the expense of the fit (de Boor 2001). Reinsch (1967) argues that the smoothing parameter S should be chosen in the range $\mathcal{N} - \sqrt{2\mathcal{N}} \leq S \leq \mathcal{N} + \sqrt{2\mathcal{N}}$, where $\mathcal{N}$ is the number of data points over which we construct the spline, if the σ_i are estimates of the standard deviation in y_i. We accordingly choose three values within this range to compare to an NFW fit: $S = \mathcal{N} - \sqrt{2\mathcal{N}},\ \mathcal{N},\ \mathcal{N} + \sqrt{2\mathcal{N}}$. The NFW model is expected to be a good fit to the inner parts of the profile, so we use the analytical expression for the projected NFW density (e.g., Wright & Brainerd 2000) to fit the cluster galaxy density profiles within R_{200}, establishing the values of n_s and r_s. We then calculate the logarithmic derivative $d\log(N)/d\log(R)$ of the splines for each cluster to test for the presence of the density jump feature, comparing it to the logarithmic derivative of the NFW fit.

3.3.2 Fixed Parameters

As noted in Section 6.1, we define measures of cluster size such that the mean mass density inside the radius R_Δ is $\bar{\rho} = \Delta\rho_b(z)$; commonly used values are R_{500} and R_{200}. The other quantity that needs to be specified is the background density $\rho_b(z)$; one choice often used in observational work is the critical density $\rho_c(z) \equiv 3H(z)^2/8\pi G$, where $H(z)$ is the Hubble parameter at redshift z, which is given by $H(z)^2 = H_0^2\left[\Omega_m(1+z)^3 + \Omega_\Lambda\right]$ with $H_0 = 100\ h$ km/s/Mpc. Another choice is to use the mean matter density $\rho_m(z) = \rho_c(z)\Omega_m(z)$, where $\Omega_m(z) = \Omega_m(1+z)^3/\left[\Omega_m(1+z)^3 + \Omega_\Lambda\right]$, which is used with $\Delta = 200$.

As noted above, DK14 use the mean matter density $\rho_m(z)$ to define the radius $R_{200} = R_{200m}$ used in the fitting formula given by Equation (3.1). However, R13 measures

$R_{200} = R_{200c}$ for their sample of clusters using the critical density as reference, so we need to convert their measure to that of DK14. To do so, we note that a given mean density $\bar{\rho}$ may be written in two ways:

$$\bar{\rho} = \Delta_c \rho_c(z) = \Delta_m \rho_m(z). \tag{3.8}$$

If we specify that $\rho = \rho_{\rm NFW}$, then in the outskirts of the cluster (i.e., including near R_{200}), we have:

$$\bar{\rho}(R_\Delta) \propto \frac{1}{R_\Delta^3}. \tag{3.9}$$

Combining this relation with Equation (3.8) yields

$$\frac{R_{200m}}{R_{200c}} = \left(\frac{1}{\Omega_m(z)}\right)^{1/3}. \tag{3.10}$$

For $z = 0.1 - 0.3$, this implies that

$$R_{200m} \approx 1.4 \times R_{200c}. \tag{3.11}$$

Accordingly, for simplicity, we will henceforth refer to R_{200m} as R_{200}, and the values from R13 will be converted to this measure using Equation (3.11).

Lastly, we need to establish an appropriate value for n_m. We note that the original prescription of DK14 defines Equation (3.1) in terms of mass densities ρ rather than number densities n, and their fitting results assume a fixed value of $\rho_m(z) = \rho_c(z)\Omega_m(z)$. The translation into a number density needs to take into account the impact of the primary selection function by which we obtain cluster members, the red sequence method. In the absence of a cluster, this method would select a population of galaxies that lies in the appropriate region of color-magnitude space; in this case, the projected density of these galaxies is expected to be roughly constant across the field of view.

Recalling the outer profile term of Equation (3.1),

$$n_{\rm out}(r) = n_m \left[b_e \left(\frac{r}{5R_{200}} \right)^{-s_e} + 1 \right], \tag{3.12}$$

we can analytically determine the contribution to the surface density of the last, constant term. The surface density is the line-of-sight integral,

$$N(R) = 2 \int_R^\infty \frac{n(r) r}{\sqrt{r^2 - R^2}} dr; \tag{3.13}$$

this integral diverges for a constant $n(r)$. However, in practice we must truncate this integral at some maximum radius $R_{\rm max}$. As noted above, DK14 use $R_{\rm max} = 10R_{\rm vir} \approx 9R_{200}$. In that case,

$$N_m(R) = 2n_m \int_R^{9R_{200}} \frac{r}{\sqrt{r^2 - R^2}} dr, \tag{3.14}$$

$$N_m(R) = 18 n_m R_{200} \sqrt{1 - \left(\frac{R}{9R_{200}} \right)^2}. \tag{3.15}$$

For the scales of interest in our fits, $R \lesssim 2R_{200}$ (and even a bit beyond), this value is roughly constant near the value at $R = 2R_{200}$,

$$N_m \approx 17.6 n_m R_{200}. \tag{3.16}$$

The redshift dependence of N_m can be determined by applying the red sequence method in test fields that are not centered on low redshift clusters. If we select a population of galaxies with this method, then we can construct the projected density in a given radial bin i as

$$N_{m,i} = \frac{\mathcal{N}_i}{\pi \left(R_{i,\rm max}^2 - R_{i,\rm min}^2 \right)}, \tag{3.17}$$

$$= \frac{1}{D_A(z)^2} \left[\frac{\mathcal{N}_i}{\pi \left(\theta_{i,\rm max}^2 - \theta_{i,\rm min}^2 \right)} \right], \tag{3.18}$$

where $\mathcal{N}_i$ is the number of galaxies in the ith bin and $D_A(z)$ denotes the angular diameter distance. We expect that the angular projected density (the term in brackets) over the radial range is a roughly constant value, which we denote by η. Then

$$N_m(z) = \frac{\eta}{D_A(z)^2} = \frac{\eta(1+z)^2}{D_c(z)^2}, \tag{3.19}$$

where D_c is the comoving distance, which at the small redshifts considered here, is given by $D_c(z) \approx (c/H_0)z$. Upon setting $\tilde{\eta} = \eta/(c/H_0)^2$, we have:

$$N_m(z) = \tilde{\eta}\frac{(1+z)^2}{z^2}. \tag{3.20}$$

To obtain the value of $\tilde{\eta}$, we apply our red sequence cuts in random test fields from SDSS (also subject to our initial magnitude cut of $r < 20$) and fit N with the above function. This yields $\tilde{\eta} \approx 0.08\ h^2\ \mathrm{Mpc}^{-2}$.

Accordingly, combining Equation (3.16) with (3.20), we find that:

$$n_m(z, R_{200}) = \frac{4.55 \times 10^{-3}}{R_{200}}\frac{(1+z)^2}{z^2}. \tag{3.21}$$

We fix this value individually for each cluster using its measured redshift and R_{200} (the latter converted as discussed above) from R13. This equation sets the background red sequence level and its applicability can be verified by examining the large R behavior of our fits in Section 4.4.

3.4 Results

3.4.1 Fitting

The results of fitting the projected number density profiles with Equations (3.1) and (3.4) are summarized in Table 3.1 for both the fiducial method and variations, the latter

of which will be discussed in the next section. We note that the DJ model will always show a density jump-like feature if the parameters are constrained to their indicated values as in Section 3.3.1. However, as the DJ model has one additional parameter than the NFW+Outer model, we then compare the two fits using the AIC and BIC, which can test whether the improvement in the fit is significant given the addition of this parameter. We compute, in each case, $\Delta\mathrm{IC} = \mathrm{IC}_{\mathrm{NFW+O}} - \mathrm{IC}_{\mathrm{DJ}}$. Since lower values of IC are favored, this quantity will be positive if the criteria indicate evidence in favor of the DJ model. In Table 3.1, we thus first list in the column, '% $\chi^2_{\mathrm{DJ}}/\mathrm{ndf} < \chi^2_{\mathrm{NFWO}}/\mathrm{ndf}$,' the number of galaxy clusters for which the reduced χ^2 is lower for the DJ model and second the number of galaxy clusters whose fits pass a general quality cut, including requiring that $\chi^2/\mathrm{ndf} < 3$ for the DJ model and a more generous $\chi^2/\mathrm{ndf} < 5$ for the other. The next two columns indicate how many clusters have $\Delta\mathrm{IC} = \mathrm{IC}_{\mathrm{NFW+O}} - \mathrm{IC}_{\mathrm{DJ}} > 0$ for each criterion, which would suggest evidence in favor of the DJ model. The last two columns indicates how many clusters have one of the $\Delta\mathrm{IC} > 5$, indicating strong evidence in favor of this model.

Our fiducial method uses a binning of $\Delta R = 0.1\ h^{-1}$Mpc and employs a magnitude cut of $r < 20$. We use two selection methods to identify cluster members; as discussed in more detail in Section 6.2, Selection A is based on SDSS photometry and Selection B refines the first with R13 spectroscopy. Using Selection A, only about 13% (7 clusters) of the original 56 clusters have both $\Delta\mathrm{IC} > 5$. We see that refining the cluster member selection yields a higher number of clusters for which the DJ model is a better description than a simple NFW model with an outer term, with about 25% of these clusters having both $\Delta\mathrm{IC} > 5$. However, the results of individual clusters are consistent between the selection methods – the seven clusters with the strongest evidence in favor of the density

jump using Selection A (A655, A1033, A1246, A1437, A1689, A1914, and A2034) continue to have $\Delta\mathrm{IC} > 5$ using the second selection. These clusters (along with the more marginal case A1835, which has only one $\Delta\mathrm{IC} > 5$ using Selection A) are shown in Figure 3.4 for Selection A fits and Figure 3.5 for Selection B; however, using Selection B several other clusters also reveal strong (and for some even stronger) evidence for a density jump. In both cases, the cluster with the strongest evidence for a density jump is A1689.

Furthermore, the increase in the number of clusters with IC evidence in favor of the DJ model using Selection B suggests that it may be beneficial to investigate these profiles further with a cleaner cluster member selection, with either a sample of galaxies with high-quality photometric redshift estimates or with a sufficiently dense sample of galaxies with secure spectroscopic redshifts. Additionally, a few of these clusters (particularly A1246) show some residual overdensity at roughly $\theta < 5'$ of the cluster center after the cluster member selection (c.f. Figure 3.3), which could be indicative either of having missed some population of galaxies in our selection or that there are some other agglomerations of galaxies along the line of sight that contribute to the overdensity. Other clusters, like A655, have some additional features in their density profiles at large R, which could be indicative of infalling groups of galaxies. High-quality, dense redshift estimates would help resolve these ambiguities.

We additionally test the fits by making the radial bins twice as large ($\Delta R = 0.2\ h^{-1}\mathrm{Mpc}$). In this case, the reduced χ^2 values are a bit worse for Selection A, as indicated in Table 3.1. We find that the larger binning yields the greatest drop in the number of clusters with evidence favorable towards the DJ model using the AIC; the BIC results, however, are virtually unchanged from the earlier case. The discrepancy

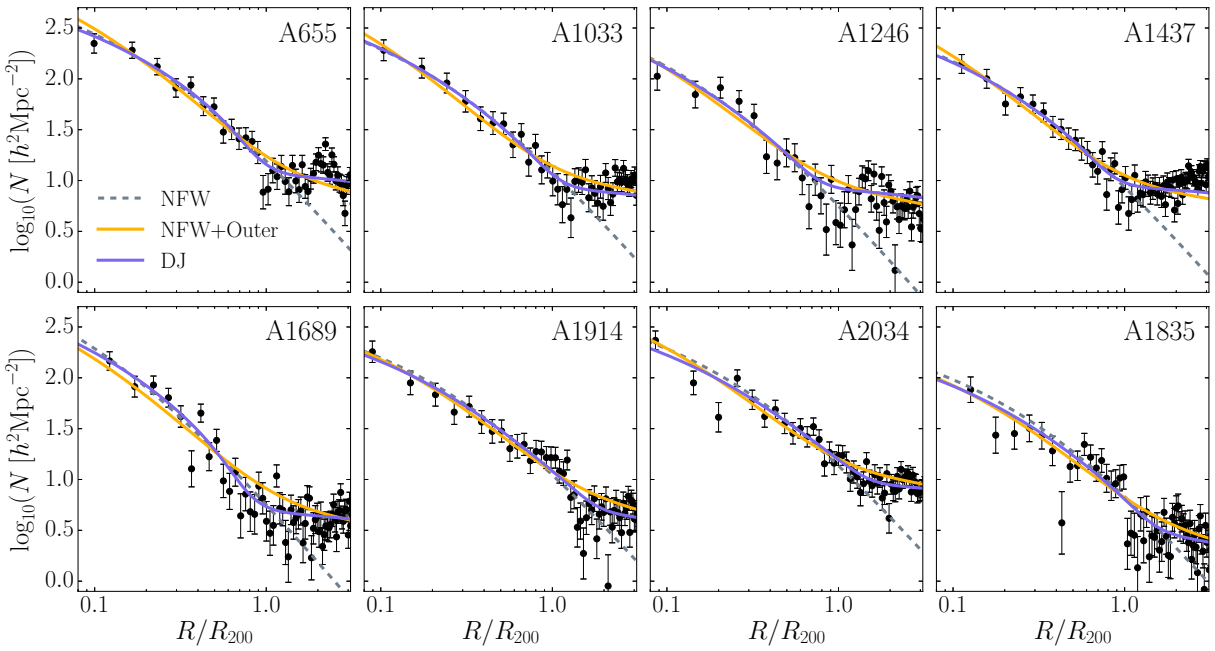

Figure 3.4.—: Plots of the projected number density profiles for the 8 clusters with the highest ΔAIC and ΔBIC values in the fiducial analysis using Selection A. Three fitted functions are shown: a base NFW, fitted interior to R_{200}, an NFW+Outer model, given by Equation (3.4) and fitted interior to $2R_{200}$, and the full Density Jump model given by Equation 3.1 with an inner NFW profile, fitted interior to $2R_{200}$.

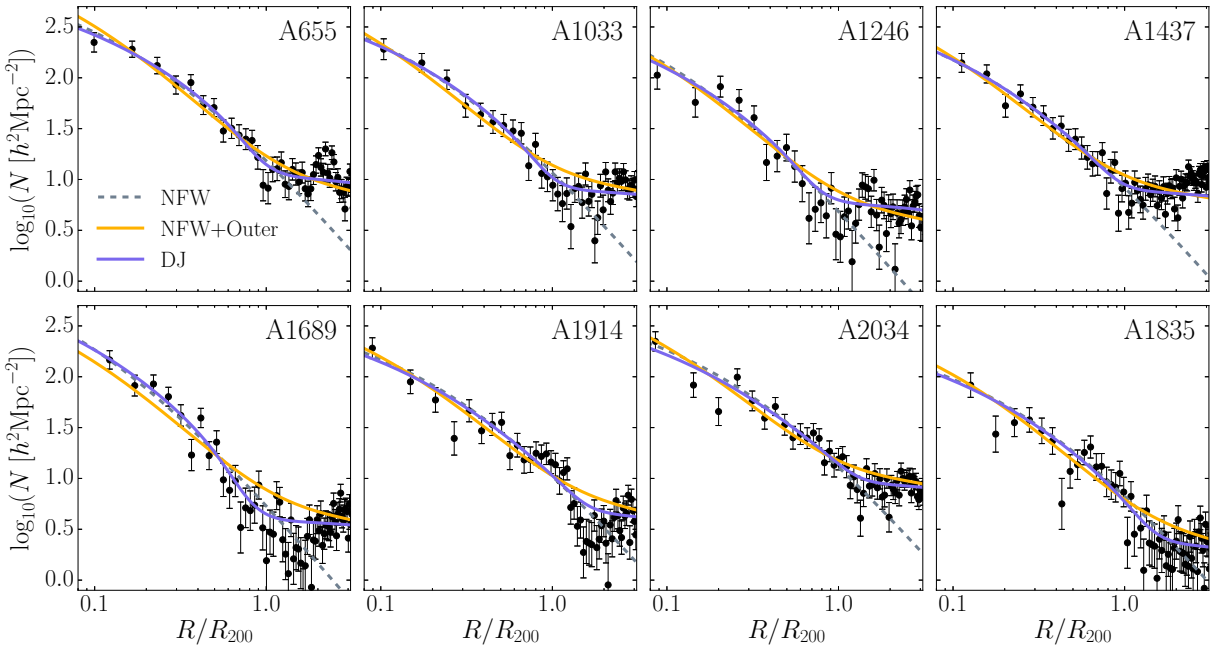

Figure 3.5.—: Plots of the projected number density profiles for the 8 clusters with $\Delta\mathrm{IC} > 5$ using both selection methods, with fits shown for the profiles constructed using Selection B. The curves are the same as in Figure 3.4.

is likely caused by the smaller number of data points over which we fit relative to the number of parameters, which affects the correction term for the AIC.

Lastly, we examine the effects of possible small miscentering on our results. We take the eight clusters in Figure 3.4 and redo the fiducial Selection A analysis after shifting the centers of each cluster by roughly 50 kpc, approximately the radius of a brightest cluster galaxy. We find that all 8 clusters continue to have $\Delta\mathrm{IC} > 0$, and 7 have both $\Delta\mathrm{IC} > 5$. A1835, the already the marginal case in the original analysis, ends up with both $\Delta\mathrm{IC} \sim 2 - 3$. This suggests that our strong results are stable with respect to small errors in the centering of the cluster.

3.4.2 Smoothing Splines

In addition to fitting the projected galaxy density profiles with Equations (3.1) and (3.4), we also fit a smoothing cubic spline as described in Section 3.3.1. This latter approach has the benefit of being model-independent; we use the spline fits to construct a smooth logarithmic derivative of the profile to test for the existence of a density jump.

First, to provide context for the spline results, in Figure 3.6, we plot the DJ model at fixed $\Gamma = 4$ for various redshifts, which determine n_m, and for an example fixed

Table 3.1:: Information Criteria Results

Method	% $\chi^2_{\mathrm{DJ}}/\mathrm{ndf} < \chi^2_{\mathrm{NFWO}}/\mathrm{ndf}$	$\Delta\mathrm{AIC} > 0$	$\Delta\mathrm{BIC} > 0$	$\Delta\mathrm{AIC} > 5$	$\Delta\mathrm{BIC} > 5$	Both > 5
Fiducial, Sel. A	38/56	18	22	8	7	7
Fiducial, Sel. B	43/56	32	32	16	20	14
$\Delta R = 0.2\,h^{-1}$Mpc, Sel. A	34/55	12	22	5	7	5

redshift $z = 0.15$, we also show the variation with Γ. The bottom panel of each plot shows the corresponding logarithmic derivatives. The effect of the redshift dependence is to make the density jump steeper at higher redshift due to the lower background n_m. At a fixed n_m, a smaller value of Γ means a shallower density jump, whose maximum amplitude slope is attained at larger radii, although the values of b_e and s_e, which are free parameters in our fits, also contribute to the variation in the amplitude.

Figure 3.6 can be compared to Figure 13 of DK14. While the behavior of the density jump is qualitatively the same, we note that in our analysis, the maximum slope amplitudes are smaller than those predicted by DK14 due to the elevated background; accordingly, in our case the maximum slope amplitudes are governed not only by the mass accretion rate Γ but also the redshift of the cluster. However, the density jump location also depends on Γ.

Accordingly, we model our spline fits on Figure 3.6. We show the cubic spline fits for the same subset of clusters selected via the information criteria in the fiducial analysis. Figure 3.7 shows the spline fits for Selection A, while Figure 3.8 is its counterpart for Selection B. The spline fits do appear to pick up a modest steepening of slope, consistent with the low redshift of these clusters. Since at low redshift we can expect to almost exclusively detect very large density jumps ($\Gamma \approx 5$), which are likely uncommon, it is perhaps not surprising that the number of clusters for which the information criteria suggest strong evidence for the jump is fairly low.

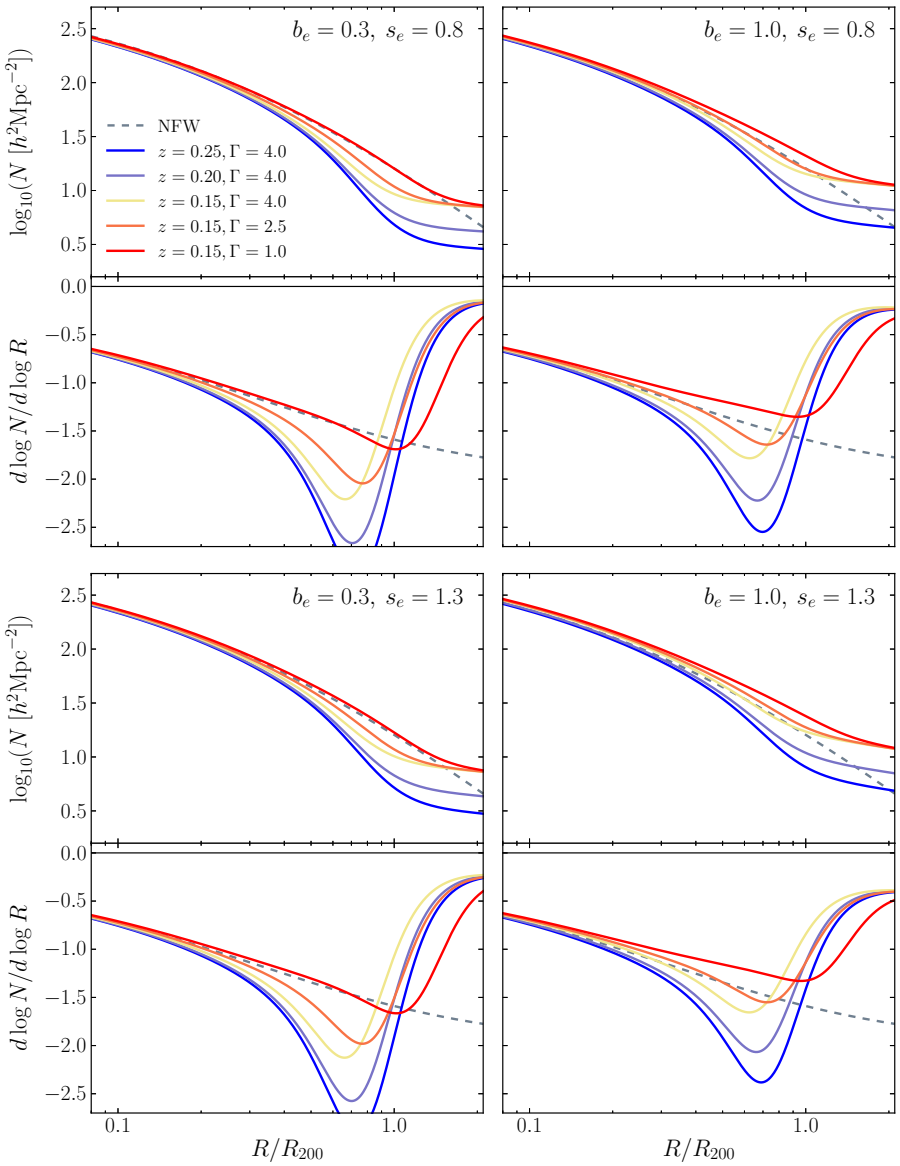

Figure 3.6.—: The projected density jump is a steepening of slope that can be analyzed using the logarithmic derivative of the DK14 model for four combinations of s_e and b_e values. The redshift dependence enters via $n_m(z, R_{200})$ as given by Equation (3.21), and we show the result for three values of z in the range of the R13 clusters at fixed $\Gamma = 4$. For the $z = 0.15$ case we also show the variation of the profile with Γ. An NFW profile (dashed) is drawn for comparison. All other model parameters are fixed.

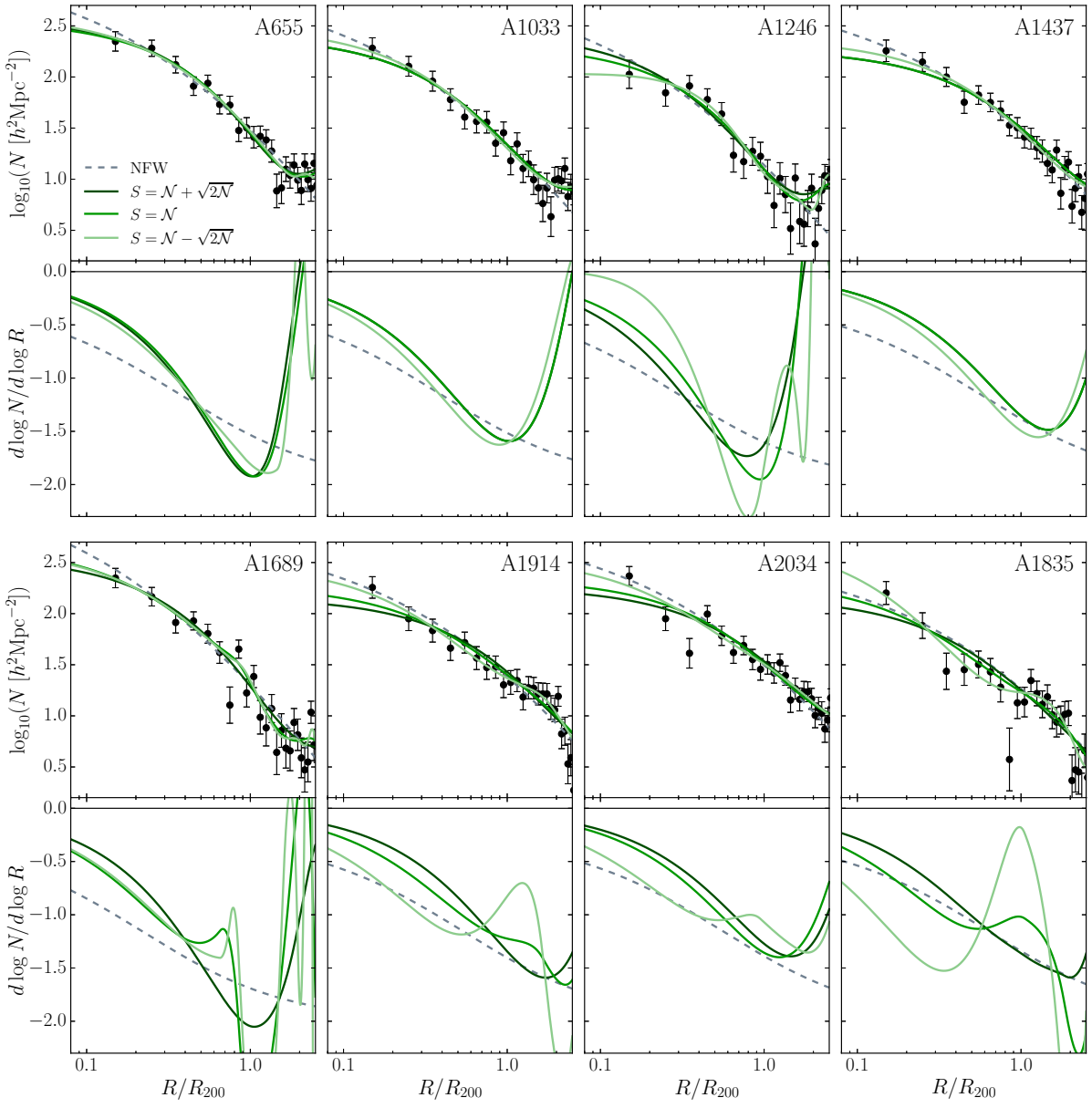

Figure 3.7.—: The top panel shows spline fits for various values of the smoothing parameter $\mathcal{S}$ for the clusters in Figure 3.4. The lower panel displays the logarithmic derivatives of the splines. An NFW fit and its logarithmic derivative (dashed line) are shown for comparison.

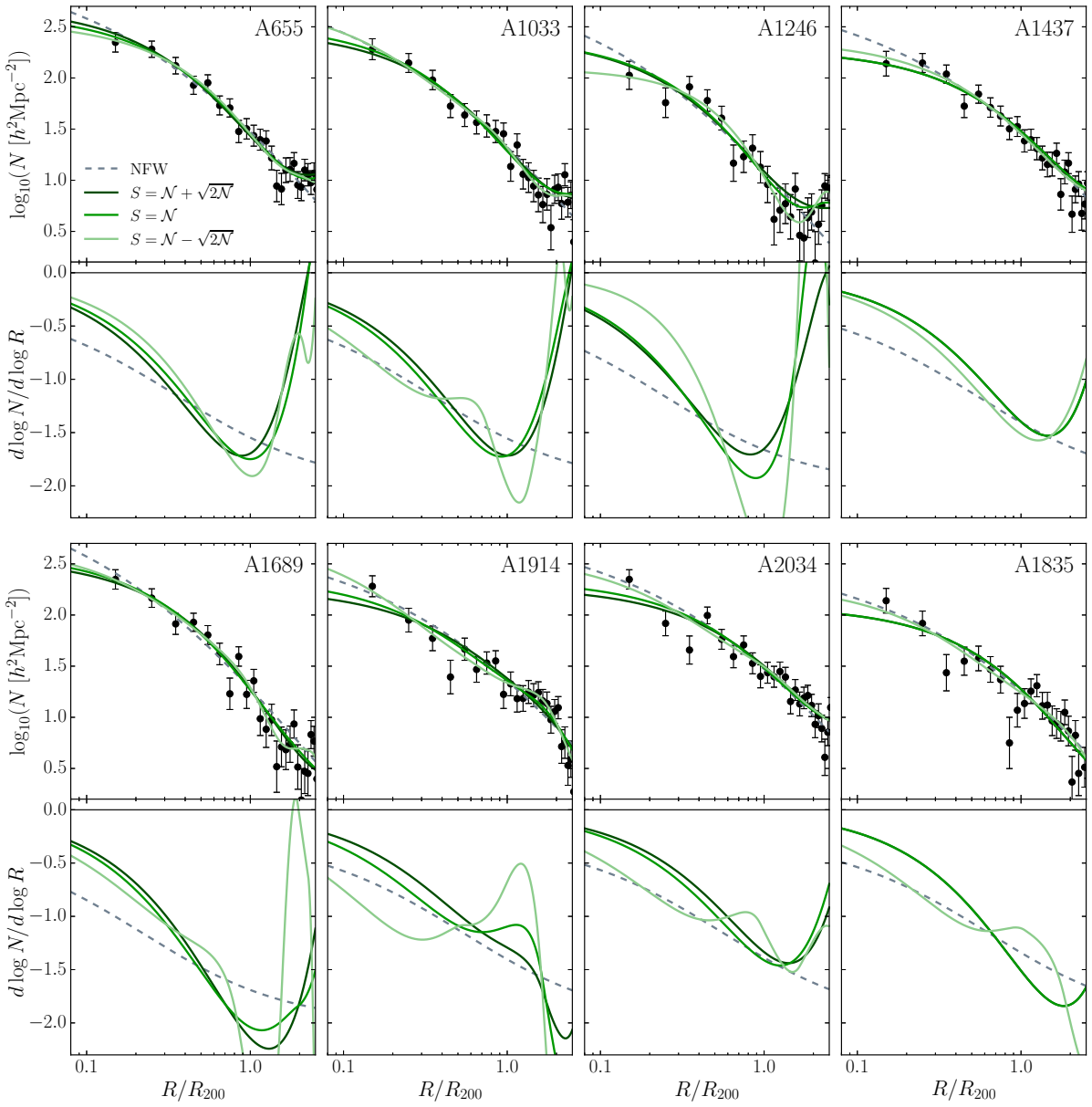

Figure 3.8.—: Same as Figure 3.7, but for Selection B profiles.

3.5 Discussion

We have tested whether cluster galaxy density profiles show evidence for a density jump feature near the virial radius using two methods: profile fitting and spline smoothing. We have examined the evidence in favor of the presence of a steep density jump in the galaxy density profiles of clusters, and also investigated the results via spline smoothing.

There does appear to be some dependence of our results on cluster redshift. In our fiducial analysis of Section 3.4.1, the seven clusters that showed strong evidence (both $\Delta\mathrm{IC} > 5$) for the density jump using Selection A spanned the redshift range of roughly $z = 0.1 - 0.2$, which omits the higher redshift clusters (although an eighth cluster, A1835, with one $\Delta\mathrm{IC} > 5$ value, is at $z = 0.25$). However, employing Selection B enlarges the sample of strong evidence clusters, and extends this to about $z = 0.1 - 0.25$, effectively the entire range of R13. More massive clusters tend to show stronger evidence for a density jump: these same 8 clusters have virial masses in the range $M_{\mathrm{vir}} = (2 - 11) \times 10^{14}\, h^{-1} M_{\odot}$, while a significant fraction of the clusters in the R13 sample have $M_{\mathrm{vir}} = (0.3 - 2) \times 10^{14}\, h^{-1} M_{\odot}$ (and may also be considered galaxy groups). This trend continues even when considering the additional clusters that pass the criteria using Selection B. This behavior can be expected, as higher mass clusters tend to have higher values of Γ and their profiles are likely to be better sampled than lower mass systems.

We see variations based on the cluster member selection. Our primary selection uses only photometric data, but redoing the analysis with the inclusion of the R13

spectroscopy does shift the results; in particular, the refined selection yields a larger sample of clusters that show some evidence for the jump. This suggests that additional data is required to make a firm detection of the density jump. This additional data could be in the form of dense spectroscopy out to large radii of cluster member galaxies, building upon the R13 catalog, which would provide the most secure cluster member determination. Otherwise, high-quality photometric redshifts could also improve upon our estimates.

Additionally, it is worth noting that in interpreting these results it is necessary to keep in mind some of the other factors that can impact the jump signature. In particular, cluster asphericity and contamination by other small groups and clusters along the line of sight can contribute to a diminishing of the jump signal. The latter of these can be addressed with redshift estimates. For the first, we note that the signature of the jump becomes more pronounced and thus easier to detect when Γ is large; however, clusters with large values of Γ may be more likely to have disturbed shapes and substructures, which when examined in projection could obscure the signature of the density jump.

More generally, it would be useful to compare the results in Table 3.1 to simulations. Mock halo catalogs could give an indication of the conditions needed for a cluster to show a discernible jump and thus the fraction of clusters in which we can expect to find this signature, which would provide context for the fractions we find using observational data. While this is a promising avenue for future analyses, such a comparison is beyond the scope of this work.

3.6 Summary and Conclusions

Using the cluster sample of R13 and optical data from SDSS, we have searched for the signature of a density jump feature near the virial radius ($\sim R_{200}$) predicted by the simulations of DK14. Our fiducial analysis selects cluster members from SDSS photometric catalogs using the red sequence method and photometric redshifts, and compares this to a selection refined by the inclusion of the spectroscopy of R13. After constructing the radial density profiles of the clusters, we fit two models, one with a density jump — Equation (3.1) — and one without — Equation (3.4) — and used the Akaike and Bayesian Information Criteria (AIC and BIC) to examine the evidence in favor of the density jump model. These criteria indicate that, using our fiducial methods, at least 10% showed strong evidence (ΔIC > 5) for the model that includes a density jump. The clusters with strong evidence for the density jump tend to have a higher mass ($M_{\rm vir} \gtrsim 2 \times 10^{14} h^{-1} M_{\odot}$), as expected. The cluster with the strongest evidence for the jump in this sample is Abell 1689.

We examined varying some of the parameters in our analysis. We find that using a larger bin size yields fewer clusters with strong evidence (if we stipulate a strong result for both criteria; the AIC appears to be most affected by the binning) for the density jump. However, if we require only one of the information criteria to yield strong evidence, then we are in excellent agreement with the fiducial analysis. We also probed the effects of possible small errors in centering; these were found to have negligible effect on our results.

We additionally tested our results using cubic smoothing splines. The spline

analysis appears to indicate some steepening of slope in these clusters, but these tend to be modest, suggesting the comparison to the theoretical predictions of DK14 may be complicated by background and projection effects. In the case of the former, a high background can diminish the signal, while the latter acknowledges that since clusters can have diverse shapes, the density jump is not necessarily localized at a single radius, which can lead to modifications of the signal in projection.

Finally, varying the cluster member selection methods does appear to have an effect on the results; in particular, including the most secure cluster member indicators (spectroscopic redshifts) increases the number of clusters for which we have strong evidence in favor of a model with a density jump. Thus, our conclusions are limited by the availability of data for the identification of galaxy cluster members. While the red sequence method provides a means of identifying the majority of cluster members, which tend to be red, early type galaxies, it does not readily provide a means of rejecting interloping red galaxies from higher redshifts or for including the smaller population of member galaxies blueward of the red sequence. While the spectroscopic observations of R13 provide an excellent start, it would be useful to extend their samples with additional redshift estimates to improve the completeness in the cluster outskirts, mitigating observational selection effects that can mimic a density steepening.

Accordingly, at present, neither the extant photometry nor spectroscopy of these clusters provides adequate numbers of confirmed member galaxies out to sufficiently large radii to significantly improve upon our methods. However, in order to better constrain the density jump feature and precisely determine its amplitude and position, future efforts will require either secure photometric redshifts or additional spectroscopy to refine the cluster galaxy density profiles. Future work using mock halo catalogs could

help pinpoint the conditions under which clusters can be expected to show a discernible density jump to help guide these observational endeavors.

3.7 Acknowledgments

We are very grateful to Andrey Kravtsov and Benedikt Diemer for their detailed and helpful comments on a draft of this paper. We would also like to thank the staff of helpdesk@sdss.org for advice regarding downloading data from SDSS.

This work was partly supported by the National Science Foundation Graduate Research Fellowship under Grant No. DGE-1144152. This work was also supported by NSF Grant No. AST-1312034. This work relied on tools from Numpy (van der Walt, Colbert, & Varoquaux 2011), Scipy (Oliphant 2007), and Matplotlib (Hunter 2007), as well as ROOT (http://root.cern.ch/).

This paper relies on data from SDSS-III. Funding for SDSS-III has been provided by the Alfred P. Sloan Foundation, the Participating Institutions, the National Science Foundation, and the U.S. Department of Energy Office of Science. The SDSS-III web site is http://www.sdss3.org/.

SDSS-III is managed by the Astrophysical Research Consortium for the Participating Institutions of the SDSS-III Collaboration including the University of Arizona, the Brazilian Participation Group, Brookhaven National Laboratory, Carnegie Mellon University, University of Florida, the French Participation Group, the German Participation Group, Harvard University, the Instituto de Astrofisica de Canarias, the Michigan State/Notre Dame/JINA Participation Group, Johns Hopkins University,

Lawrence Berkeley National Laboratory, Max Planck Institute for Astrophysics, Max Planck Institute for Extraterrestrial Physics, New Mexico State University, New York University, Ohio State University, Pennsylvania State University, University of Portsmouth, Princeton University, the Spanish Participation Group, University of Tokyo, University of Utah, Vanderbilt University, University of Virginia, University of Washington, and Yale University.

Chapter 4

Quantifying the Color-Dependent Stochasticity of Large-Scale Structure

Anna Patej & Daniel Eisenstein, accepted for publication in *Monthly Notices of the Royal Astronomical Society* (2016)

4.1 Introduction

Large-scale galaxy redshift surveys such as the Sloan Digital Sky Survey (SDSS-III DR12; Alam, et al. 2015) use the distribution of galaxies in the universe to constrain cosmological parameters in a manner complementary to other cosmological probes, including measurements of the cosmic microwave background (e.g., Ade et al. 2015) and supernovae (e.g., Suzuki et al. 2012). Within the scope of galaxy redshift surveys,

major projects like SDSS-III's Baryon Oscillation Spectroscopic Survey (BOSS; Dawson et al. 2013) as well as future experiments like the Dark Energy Spectroscopic Instrument (DESI) (Levi et al. 2013) target specific types of galaxies: luminous red galaxies (LRGs), and LRGs and emission line galaxies (ELGs), respectively. Accordingly, a key source of systematic uncertainty in these surveys is the knowledge of the extent to which the subset of galaxies observed probes the large-scale structure of the universe.

Local bias argues for a minimal level of stochasticity on large scales (Coles 1993; Scherrer & Weinberg 1998) and investigations of halo clustering suggest that halos of different masses do roughly trace the same large-scale structure (e.g, Seljak & Warren 2004; Hamaus et al. 2010). Accordingly, we may expect galaxies to be roughly non-stochastic (e.g., Tegmark & Bromley 1999). An informative test of these predictions can be obtained by measuring whether red and blue galaxies trace the same large-scale structure. The mathematical framework of this question can be developed straightforwardly using the concept of a fractional overdensity field,

$$\delta(\mathbf{x}) = \frac{\rho(\mathbf{x})}{\bar{\rho}} - 1. \tag{4.1}$$

In the simplest scenario, we can relate the distribution of red and blue galaxies to this underlying matter distribution via linear, deterministic bias parameters as:

$$\delta_b(\mathbf{x}) = b_b\delta(\mathbf{x}), \quad \delta_r(\mathbf{x}) = b_r\delta(\mathbf{x}), \tag{4.2}$$

from which it is possible to compute the correlation function as $\xi(\mathbf{R}) = \langle\delta(\mathbf{x})\delta(\mathbf{x}+\mathbf{R})\rangle$.

Combined with Equation (4.2), this yields the relations:

$$\xi_{bb}(\mathbf{R}) = b_b^2 \xi(\mathbf{R}), \tag{4.3}$$

$$\xi_{rr}(\mathbf{R}) = b_r^2 \xi(\mathbf{R}), \tag{4.4}$$

$$\xi_{br}(\mathbf{R}) = b_b b_r \xi(\mathbf{R}). \tag{4.5}$$

Taking the square root of the ratios of the autocorrelations yields estimates of the relative bias $b_{\rm rel}$ between red and blue galaxies (e.g., Croton et al. 2007; Coil et al. 2008; Guo et al. 2013; Skibba et al. 2014). Constructing the correlation coefficient, r_ξ, we find:

$$r_\xi \equiv \frac{\xi_{br}}{\sqrt{\xi_{bb}\xi_{rr}}} = 1. \tag{4.6}$$

However, the formalism of Equation (4.2) has several obvious failures, one of which is that it permits values of $\delta_b, \delta_r < -1$ if $b_b, b_r > 1$, and so must be superseded by a more realistic model. To this end, we follow Dekel & Lahav (1999) in defining, for $g = b, r$,

$$\epsilon_g(\mathbf{x}) \equiv \delta_g(\mathbf{x}) - b_g \delta(\mathbf{x}), \tag{4.7}$$

a random bias field that introduces stochasticity into the relations between the two galaxy samples. In this case, if we calculate the correlation coefficient, we see that $r_\xi \neq 1$.

The key to discerning the presence of stochasticity, then, is the measurement of the correlation coefficient. We use pair counting to calculate both the traditional correlation function statistics as well as the more recent ω statistic of Xu et al. (2010) using the BOSS CMASS sample of galaxies from SDSS-III DR12; we then calculate a correlation coefficient for each statistic. Our focus is on intermediate scales, roughly $20 \lesssim r \lesssim 100$ h^{-1}Mpc, which can be compared to the results of previous analyses at smaller scales using similar statistical methods (e.g., Zehavi et al. 2005). Our

approach also provides an alternative to analyses of colour-dependent clustering using the complementary counts-in-cells method (e.g., Wild et al. 2005; Swanson et al. 2008). Throughout we assume a flat ΛCDM cosmology with $\Omega_m = 0.274$, which is consistent with Anderson et al. (2012).

4.2 Data

The SDSS-III DR12 contains spectra of over 1.3 million galaxies and *ugriz* imaging of 14555 sq. degrees of sky obtained using a 2.5 m telescope at Apache Point Observatory (York et al. 2000; Gunn et al. 2006; Alam, et al. 2015). A series of publications outlines the technical details of SDSS instrumentation (Fukugita et al. 1996; Smith et al. 2002; Doi et al. 2010; Smee et al. 2013) and the data processing pipelines (Lupton et al. 2001; Pier et al. 2003; Padmanabhan et al. 2008; Bolton et al. 2012; Weaver et al. 2015). We perform our analysis on the CMASS sample of BOSS galaxies, which is defined via colour and magnitude cuts as in Eisenstein et al. (2011), Dawson et al. (2013), and Reid et al. (2015). We further narrow our attention to the redshift range $0.55 < z < 0.65$, so selected as to avoid incompleteness of the CMASS sample at higher redshifts and to bypass lower redshifts where the CMASS colour cuts exclude blue galaxies. To divide the sample into red and blue galaxies, we use the criterion of Masters et al. (2011), which selects red galaxies using the simple colour cut $g - i > 2.35$. These cuts yield 232,759 red galaxies and 61,301 blue galaxies. In addition to the data, we select two subsamples of random points distributed across the survey area to correspond to the red and blue galaxies such that each set has roughly 50 times the number of galaxies as the data subsamples.

Since this colour cut yields roughly four times more red galaxies than blue, we use the redshift distribution of galaxies, shown in Fig. 4.1, to generate weights $w_{\rm colour}$ for the blue galaxies that match their distribution to the red galaxies, which we will use in addition to the standard data weights. The colour weights match the redshift distributions to ensure that the large-scale structure variations in the survey are equally weighted, thereby reducing sample variance in the comparison of clustering between the two samples. The final weighting that we use is then:

$$w_{\rm total} = w_{\rm colour} w_{\rm sys} (w_{zf} + w_{cp} - 1), \tag{4.8}$$

where $w_{\rm colour} = 1$ for red galaxies and $w_{\rm colour} = N_r(z)/N_b(z) > 1$ for blue galaxies, $w_{\rm sys}$ is a systematic weight that accounts for observing conditions, and w_{zf} and w_{cp} account for redshift failures and close pairs, respectively (c.f. Anderson et al. 2012; Ross et al. 2014). We additionally match the redshift distribution of the randoms to that of the data.

It is worth noting that the simple colour cut of Masters et al. (2011) is not the only choice for dividing the galaxy sample into red and blue subsets; other works have employed different cuts, such as the luminosity dependent colour cut of Zehavi et al. (2011) and Guo et al. (2013). However, for the purposes of this work, the exact choice of the colour cut is not significant, since we make the randoms trace the galaxy redshift distributions. In essence, all we require is a simple criterion by which to divide the sample into two categories, which we compare via two statistics.

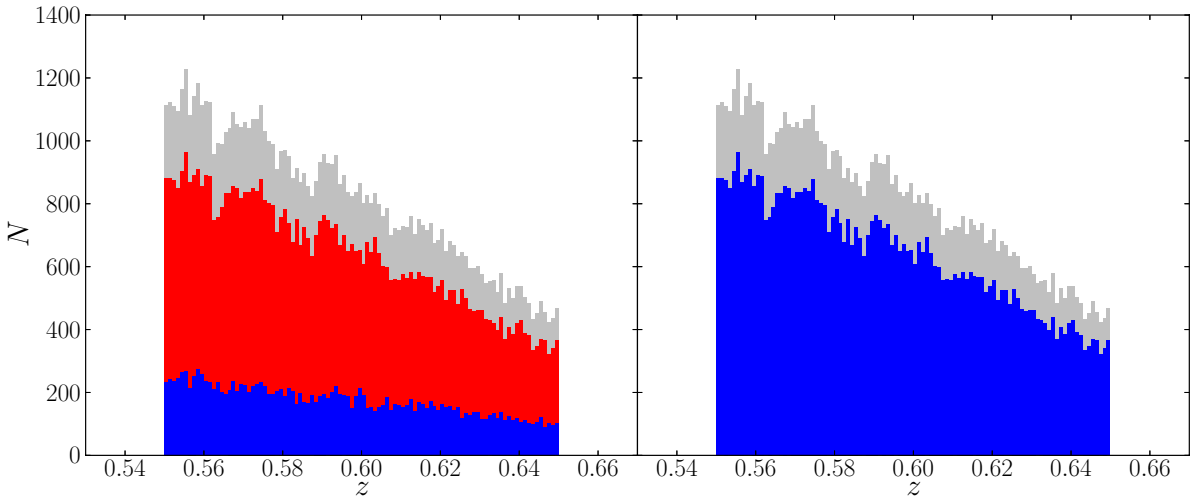

Figure 4.1.—: A histogram of the distribution of galaxies in the DR12 CMASS South sample over $0.55 < z < 0.65$. The lefthand panel shows the original division into red and blue galaxies following the simple colour cut described in Section 6.2; in the righthand panel, we show the distribution after weighting the blue sample to match the red galaxies.

4.3 Procedure

4.3.1 Statistics

One of the standard methods of calculating the galaxy correlation function is the Landy-Szalay estimator (Landy & Szalay 1993):

$$\xi(r) = \frac{DD(r) - 2DR(r) + RR(r)}{RR(r)}, \tag{4.9}$$

where the terms DD, DR, and RR denote normalised data-data, data-random, and random-random pair counts. In analyzing red and blue galaxy clustering, we may thus define the auto-correlations of blue galaxies and red galaxies as:

$$\xi_{bb}(r) = \frac{D_bD_b(r) - 2D_bR_b(r) + R_bR_b(r)}{R_bR_b(r)}, \tag{4.10}$$

$$\xi_{rr}(r) = \frac{D_rD_r(r) - 2D_rR_r(r) + R_rR_r(r)}{R_rR_r(r)}, \tag{4.11}$$

and the cross-correlation (blue-red) as:

$$\xi_{br}(r) = \frac{D_bD_r(r) - D_bR_r(r) - D_rR_b(r) + R_bR_r(r)}{R_bR_r(r)}. \tag{4.12}$$

From these functions we can then compute the cross-correlation coefficient,

$$r_\xi = \frac{\xi_{br}}{\sqrt{\xi_{rr}\xi_{bb}}}, \tag{4.13}$$

which provides a measure of the stochasticity.

However, while correlation functions provide a useful measurement of the stochasticity parameter, it is possible to extend this analysis by using a statistic that is both more computationally efficient and less susceptible to poorly constrained or

measured fluctuations from both small and large scales. Such a statistic is provided by Xu et al. (2010), who define an ω_ℓ statistic whose monopole term is:

$$\omega_0(r_s) = 4\pi \int W(r, r_s)\xi(r)r^2 dr, \tag{4.14}$$

where W is a smooth, compensated filter, chosen by Xu et al. (2010) (see also Padmanabhan et al. 2007) to be:

$$W(x) = (2x)^2(1-x)^2\left(\frac{1}{2} - x\right)\frac{1}{r_s^3}, \tag{4.15}$$

where

$$x = \left(\frac{r}{r_s}\right)^3. \tag{4.16}$$

The smoothness of the filter function W means that ω_0 is largely insensitive to small-scale power, while the fact that W integrates to zero removes the sensitivity to large-scale power and reduces the risk of including large-scale systematic errors.

Now, following Xu et al. (2010), if we define a simple pair-count estimator of the correlation function as:

$$\xi(r) = \frac{DD(r)}{RR(r)} - 1, \tag{4.17}$$

then by substituting into Equation (4.14), we obtain:

$$\omega_0(r_s) = 4\pi \int W(r, r_s)\frac{DD(r)}{RR(r)}r^2 dr, \tag{4.18}$$

with the integral of the -1 term in Equation (4.17) vanishing since we have selected a compensated filter. The DD term has a simple mathematical interpretation: DD is simply a weighted count over pairs at a given separation. That is, DD can be written as a sum of Dirac delta functions:

$$DD(r) = \sum_j \eta_j \delta_D(r - r_j), \tag{4.19}$$

where η_j is the product of the $w_{\rm tot}$ of the two galaxies in the pair. The RR term, on the other hand, is a description of the survey region, and may be written as:

$$RR(r) = N_D^2 \Phi(r) \frac{4\pi r^2 dr}{V}. \tag{4.20}$$

Here, N_D is the weighted number of (data) galaxies, and V is the total survey volume. $\Phi(r)$ is a function that takes into account the survey boundaries; that is, it measures the fraction of pairs that are lost because the central galaxy around which the pair counts are being computed is close to the boundaries. $\Phi(r)$ can be approximated by counting up RR pairs and then fitting a polynomial to the formula defined in Equation (4.20). With Φ thus calculated, rearranging this equation yields:

$$\frac{V}{N_D^2} \frac{1}{\Phi(r)} = \frac{4\pi r^2 dr}{RR(r)}. \tag{4.21}$$

Returning to Equation (4.18), we find:

$$\omega_0(r_s) = \int W(r, r_s) \sum_j \eta_j \delta_D(r - r_j) \frac{4\pi r^2}{RR(r)} dr. \tag{4.22}$$

The δ_D function then collapses the integral so that, upon substituting Equation (4.21) and absorbing η_j into W, we obtain the following summation:

$$\omega_0(r_s) = \frac{V}{N_D^2} \sum_j \frac{W(r_j, r_s)}{\Phi(r_j)}. \tag{4.23}$$

Accordingly, we see that the ω_0 statistic reduces to a discrete sum over pairs. So defined, ω_0 reveals several additional advantages over the traditional ξ statistic (Padmanabhan et al. 2007; Xu et al. 2010). First, when computing ξ, we initially bin the data to compute the pair counts at a discrete set of points. When computing ω_0, on the other hand, we sum over each pair individually, which eliminates binning concerns. Additionally, the computation of ξ is time-consuming since the number of randoms is

typically chosen to be about 50 times the number of data points; while RR still needs to be computed in order to obtain Φ, one can use far fewer points in order to simply get an estimate of the geometry of the survey.

Now, we can define ω analogues to all the correlation function statistics. The correlation functions themselves are translated into:

$$\omega_{bb}(r_s) = \frac{V}{N_b^2} \sum_{j \in D_b D_b} \frac{W(r_j, r_s)}{\Phi(r_j)}, \tag{4.24}$$

$$\omega_{rr}(r_s) = \frac{V}{N_r^2} \sum_{j \in D_r D_r} \frac{W(r_j, r_s)}{\Phi(r_j)}, \tag{4.25}$$

$$\omega_{br}(r_s) = \frac{V}{N_b N_r} \sum_{j \in D_b D_r} \frac{W(r_j, r_s)}{\Phi(r_j)}. \tag{4.26}$$

From these, we construct an ω coefficient analogous to r_ξ as:

$$r_\omega = \frac{\omega_{br}}{\sqrt{\omega_{bb}\omega_{rr}}}, \tag{4.27}$$

which will provide a measurement of the stochasticity. In order to reduce the amount of subscripts in certain contexts, we note that we will use ω and ω_0 for the Xu et al. (2010) statistic interchangeably throughout the remainder of this work. We calculate the ξ and ω statistics for three selections of random galaxies, and average the results for r for our final result.

4.3.2 Error Analysis

We employ the jackknife method of error estimation to derive error bars for our measurements of ξ and ω. In the jackknife method, we first subdivide our survey into N roughly commensurate regions, then compute the statistics N times, each time leaving out one of the previously defined regions. Then, the jackknife mean of the measurements

may be written:

$$\zeta_{J,i} = \sum_{j \neq i} \frac{\zeta_j}{N-1} = \frac{N\bar{\zeta} - \zeta_i}{N-1}. \tag{4.28}$$

From this, we may derive the errors as:

$$\sigma^2_{J,\bar{\zeta}} = \frac{N-1}{N} \sum_{i=1}^{N} (\zeta_{J,i} - \bar{\zeta})^2. \tag{4.29}$$

The remaining issue is the definition of these regions. We use the method of Voronoi tessellation, in which we select a set of N central points within the survey volume, and then for each of these points compute the locus of points that are closer to that central point than any other. In practice, we choose a random sample of 150 galaxies to serve as the central points. Then, to obtain Voronoi regions that are similar in size we iterate over this selection, splitting the largest region by selecting two new central points from within that region and merging the smallest region into its neighbors by removing its central point and recomputing the regions. Although the regions are not exactly the same size, with the smallest and largest Voronoi region differing by $\lesssim 50\%$, we have verified numerically that these modest variations do not measurably bias our result.

The result of this process is shown in Fig. 4.2, which shows the final set of Voronoi regions for one of the three runs that contributes to our final averaged value for r. Each of the final Voronoi regions spans an area of roughly $14555/150 \approx 100$ sq. degrees, or roughly 10 degrees on each side, which amounts to a transverse comoving distance of roughly 1.6 h^{-1}Gpc at $z = 0.6$, the midpoint of our redshift range. Having thus computed the Voronoi regions V_i, we obtain the jackknife regions J_i as $J_i = \sum V_n - V_i$.

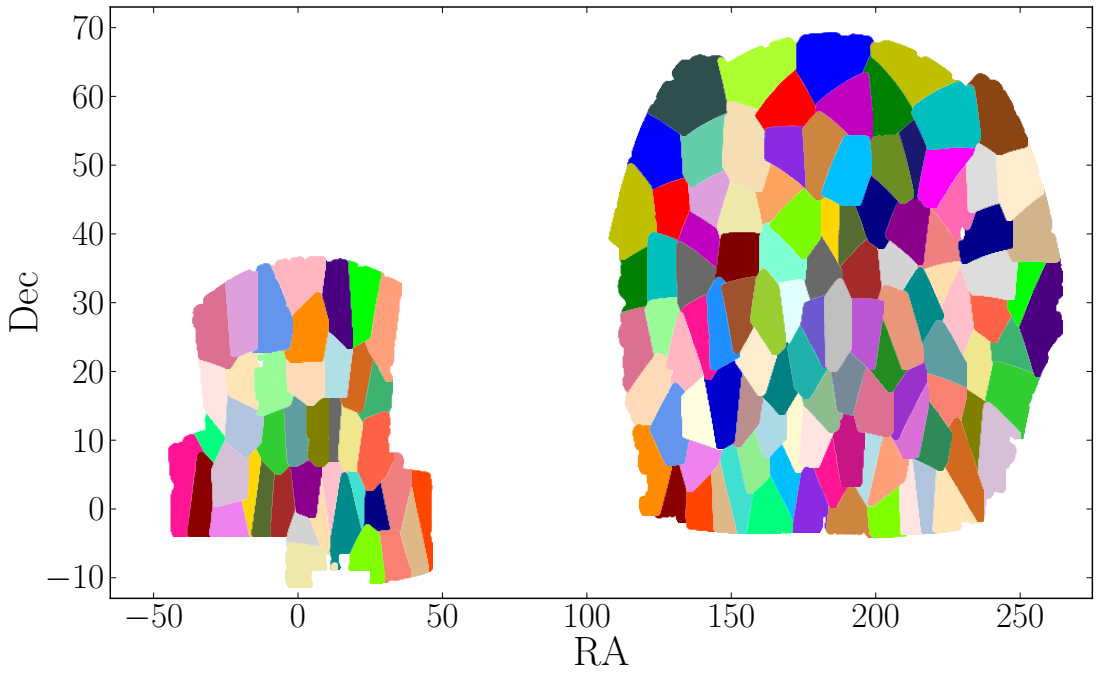

Figure 4.2.—: Definition of 150 Voronoi regions over the entire SDSS survey area that are used in the computation of jackknife errors for one run.

4.4 Results

We compute both the ξ and ω statistics for the CMASS sample of galaxies in three iterations, each with a different selection of randoms and of Voronoi regions, which allows us to test the stability of the results. For the correlation function, we choose a binning of $\Delta R = 5\ h^{-1}$Mpc, while for ω, we select 9 values of R_s for which to calculate the statistic, each spaced by 10 h^{-1}Mpc. The correlation functions — the blue and red auto-correlations, and the blue-red cross-correlation — and the corresponding ω statistics are computed in Fig. 4.3 for one of the runs.

From the three correlation functions, we obtain the correlation coefficient r_ξ, shown in the left-hand panel of Fig. 4.4 for one of the iterations, and fit to it a horizontal line. Although we compute the correlation functions themselves out to large scales, for the calculation of the correlation coefficient, we use the range $20 < R < 80\ h^{-1}$Mpc. We also fit the analogous coefficient r_ω (albeit in the slightly extended range $20 < R_s < 100\ h^{-1}$Mpc), the results of which can be seen in the righthand panel of Fig. 4.4 for one of the runs. The reduced covariance matrices used in that iteration are furnished in Fig. 4.5. It is worth noting that the ξ covariance matrix is highly diagonal; this is likely due to shot noise in the blue subsample of galaxies. The ω covariance matrix, on the other hand, does demonstrate some covariance due to integrating ξ over overlapping kernels.

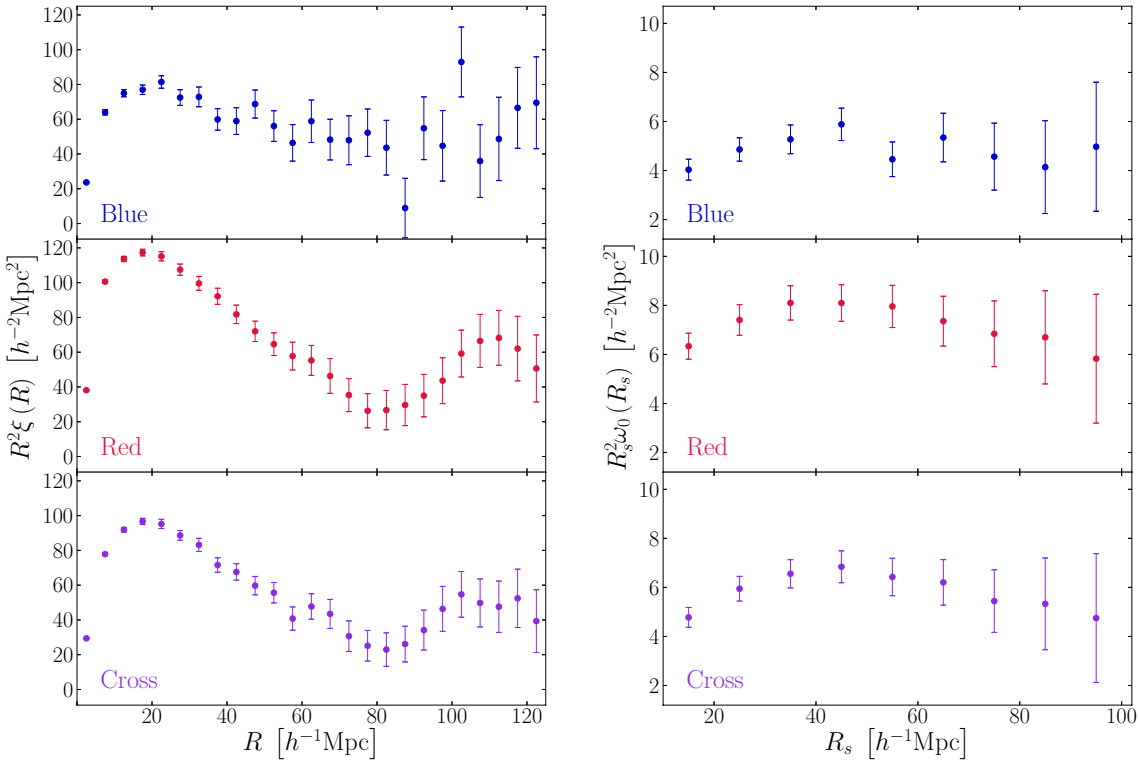

Figure 4.3.—: Left: Blue-blue (top), red-red (middle), and blue-red (bottom) correlation functions, computed using a bin size of 5 h^{-1} Mpc and scaled by R^2. Right: Blue-blue, red-red, and blue-red ω_0 functions, computed using an R_s spacing of 10 h^{-1} Mpc and scaled by R_s^2.

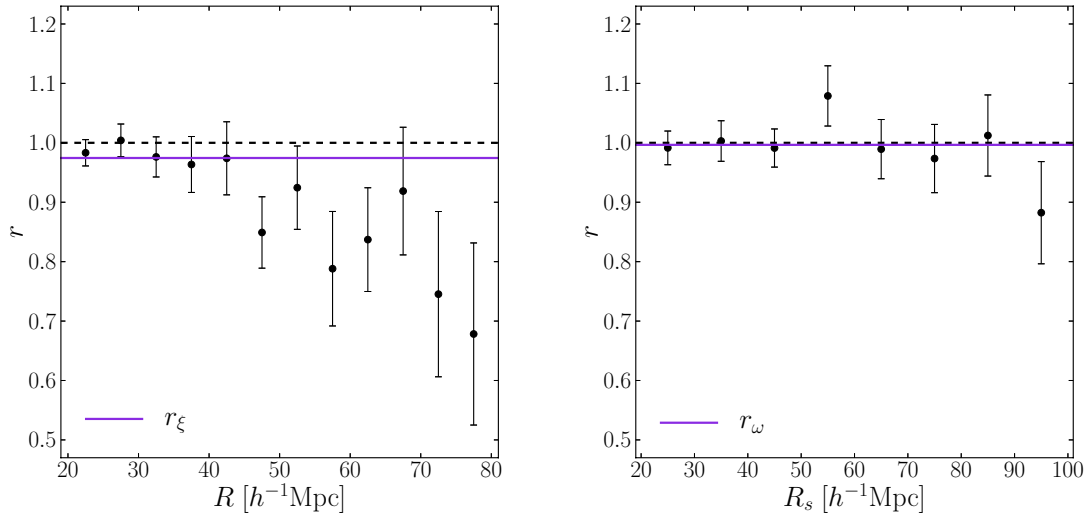

Figure 4.4.—: The correlation coefficient, r_ξ (left) and the analogous coefficient r_ω (right) given by the best fit line (solid) from one run. A dashed line is drawn at $r = 1$ for comparison. Our results using the ω statistic indicate less stochasticity on intermediate scales than the noisier analysis using correlation functions.

We average the stochasticity parameters r that we measure this way from the three iterations; the resulting values are:

$$\langle r_\xi \rangle = 0.978 \pm 0.014, \tag{4.30}$$

$$\langle r_\omega \rangle = 0.996 \pm 0.011. \tag{4.31}$$

Although r_ξ is lower than r_ω, the results of both suggest low stochasticity on intermediate scales. The difference in these values is possibly influenced by the substantial scatter for $R \gtrsim 45\ h^{-1}$Mpc in r_ξ, to which the ω statistic is less susceptible.

However, our results averaging over scales are driven primarily by the smaller scale values, as these are better measured in ξ and ω. Accordingly, we test our results by

varying the minimum radius and refitting r_ξ and r_ω for the same run as depicted in Fig. 4.4. The resulting values of r_ξ and r_ω are plotted as a function of $R_{\rm min}$ in Fig. 4.6. From this, we see that r_ξ has a much stronger dependence on the minimum radius of the fit than r_ω, and shows a steep decline as $R_{\rm min}$ increases, which may be due to a systematic at large scales, while r_ω remains roughly constant. This suggests that ω, which demonstrates less variation, is a promising statistic for this type of analysis.

For both statistics, using a minimum fitting radius that is $< 20\ h^{-1}$Mpc shows results that deviate from what would be obtained using a slightly larger minimum radius. For ξ, r_ξ is larger, while for ω, r_ω is smaller when $R_{\rm min} < 20\ h^{-1}$Mpc. Accordingly, to avoid results that are driven by these small scales, we recommend using a fitting range $R \gtrsim 20\ h^{-1}$Mpc, and the results that we quote use that range.

4.5 Discussion

Our results align well with previous studies using correlation function analyses, although given the various data sets and definitions of colour cuts employed in these works, the exact values cannot directly compared; rather we simply note the consistency of the results among similar analyses. With data from SDSS DR7, Zehavi et al. (2011) found that r_ξ is consistent with 1 on the largest of scales that they consider (roughly $10 < R < 40\ h^{-1}$Mpc). This agrees with the results of Wang et al. (2007), whose analysis of SDSS DR4 established similar results for $R \sim 10\ h^{-1}$Mpc. Our measured value of r_ω aligns well with these results.

A complementary approach was pursued by Wild et al. (2005) and Swanson et al.

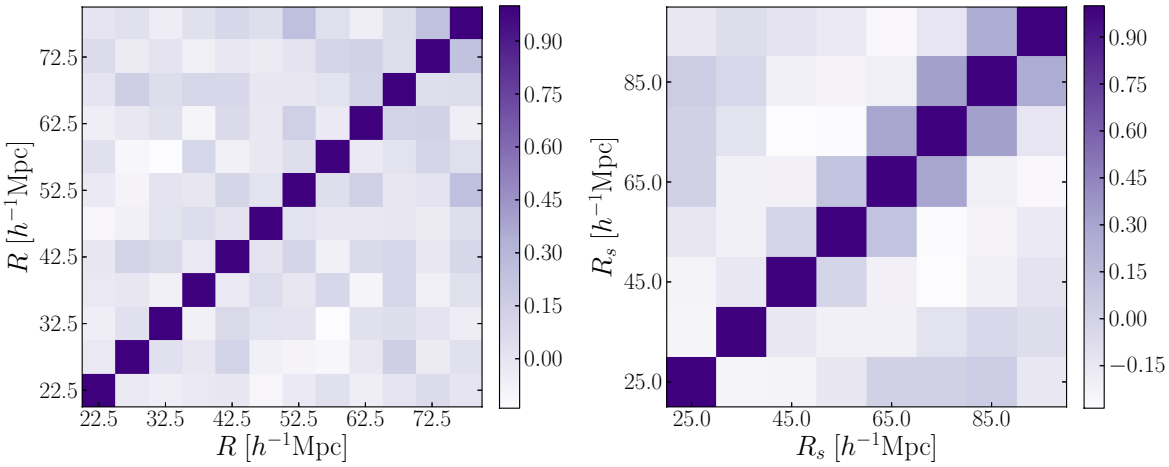

Figure 4.5.—: The reduced covariance matrices for the correlation coefficient, r_ξ (left), and the analogous coefficient, r_ω (right), calculated for $R < 80\ h^{-1}$Mpc and $R_s < 100\ h^{-1}$Mpc from the run whose results are shown in Fig. 4.4. These matrices are used to calculate the χ^2 for fitting r.

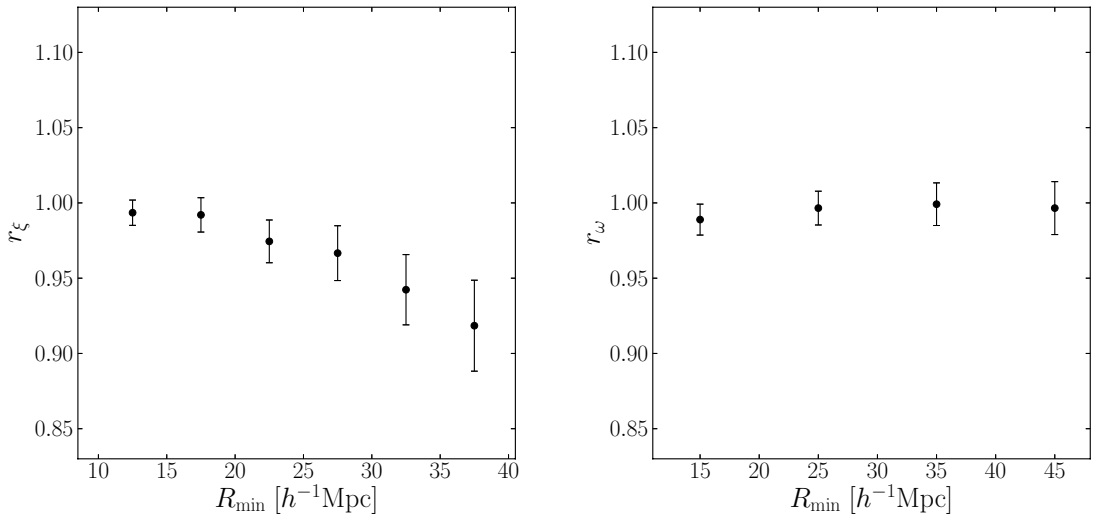

Figure 4.6.—: The fitted values of r_ξ and r_ω as a function of $R_{\rm min}$, the minimum radius used in the fit, for one run. The results using the ξ statistic are more strongly dependent on the fitting range than those using ω.

(2008) in the form of the counts-in-cells method. Wild et al. (2005) used data from the 2dF Galaxy Redshift Survey to investigate r_ξ on scales of $7 < R < 32\ h^{-1}$Mpc. Their value of r_ξ increases from roughly $r_\xi \approx 0.87$ at $R = 7\ h^{-1}$Mpc to $r_\xi = 0.97$ at $R \approx 30\ h^{-1}$Mpc. Swanson et al. (2008) relied on SDSS DR5 to obtain similar values for $R \gtrsim 25\ h^{-1}$Mpc, concluding that $r_\xi \approx 0.97$ as well on such large scales. These results are in good agreement with our values for r_ξ, but are somewhat lower than what we measure for r_ω. Additionally, Blanton (2000) used this method to find that $r_\xi \sim 0.87 - 0.95$ for samples of early and late-type galaxies in the Las Campanas Redshift Survey on $15\ h^{-1}$Mpc scales, which is consistent with our lower bound from the ξ statistic.

It is worth noting that in these works as well as our own the correlation coefficient is compared to $r_\xi = 1$ to determine the level of stochasticity, but in a few bins, our values of r_ξ exceed 1. To examine why this is so, we recall the Dekel & Lahav (1999) formalism of Equation (4.7), which describes the red and blue galaxy distributions as:

$$\frac{\vec{\delta_r}}{b_r} = \vec{\delta} + \vec{\epsilon_r} \equiv \vec{\alpha}, \tag{4.32}$$

$$\frac{\vec{\delta_b}}{b_b} = \vec{\delta} + \vec{\epsilon_b} \equiv \vec{\alpha} + \vec{\beta}. \tag{4.33}$$

Defining a correlation matrix M, we may then compute the correlation coefficient as:

$$r_\xi^2 = \frac{\langle \vec{\alpha}^T M(\vec{\alpha} + \vec{\beta})\rangle^2}{\langle \vec{\alpha}^T M\vec{\alpha}\rangle\langle(\vec{\alpha} + \vec{\beta})^T M(\vec{\alpha} + \vec{\beta})\rangle}, \tag{4.34}$$

$$r_\xi^2 = \frac{\langle \vec{\alpha}^T M\vec{\alpha}\rangle^2}{\langle \vec{\alpha}^T M\vec{\alpha}\rangle\left[\langle \vec{\alpha}^T M\vec{\alpha}\rangle + \langle \vec{\beta}^T M\vec{\beta}\rangle\right]}, \tag{4.35}$$

where the cross terms have gone to zero upon taking the expectation value. This means that:

$$r_\xi = \sqrt{\frac{\langle \vec{\alpha}^T M\vec{\alpha}\rangle}{\langle \vec{\alpha}^T M\vec{\alpha}\rangle + \langle \vec{\beta}^T M\vec{\beta}\rangle}} \equiv \sqrt{\frac{\xi_\alpha}{\xi_\alpha + \xi_\beta}}. \tag{4.36}$$

Accordingly, we have expressed r_ξ in terms of the autocorrelation function of $\vec{\beta} = \vec{\epsilon_b} - \vec{\epsilon_r}$. If $\xi_\beta = 0$, then $r_\xi = 1$, as expected. However, if $\xi_\beta > 0$, then $r_\xi < 1$, but if ξ_β is negative, then r_ξ will in fact exceed 1. We note that our definition of stochasticity relies on the correlation function so it does not rule out local stochasticity that is uncorrelated at large separations.

4.6 Comparison with Simulations

To provide some context for our results, we apply these methods to a catalog produced from a cosmological N-body simulation run with the Abacus code (Ferrer et al. in prep; Metchnik & Pinto in prep.), which used 4096^3 particles in a 3.5 h^{-1}Gpc box, yielding particle masses of 5×10^{10} $h^{-1}\mathrm{M}_\odot$ with a Plummer softening of 105 h^{-1}kpc. Halos at a given redshift were found by the friends-of-friends algorithm (Davis et al. 1985) with a linking length parameter $b = 0.2$. We select a full-sky survey of halos, over which we define 145 Voronoi regions, in an annulus corresponding to the range $0.55 < z < 0.65$. We extract the real-space centre-of-mass positions of halos that fall into one of two well-separated mass bins, $(0.5 - 1.0) \times 10^{13}$ $h^{-1}\mathrm{M}_\odot$ and $(0.5 - 1.0) \times 10^{14}$ $h^{-1}\mathrm{M}_\odot$. These mass ranges do not correspond to the masses of the CMASS galaxies; rather, the lower mass bin is selected so as to have at least 100 particles in the halo, while the other is chosen to be significantly more massive. This split yields 2,183,762 low mass and 113,740 high mass halos.

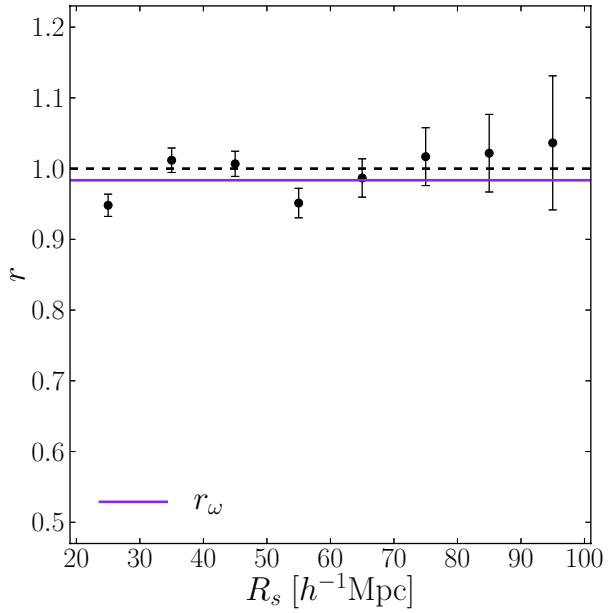

Figure 4.7.—: The coefficient r_ω for the simulated catalog from the best fit line (solid) shown. A dashed line is drawn at $r = 1$ for comparison.

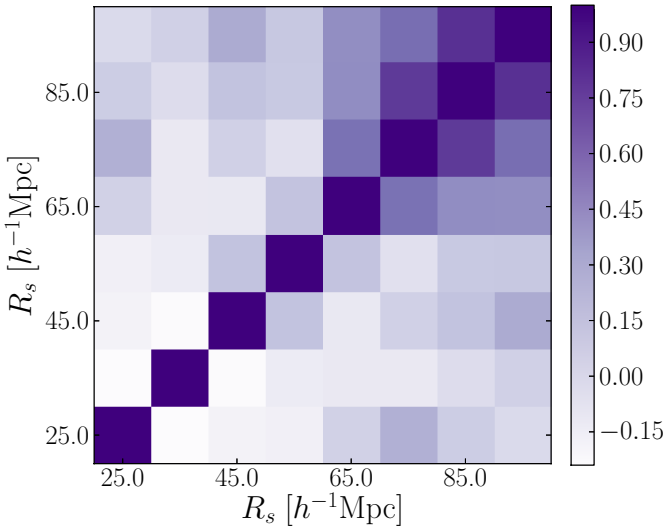

Figure 4.8.—: The reduced covariance matrix for the correlation coefficient coefficient, r_ω, measured from the simulated catalogs, which is used for calculating the χ^2 for the fit shown in Fig. 4.7.

We then follow the same procedure as outlined in Section 4.3 to measure the coefficient r_ω, although we only use one run for the simulated catalog, and only 10× randoms. Fig. 4.7 shows the variation of r_ω as a function of R_s, as well as the best fit horizontal line to the points, and Fig. 4.8 shows the reduced covariance matrix used for the fitting. We find a best fit value of $r_\omega = 0.984 \pm 0.006$. This measured value is slightly lower than what we found in the data using this same statistic, although the ranges of values are consistent with each other, and with the value of r_ξ that was calculated for DR12. However, as noted above, the samples that we use here are not directly comparable to the red/blue split used in the data as these halos are more massive than the CMASS galaxies. Instead, what the simulation results indicate is that a halo model does involve some stochasticity, and provide a lower bound on r, which would likely be

higher for halo masses more closely attuned to CMASS.

4.7 Summary and Conclusions

Using the CMASS sample of galaxies from SDSS DR12, we have measured the clustering of red and blue galaxies using correlation functions and the ω_0 statistic of Xu et al. (2010). From these functions, we constructed the stochasticity parameter r and analysed its value over intermediate scales, which we take as roughly $20 \lesssim R \lesssim 100\ h^{-1}$Mpc. Basing our results primarily on the ω statistic, we found that $r > 0.974$, indicating low levels of stochasticity on these scales. Taking into account the results using the standard correlation function statistics, this bound decreases slightly to about $r > 0.95$.

Our results are in good agreement with the results of previous correlation function studies, including those of Wang et al. (2007) and Zehavi et al. (2011). We also compared these values to the value of r_ω obtained from a simulated halo catalog. We found that the simulated catalog prefers a slightly lower value of r_ω than does the data; nevertheless, the values are consistent with each other as well as with the results of using the ξ statistic on the data. However, due to the high mass ranges of the simulated halos, the value of r from this simulation may be lower than what we would obtain from halos with masses more closely corresponding to those of CMASS galaxies.

We have additionally established the utility of the ω_0 statistic in analyzing the stochasticity. As the results of Section 4.4 indicate, the traditional correlation function statistics yield noisy estimates of r on large scales. In addition to being more

computationally efficient, the ω_0 statistic is less susceptible to these fluctuations, making it a promising tool for future investigations, possibly at larger scales.

4.8 Acknowledgments

We would like to thank Ashley Ross, Uros Seljak, Michael Strauss, and Idit Zehavi for helpful comments and discussions. We are also grateful to Douglas Ferrer, who produced the Abacus catalog that was used in this paper.

This work was supported by the National Science Foundation Graduate Research Fellowship under Grant No. DGE-1144152 and by U.S. Department of Energy Grant No. DE-SC0013718. The analysis in this paper made use of tools from NumPy (van der Walt, Colbert, & Varoquaux 2011), SciPy (Oliphant 2007), and Matplotlib (Hunter 2007), as well as from ROOT (Brun & Rademakers 1997; see also http://root.cern.ch/).

This paper relies on data from SDSS-III. Funding for SDSS-III has been provided by the Alfred P. Sloan Foundation, the Participating Institutions, the National Science Foundation, and the U.S. Department of Energy Office of Science. The SDSS-III web site is http://www.sdss3.org/.

SDSS-III is managed by the Astrophysical Research Consortium for the Participating Institutions of the SDSS-III Collaboration including the University of Arizona, the Brazilian Participation Group, Brookhaven National Laboratory, Carnegie Mellon University, University of Florida, the French Participation Group, the German Participation Group, Harvard University, the Instituto de Astrofisica de Canarias, the Michigan State/Notre Dame/JINA Participation Group, Johns Hopkins University,

Lawrence Berkeley National Laboratory, Max Planck Institute for Astrophysics, Max Planck Institute for Extraterrestrial Physics, New Mexico State University, New York University, Ohio State University, Pennsylvania State University, University of Portsmouth, Princeton University, the Spanish Participation Group, University of Tokyo, University of Utah, Vanderbilt University, University of Virginia, University of Washington, and Yale University.

Chapter 5

Analyzing Baryon Acoustic Oscillations in Sparse Spectroscopic Surveys via Cross-Correlations

Anna Patej & Daniel Eisenstein, to be submitted to *Monthly Notices of the Royal Astronomical Society* (2016)

5.1 Introduction

The signature of baryon acoustic oscillations is a peak in the clustering of galaxies at large scales that is a relic of propagating sound waves in the early universe and whose location depends on the distance the waves were able to cover prior to recombination (for a recent review, see Weinberg et al. 2013). Major redshift surveys like the Sloan Digital Sky Survey's (SDSS) Baryon Oscillation Spectroscopic Survey (BOSS; Dawson et al.

2013) and the 2dF Galaxy Redshift Survey (2dFGRS; Colless et al. 2001) have analyzed the clustering of galaxies in order to detect this feature and use it to measure the cosmological quantities $D_A(z)$, the angular diameter distance, and $H(z)$, the Hubble parameter (Eisenstein et al. 2005; Cole et al. 2005). BOSS has already attained percent level precision distance measurements using the BAO method at $z = 0.57$ (Anderson et al. 2014).

However, most detections of the BAO feature in samples of galaxies thus far have occurred at fairly low redshifts, where these galaxy redshift surveys are able to attain sufficiently high densities of spectroscopically observed galaxies. However, present and future surveys such as eBOSS (Dawson et al. 2016) and the Dark Energy Spectroscopic Instrument (DESI) (Levi et al. 2013) will push the availability of spectra at higher redshifts by targeting quasars in addition to lower redshift galaxies. The densities of these objects are, nevertheless, expected to be lower than what is needed for measuring the BAO in the standard ways with auto-correlations. Accordingly, new methods need to be developed for leveraging such sparse datasets.

To this end, in this paper we develop a new method for measuring the BAO signal with sparse spectroscopic data. Our method consists of cross-correlating the sparse data with a dense photometric sample to enhance the signal. We present this method, deriving explicit forms for the correlation function and the covariance matrix. We then apply it to data from SDSS to verify whether we can detect the BAO peak. In what follows, we use a flat ΛCDM cosmology with $\Omega_m = 0.314$ and $h = 0.673$, consistent with *Planck* 2015 parameters (Ade et al. 2015).

5.2 Data

As in Chapter 4, we use the color cut-defined CMASS sample of galaxies from Data Release 12 of SDSS-III (Eisenstein et al. 2011; Dawson et al. 2013; Alam, et al. 2015; Reid et al. 2015) for our spectroscopic sample. These data were obtained with a 2.5 m telescope at Apache Point Observatory (York et al. 2000; Gunn et al. 2006) whose instrumentation is well-documented (Fukugita et al. 1996; Smith et al. 2002; Doi et al. 2010; Smee et al. 2013) and for which a set of data processing pipelines has been developed (Lupton et al. 2001; Pier et al. 2003; Padmanabhan et al. 2008; Bolton et al. 2012; Weaver et al. 2015). To obtain a sufficiently sparse sample of spectra for the validation of the method that we will describe in the next section, we restrict the redshift range, focusing only on those galaxies for which $z > 0.6$. This yields 205,367 galaxies, and we select a set of random points five times larger than this for the construction of the correlation function. The photometric sample used in this paper comes from SDSS DR9 (Ahn et al. 2012) and comprises 6,594,677 galaxies; we use a catalog of randoms two times larger than this to construct the correlation function.

5.3 Method

For a spectroscopic survey of galaxy density n_s, the variance on each Fourier mode is $\sigma_s^2 = (P_s + 1/n_s)^2$, so that the signal to noise (S/N) is given by (Weinberg et al. 2013):

$$\frac{S}{N} = \frac{n_s P_s}{1 + n_s P_s}, \tag{5.1}$$

where P_s denotes the power spectrum $P_s(k)$. From this, we immediately see that the S/N per mode approaches 1 when $n_s P_s \gg 1$ but decreases when $n_s P_s < 1$, so that the relevant quantity to track is nP. Let us assume we have a photometric dataset with some n_p and P_p. Both the spectroscopic and photometric samples are biased tracers of the underlying matter distribution such that:

$$\delta_s(\boldsymbol{x}) = b_s \delta(\boldsymbol{x}),\ \delta_p(\boldsymbol{x}) = b_p \delta(\boldsymbol{x})$$

Accordingly, we may write the power spectra as $P_s(k) = b_s^2 P(k)$ and $P_p(k) = b_p^2 (n_p/N_p) P(k)$, with the factor of $n_p/N_p = 1/L_p$, where L_p is the depth of the photometry, approximately accounting for the fact that we are converting the three-dimensional $P(k)$ to the two-dimensional $P_p(k)$.

When we cross-correlate a photometric sample to the spectroscopic sample, we obtain the power spectrum of the cross-correlation as $P_x = (n_p/N_p) b_s b_p P$ with variance $\sigma_x^2 = P_x^2 + \sigma_{s,2}\sigma_{p,2}$, where the subscript "2" indicates projection, so that the signal-to-noise becomes:

$$\left(\frac{S}{N}\right)^2 = \frac{P_x^2}{P_x^2 + (b_s^2[n_s/N_s]P_s + 1/N_s)(b_p^2[n_p/N_p]P_p + 1/N_p)}, \tag{5.2}$$

$$\left(\frac{S}{N}\right)^2 = \left(1 + \frac{n_s}{N_s}\frac{N_p}{n_p}\left[1 + \frac{1}{n_s b_s^2 P}\right]\left[1 + \frac{1}{n_p b_p^2 P}\right]\right)^{-1}, \tag{5.3}$$

$$\left(\frac{S}{N}\right)^2 = \left(1 + \frac{L_p}{L_s}\left[1 + \frac{1}{n_s b_s^2 P}\right]\left[1 + \frac{1}{n_p b_p^2 P}\right]\right)^{-1}. \tag{5.4}$$

Accordingly, we see that with the cross-correlation, when $n_s P_s$ gets small, we can compensate with the $n_p P_p$ term.

To see when this method would improve upon the results of using the auto-correlation, let us estimate the number of modes that we could measure. For a spectroscopic sample with constant density, the effective number of modes $\mathcal{N}_s$ in a shell

of width Δk is given by:

$$\mathcal{N}_s = \frac{AL_s}{2(2\pi)^3} 4\pi k^2 \Delta k \times \left(\frac{n_s P_s}{1 + n_s P_s}\right)^2. \tag{5.5}$$

In the case of the photometric sample, we have $k_z = 0$, which means that

$$\mathcal{N}_p = \frac{A}{(2\pi)^2} 2\pi k \Delta k \times \left(1 + \frac{L_p}{L_s}\left[1 + \frac{1}{n_s b_s^2 P}\right]\left[1 + \frac{1}{n_p b_p^2 P}\right]\right)^{-1}. \tag{5.6}$$

We are looking for the case wherein $\mathcal{R} = \mathcal{N}_s/\mathcal{N}_p < 1$, which means that

$$\mathcal{R} = \frac{kL_s}{2\pi}\left(\frac{1}{1 + 1/(n_s b_s^2 P)}\right)^2 \times \left(1 + \frac{L_p}{L_s}\left[1 + \frac{1}{n_s b_s^2 P}\right]\left[1 + \frac{1}{n_p b_p^2 P}\right]\right), \tag{5.7}$$

and if we assume that $n_s b_s^2 P \ll 1$ (the limit in which the auto-correlation method begins to lose information), this simplifies to:

$$\mathcal{R} = \frac{kL_s}{2\pi}\left(n_s b_s^2 P\right)^2 \times \left(\frac{L_p}{L_s}\left[n_s b_s^2 P\right]^{-1}\left[1 + \frac{1}{n_p b_p^2 P}\right]\right), \tag{5.8}$$

$$\mathcal{R} = \frac{kL_p}{2\pi}\left(\frac{1 + 1/(n_p b_p^2 P)}{1/(n_s b_s^2 P)}\right). \tag{5.9}$$

Let us denote $\eta_s = n_s b_s^2 P$ and $\eta_p = n_p b_p^2 P$, so that:

$$\mathcal{R} = \frac{kL_p}{2\pi}\frac{1 + \eta_p^{-1}}{\eta_s^{-1}}. \tag{5.10}$$

To satisfy $\mathcal{R} < 1$, we require

$$\eta_s^{-1} > \frac{kL_p}{2\pi}\left(1 + \eta_p^{-1}\right). \tag{5.11}$$

We can generally get very high photometric densities, so that we can take $\eta_p^{-1} \to 0$. Accordingly, for a reasonable photometric depth of $L_p = 500\ h^{-1}\mathrm{Mpc}$ and $k = 0.15\ h\mathrm{Mpc}^{-1}$, we require $\eta_s \lesssim 0.08$.

In practice, the *projected* cross-correlation function between the spectroscopic and photometric samples can be constructed via the Landy-Szalay estimator (Landy &

Szalay 1993),

$$w(r) = \frac{D_s D_p(r) - D_s R_p(r) - D_p R_s(r) + R_s R_p(r)}{R_s(r) R_p(r)}, \tag{5.12}$$

where D indicates the data and R denotes the random points; p and s refer to the photometry and spectroscopy, respectively. While the Landy-Szalay estimator is normally defined as providing an estimate of $\xi(r)$, the full three-dimensional correlation function, in our case we only know the positions of the galaxies on the sky for the photometric sample. Accordingly, when we compute the correlation function, we used only spectroscopic galaxies as our central points and then calculate pair counts in two-dimensional annular bins around the central galaxy, assuming that the photometric galaxies in the bin are at the same redshift as the spectroscopic galaxy to convert angular separations into physical distances. Thus, the resulting correlation function is by construction the projected correlation function $w(r)$, which has the benefit of not requiring redshift-space corrections.

To compute errors on our measurements, we divide the spectroscopic survey area into 150 roughly commensurate regions using Voronoi tessellation and then employ the jackknife method. In the next section, we treat the problem more formally, deriving explicit forms not only for the projected correlation function but also the covariance matrix, which can be calculated numerically and used in fitting the theoretical forms to the data.

5.4 Derivation

Let us assume that we have two samples of galaxies: a spectroscopic sample with fractional overdensity field $\delta_s(\boldsymbol{r})$, and the other a photometric sample. For this latter sample, we can calculate a projected overdensity field as:

$$\Delta_p(\boldsymbol{\theta}) = \frac{\int dr'\, r'^2 n_p(r')\delta_p(\boldsymbol{r'})}{\int dr'\, r'^2 n_p(r')}. \tag{5.13}$$

Defining the normalization factor as

$$\mathcal{N} \equiv \int dr'\, r'^2 n_p(r'), \tag{5.14}$$

this may be written simply as

$$\Delta_p(\boldsymbol{\theta}) = \frac{1}{\mathcal{N}} \int dr'\, r'^2 n_p(r')\delta_p(\boldsymbol{r'}). \tag{5.15}$$

The correlation of δ_s and Δ_p, noting that $\boldsymbol{r} = (r, \boldsymbol{\theta})$, is then

$$w(\boldsymbol{R}) = \langle \delta_s(\boldsymbol{r})\Delta_p(\boldsymbol{\theta} + \boldsymbol{R}/r)\rangle, \tag{5.16}$$

$$w(\boldsymbol{R}) = \frac{\int d^3r\; \delta_s(\boldsymbol{r}) n_s(r)\mathcal{W}(r,\eta) \int d^2\theta'\; \Delta_p(\boldsymbol{\theta'})\mathcal{N}\mathcal{S}(\boldsymbol{\theta}, \boldsymbol{\theta'}, \boldsymbol{R}, r)}{\int d^3r\; n_s(r)\mathcal{W}(r,\eta) \int d^2\theta'\; \mathcal{N}\mathcal{S}(\boldsymbol{\theta}, \boldsymbol{\theta'}, \boldsymbol{R}, r)}. \tag{5.17}$$

Here, $\mathcal{W}$ is a weighting function that may depend on r and other variables independent of $\boldsymbol{r}$, collectively referred to as η, and $\mathcal{S}$ is a selection function that depends on the angular coordinates of the galaxies. If we focus on a single separation, then the selection function is a Dirac delta function:

$$\mathcal{S}(\boldsymbol{\theta}, \boldsymbol{\theta'}, \boldsymbol{R}, r) = \delta_D^{(2)}\left(r\boldsymbol{\theta'} - (r\boldsymbol{\theta} + \boldsymbol{R})\right). \tag{5.18}$$

Using Equations 5.15 and 5.18 and writing out explicitly $\boldsymbol{r} = (r, \boldsymbol{\theta})$, Equation 5.17

becomes:

$$w(\boldsymbol{R}) = \frac{\int dr\, r^2 n_s(r)\mathcal{W}(r,\eta)\int d^2\theta\, \delta_s(r,\boldsymbol{\theta})\int d^2\theta'\, \delta_D^{(2)}(r\boldsymbol{\theta}'-(r\boldsymbol{\theta}+\boldsymbol{R}))\int dr'\, r'^2 n_p(r')\delta_p(r',\boldsymbol{\theta}')}{\int dr\, r^2 n_s(r)\mathcal{W}(r,\eta)\int d^2\theta\ \int d^2\theta'\, \delta_D^{(2)}(r\boldsymbol{\theta}'-(r\boldsymbol{\theta}+\boldsymbol{R}))\int dr'\, r'^2 n_p(r')}. \tag{5.19}$$

The delta function collapses the θ' integral in both the numerator and denominator, giving $1/r^2$, and in the denominator, the θ integral can be immediately evaluated to a constant, yielding:

$$w(\boldsymbol{R}) = \frac{\int dr\, n_s(r)\mathcal{W}(r,\eta)\int d^2\theta\, \delta_s(r,\boldsymbol{\theta})\int dr'\, n_p(r')\delta_p(r',\boldsymbol{\theta}+\boldsymbol{R}/r)}{4\pi\int dr\, n_s(r)\mathcal{W}(r,\eta)\int dr'\, r'^2 n_p(r')}. \tag{5.20}$$

Rearranging the order of integration gives:

$$w(\boldsymbol{R}) = \frac{\int dr\, n_s(r)\mathcal{W}(r,\eta)\int dr'\, r'^2 n_p(r')\int d^2\theta\, \delta_s(r,\boldsymbol{\theta})\delta_p(r',\boldsymbol{\theta}+\boldsymbol{R}/r)}{4\pi\int dr\, n_s(r)\mathcal{W}(r,\eta)\int dr'\, r'^2 n_p(r')}. \tag{5.21}$$

With an eye towards an application to catalog data, we note that the correlation function is constructed from pair counts of galaxies, normalized by pair counts of random galaxies, so that:

$$w(\boldsymbol{R}) = \frac{N_s N_p}{R_s R_p} = \frac{(D_s - R_s)(D_p - R_p)}{R_s R_p}. \tag{5.22}$$

This allows us to identify the numerator and denominator of Equation 5.21 with $N_s N_p$ and $R_s R_p$.

5.4.1 Expectation Value

Taking the expectation value of Equation 5.21 yields:

$$\langle w(\boldsymbol{R})\rangle = \frac{\int dr\, n_s(r)\mathcal{W}(r,\eta)\int dr'\, r'^2 n_p(r')\int d^2\theta\, \langle\delta_s(r,\boldsymbol{\theta})\delta_p(r',\boldsymbol{\theta}+\boldsymbol{R}/r)\rangle}{4\pi\int dr\, n_s(r)\mathcal{W}(r,\eta)\int dr'\, r'^2 n_p(r')}. \tag{5.23}$$

Focusing on the numerator,

$$\langle N_s N_p \rangle = \int dr\, n_s(r) \mathcal{W}(r,\eta) \int dr'\, r'^2 n_p(r') \int d^2\theta\, \langle \delta_s(r,\boldsymbol{\theta}) \delta_p(r', \boldsymbol{\theta} + \boldsymbol{R}/r) \rangle, \tag{5.24}$$

we can use the Fourier transform,

$$\delta(\boldsymbol{r}) = \frac{1}{(2\pi)^{3/2}} \int d^3k\, \delta_{\boldsymbol{k}} e^{i\boldsymbol{k}\cdot\boldsymbol{r}}, \tag{5.25}$$

as well as the formalism of Dekel & Lahav (1999), which relates the $\delta_g = \delta_s, \delta_p$ fields to the underlying matter density field $\delta \equiv \delta_m$ as:

$$\delta_g = b_g \delta + \epsilon_g, \tag{5.26}$$

to write the expectation value of two δs as:

$$\langle \delta(r,\boldsymbol{\theta}) \delta(r', \boldsymbol{\theta} + \boldsymbol{R}/r) \rangle = \frac{b_s b_p}{(2\pi)^3} \int\int d^3k d^3k'\, \langle \delta_{\boldsymbol{k}} \delta_{\boldsymbol{k}'} \rangle e^{ir\boldsymbol{k}_\perp \cdot \boldsymbol{\theta}} e^{ir k_{\shortparallel}} e^{ir'\boldsymbol{k}'_\perp \cdot (\boldsymbol{\theta} + \boldsymbol{R}/r)} e^{ir' k'_{\shortparallel}}, \tag{5.27}$$

where we are using the flat sky approximation and have written $k = \sqrt{k_\perp^2 + k_{\shortparallel}^2}$, with $k_\perp$ indicating the transverse components of k and $k_{\shortparallel}$ indicating the line-of-sight component. Then, using

$$\langle \delta_{\boldsymbol{k}} \delta_{\boldsymbol{k}'} \rangle = \delta_D^{(3)}(\boldsymbol{k} + \boldsymbol{k}') P(k), \tag{5.28}$$

and integrating over k yields

$$\langle \delta(r,\boldsymbol{\theta}) \delta(r', \boldsymbol{\theta} + \boldsymbol{R}/r) \rangle = \frac{b_s b_p}{(2\pi)^3} \int d^3k'\, P(k') e^{-ir\boldsymbol{k}'_\perp \cdot \boldsymbol{\theta}} e^{-ir k_{\shortparallel}} e^{ir'\boldsymbol{k}'_\perp \cdot (\boldsymbol{\theta} + \boldsymbol{R}/r)} e^{ir' k'_{\shortparallel}}, \tag{5.29}$$

$$= \frac{b_s b_p}{(2\pi)^3} \int d^3k'\, P(k') e^{-ir\boldsymbol{k}'_\perp \cdot \boldsymbol{\theta}} e^{ir'\boldsymbol{k}'_\perp \cdot (\boldsymbol{\theta} + \boldsymbol{R}/r)} e^{-i(r-r')k'_{\shortparallel}}. \tag{5.30}$$

Thus,

$$\begin{aligned} \langle N_s N_p \rangle = \; & b_s b_p \int dr\, n_s(r) \mathcal{W}(r,\eta) \int dr'\, r'^2 n_p(r') \int \frac{d^2\theta}{(2\pi)^3} \\ & \times \int d^3k'\, P(k') e^{-ir\boldsymbol{k}'_\perp \cdot \boldsymbol{\theta}} e^{ir'\boldsymbol{k}'_\perp \cdot (\boldsymbol{\theta} + \boldsymbol{R}/r)} e^{-i(r-r')k'_{\shortparallel}}, \end{aligned} \tag{5.31}$$

If we assume that the line of sight weighting is much larger than the BAO scale, then we may approximate $k = \sqrt{k_\perp^2 + k_\parallel^2} \approx k_\perp$, and we can split up the last integral:

$$\begin{aligned}
\langle N_s N_p \rangle &= b_s b_p \int dr\, n_s(r) \mathcal{W}(r,\eta) \int dr'\, r'^2 n_p(r') \int \frac{d^2\theta}{(2\pi)^3} \\
&\quad \times \int d^2k'_\perp\, P(k'_\perp) e^{-ir\boldsymbol{k}'_\perp \cdot \boldsymbol{\theta}} e^{ir'\boldsymbol{k}'_\perp \cdot (\boldsymbol{\theta} + \boldsymbol{R}/r)} \int dk'_\parallel\, e^{-i(r-r')k'_\parallel}, \qquad (5.32) \\
&= b_s b_p \int dr\, n_s(r) \mathcal{W}(r,\eta) \int dr'\, r'^2 n_p(r') \int \frac{d^2\theta}{(2\pi)^3} \\
&\quad \times \int d^2k'_\perp\, P(k'_\perp) e^{-ir\boldsymbol{k}'_\perp \cdot \boldsymbol{\theta}} e^{ir'\boldsymbol{k}'_\perp \cdot (\boldsymbol{\theta} + \boldsymbol{R}/r)} 2\pi \delta_D(r - r'), \qquad (5.33) \\
&= b_s b_p \int dr\, r^2 n_s(r) \mathcal{W}(r,\eta) n_p(r) \int \frac{d^2\theta}{(2\pi)^2} \int d^2k'_\perp\, P(k'_\perp) e^{-ir\boldsymbol{k}'_\perp \cdot \boldsymbol{\theta}} e^{ir\boldsymbol{k}'_\perp \cdot (\boldsymbol{\theta} + \boldsymbol{R}/r)}. \qquad (5.34)
\end{aligned}$$

Now, the $\boldsymbol{\theta}$ terms cancel, making the integral over that variable trivial:

$$\begin{aligned}
\langle N_s N_p \rangle &= b_s b_p \int dr\, r^2 n_s(r) \mathcal{W}(r,\eta) n_p(r)\, \frac{4\pi}{(2\pi)^2} \int d^2k'_\perp\, P(k'_\perp) e^{ir\boldsymbol{k}'_\perp \cdot \boldsymbol{R}/r}, \qquad (5.35) \\
&= \frac{b_s b_p}{\pi} \int dr\, r^2 n_s(r) \mathcal{W}(r,\eta) n_p(r) \int d^2k'_\perp\, P(k'_\perp) e^{i\boldsymbol{k}'_\perp \cdot \boldsymbol{R}}. \qquad (5.36)
\end{aligned}$$

We can then identify:

$$w_p(\boldsymbol{R}) \equiv \frac{1}{2\pi} \int d^2k'_\perp\, P(k'_\perp) e^{i\boldsymbol{k}'_\perp \cdot \boldsymbol{R}}, \qquad (5.37)$$

where w_p is the projected correlation function, which has been used extensively in galaxy clustering analyses (e.g., Coil et al. 2008; Zehavi et al. 2011; Nuza et al. 2013) as it is less affected by redshift space distortions. The function w_p can be calculated as the line-of-sight integral of the three-dimensional correlation function,

$$w_p = \int_{-\infty}^{\infty} dr_\parallel \xi(r_\perp, r_\parallel). \qquad (5.38)$$

Returning to our derivation, we find

$$\langle N_s N_p \rangle = 2 b_s b_p \int dr\, r^2 n_s(r) \mathcal{W}(r,\eta) n_p(r) w_p(\boldsymbol{R}). \qquad (5.39)$$

Finally, this yields

$$\langle w(\boldsymbol{R})\rangle = \frac{b_s b_p}{2\pi} w_p(\boldsymbol{R}) \frac{\int dr\, r^2 n_s(r)\mathcal{W}(r,\eta) n_p(r)}{\int dr\, n_s(r)\mathcal{W}(r,\eta)\int dr'\, r'^2 n_p(r')}. \tag{5.40}$$

To gain some intuition for the behavior of $\langle w\rangle$, we assume that the distributions of the spectroscopic and photometric galaxies are given by boxcar functions of lengths L_s and L_p, respectively, which represent the depths of the survey, and $L_s < L_p$. Let us also assume the weighting is independent of r, and equal to 1. In that case, the integral normalization gives:

$$\frac{\int dr\, r^2 n_s(r)\mathcal{W}(r,\eta) n_p(r)}{\int dr\, n_s(r)\mathcal{W}(r,\eta)\int dr'\, r'^2 n_p(r')} = \frac{\int_{-L_s/2}^{L_s/2} dr\, r^2}{\int_{-L_s/2}^{L_s/2} dr \int_{-L_p/2}^{L_p/2} dr'\, r'^2} = \frac{L_s^3}{L_p^3 L_s} = \frac{L_s^2}{L_p^3} \sim \frac{1}{L}. \tag{5.41}$$

Accordingly, we see that this factor roughly scales as the inverse of the depth of the survey.

5.4.2 Covariance

The covariance is given by:

$$C(\boldsymbol{R},\boldsymbol{S}) \equiv \langle [w(\boldsymbol{R}) - \langle w(\boldsymbol{R})\rangle][w(\boldsymbol{S}) - \langle w(\boldsymbol{S})\rangle]\rangle, \tag{5.42}$$

$$= \langle [w(\boldsymbol{R})w(\boldsymbol{S}) - \langle w(\boldsymbol{S})\rangle w(\boldsymbol{R}) - \langle w(\boldsymbol{R})\rangle w(\boldsymbol{S}) + \langle w(\boldsymbol{R})\rangle\langle w(\boldsymbol{S})\rangle]\rangle, \tag{5.43}$$

$$= \langle w(\boldsymbol{R})w(\boldsymbol{S})\rangle - \langle w(\boldsymbol{R})\rangle\langle w(\boldsymbol{S})\rangle. \tag{5.44}$$

The numerator of first term, which we will refer to as N_C for simplicity, in Equation (5.44) may be written out as:

$$\langle N_C\rangle = D_C\langle w(\boldsymbol{R})w(\boldsymbol{S})\rangle \tag{5.45}$$

$$= \int dr_1\, n_s(r_1)\mathcal{W}(r_1,\eta)\int dr_1'\, r_1'^2 n_p(r_1')\int dr_2\, n_s(r_2)\mathcal{W}(r_2,\eta)\int dr_2'\, r_2'^2 n_p(r_2')$$
$$\times \int d^2\theta_1 \int d^2\theta_2 \langle \delta_s(r_1,\boldsymbol{\theta}_1)\delta_p(r_1',\boldsymbol{\theta}_1 + \boldsymbol{R}/r_1)\delta_s(r_2,\boldsymbol{\theta}_2)\delta_p(r_2',\boldsymbol{\theta}_2 + \boldsymbol{S}/r_2)\rangle, \tag{5.46}$$

where D_C stands for the denominator. Again using the Dekel & Lahav (1999) formalism so that $\delta_g = b_g\delta + \epsilon_g$, this immediately becomes:

$$\begin{aligned}\langle N_C\rangle =& b_s^2 b_p^2 \int dr_1\, n_s(r_1)\mathcal{W}(r_1,\eta)\int dr_1'\, r_1'^2 n_p(r_1')\int dr_2\, n_s(r_2)\mathcal{W}(r_2,\eta)\int dr_2'\, r_2'^2 n_p(r_2') \\ &\times \int d^2\theta_1 \int d^2\theta_2 \langle \delta(r_1,\boldsymbol{\theta}_1)\delta(r_1',\boldsymbol{\theta}_1+\boldsymbol{R}/r_1)\delta(r_2,\boldsymbol{\theta}_2)\delta(r_2',\boldsymbol{\theta}_2+\boldsymbol{S}/r_2)\rangle. \end{aligned} \tag{5.47}$$

The expectation value may be expressed as a Fourier transform:

$$\begin{aligned}\langle \delta(r_1,\boldsymbol{\theta}_1)\delta(r_1',\boldsymbol{\theta}_1+\boldsymbol{R}/r_1)\delta(r_2,\boldsymbol{\theta}_2)\delta(r_2',\boldsymbol{\theta}_2+\boldsymbol{S}/r_2)\rangle = \frac{1}{(2\pi)^6}\int\int\int\int d^3k d^3k' d^3q d^3q' \\ \times \langle \delta_{\boldsymbol{k}}\delta_{\boldsymbol{k}'}\delta_{\boldsymbol{q}}\delta_{\boldsymbol{q}'}\rangle e^{ir_1\boldsymbol{k}_\perp\cdot\boldsymbol{\theta}_1} e^{ir_1'\boldsymbol{k}_\perp'\cdot(\boldsymbol{\theta}_1+\boldsymbol{R}/r_1)} e^{ir_2\boldsymbol{q}_\perp\cdot\boldsymbol{\theta_2}} e^{ir_2'\boldsymbol{q}_\perp'\cdot(\boldsymbol{\theta}_2+\boldsymbol{S}/r_2)} e^{ir_1 k_\parallel} e^{ir_1' k_\parallel'} e^{ir_2 q_\parallel} e^{ir_2' q_\parallel'}. \end{aligned} \tag{5.48}$$

Using Wick's theorem, we can write the expectation value as:

$$\langle \delta_{\boldsymbol{k}}\delta_{\boldsymbol{k}'}\delta_{\boldsymbol{q}}\delta_{\boldsymbol{q}'}\rangle = \langle \delta_{\boldsymbol{k}}\delta_{\boldsymbol{k}'}\rangle\langle \delta_{\boldsymbol{q}}\delta_{\boldsymbol{q}'}\rangle + \langle \delta_{\boldsymbol{k}}\delta_{\boldsymbol{q}}\rangle\langle \delta_{\boldsymbol{k}'}\delta_{\boldsymbol{q}'}\rangle + \langle \delta_{\boldsymbol{k}}\delta_{\boldsymbol{q}'}\rangle\langle \delta_{\boldsymbol{k}'}\delta_{\boldsymbol{q}}\rangle. \tag{5.49}$$

The first term in this expansion can immediately be identified with $\langle w(\boldsymbol{R})\rangle\langle w(\boldsymbol{S})\rangle$, which cancels the second term in Equation (5.44). Then, we express the remaining factors in terms of the power spectrum:

$$\langle \delta_{\boldsymbol{k}}\delta_{\boldsymbol{q}}\rangle\langle \delta_{\boldsymbol{k}'}\delta_{\boldsymbol{q}'}\rangle = \delta_D^{(3)}(\boldsymbol{k}+\boldsymbol{q})P(q)\delta_D^{(3)}(\boldsymbol{k}'+\boldsymbol{q}')P(q'), \tag{5.50}$$

$$\langle \delta_{\boldsymbol{k}}\delta_{\boldsymbol{q}'}\rangle\langle \delta_{\boldsymbol{k}'}\delta_{\boldsymbol{q}}\rangle = \delta_D^{(3)}(\boldsymbol{k}+\boldsymbol{q}')P(q')\delta_D^{(3)}(\boldsymbol{k}'+\boldsymbol{q})P(q). \tag{5.51}$$

Let us denote the Fourier transform of the first of these terms by A and that of the second by B.

Beginning with term A, we find:

$$A = \frac{1}{(2\pi)^6}\int\int\int\int d^3k d^3k' d^3q d^3q' \,\langle\delta_{\boldsymbol{k}}\delta_{\boldsymbol{q}}\rangle\langle\delta_{\boldsymbol{k}'}\delta_{\boldsymbol{q}'}\rangle$$
$$\times e^{ir_1\boldsymbol{k}_\perp\cdot\boldsymbol{\theta}_1}e^{ir_1'\boldsymbol{k}_\perp'\cdot(\boldsymbol{\theta}_1+\boldsymbol{R}/r_1)}e^{ir_2\boldsymbol{q}_\perp\cdot\boldsymbol{\theta_2}}e^{ir_2'\boldsymbol{q}_\perp'\cdot(\boldsymbol{\theta}_2+\boldsymbol{S}/r_2)}e^{ir_1k_{\shortparallel}}e^{ir_1'k_{\shortparallel}'}e^{ir_2q_{\shortparallel}}e^{ir_2'q_{\shortparallel}'}, \tag{5.52}$$
$$= \frac{1}{(2\pi)^6}\int\int\int\int d^3k d^3k' d^3q d^3q' \,\delta_D^{(3)}(\boldsymbol{k}+\boldsymbol{q})P(q)\delta_D^{(3)}(\boldsymbol{k}'+\boldsymbol{q}')P(q')$$
$$\times e^{ir_1\boldsymbol{k}_\perp\cdot\boldsymbol{\theta}_1}e^{ir_1'\boldsymbol{k}_\perp'\cdot(\boldsymbol{\theta}_1+\boldsymbol{R}/r_1)}e^{ir_2\boldsymbol{q}_\perp\cdot\boldsymbol{\theta_2}}e^{ir_2'\boldsymbol{q}_\perp'\cdot(\boldsymbol{\theta}_2+\boldsymbol{S}/r_2)}e^{ir_1k_{\shortparallel}}e^{ir_1'k_{\shortparallel}'}e^{ir_2q_{\shortparallel}}e^{ir_2'q_{\shortparallel}'}, \tag{5.53}$$
$$= \frac{1}{(2\pi)^6}\int\int d^3k d^3k' \,P(k)P(k')e^{ir_1\boldsymbol{k}_\perp\cdot\boldsymbol{\theta}_1}e^{ir_1'\boldsymbol{k}_\perp'\cdot(\boldsymbol{\theta}_1+\boldsymbol{R}/r_1)}e^{-ir_2\boldsymbol{k}_\perp\cdot\boldsymbol{\theta_2}}e^{-ir_2'\boldsymbol{k}_\perp'\cdot(\boldsymbol{\theta}_2+\boldsymbol{S}/r_2)}$$
$$\times e^{ir_1k_{\shortparallel}}e^{ir_1'k_{\shortparallel}'}e^{-ir_2k_{\shortparallel}}e^{-ir_2'k_{\shortparallel}'}, \tag{5.54}$$
$$= \frac{1}{(2\pi)^6}\int\int d^3k d^3k' \,P(k)P(k')e^{ir_1\boldsymbol{k}_\perp\cdot\boldsymbol{\theta}_1}e^{ir_1'\boldsymbol{k}_\perp'\cdot(\boldsymbol{\theta}_1+\boldsymbol{R}/r_1)}e^{-ir_2\boldsymbol{k}_\perp\cdot\boldsymbol{\theta_2}}e^{-ir_2'\boldsymbol{k}_\perp'\cdot(\boldsymbol{\theta}_2+\boldsymbol{S}/r_2)}$$
$$\times e^{ik_{\shortparallel}(r_1-r_2)}e^{ik_{\shortparallel}'(r_1'-r_2')}. \tag{5.55}$$

We can again separate the integrals:

$$A = \frac{1}{(2\pi)^6}\int\int d^2k_\perp d^2k_\perp' \,P(k_\perp)P(k_\perp')e^{ir_1\boldsymbol{k}_\perp\cdot\boldsymbol{\theta}_1}e^{ir_1'\boldsymbol{k}_\perp'\cdot(\boldsymbol{\theta}_1+\boldsymbol{R}/r_1)}e^{-ir_2\boldsymbol{k}_\perp\cdot\boldsymbol{\theta_2}}e^{-ir_2'\boldsymbol{k}_\perp'\cdot(\boldsymbol{\theta}_2+\boldsymbol{S}/r_2)}$$
$$\times \int dk_{\shortparallel}\, e^{ik_{\shortparallel}(r_1-r_2)}\int dk_{\shortparallel}'\, e^{ik_{\shortparallel}'(r_1'-r_2')}, \tag{5.56}$$
$$= \frac{1}{(2\pi)^6}\int\int d^2k_\perp d^2k_\perp' \,P(k_\perp)P(k_\perp')e^{ir_1\boldsymbol{k}_\perp\cdot\boldsymbol{\theta}_1}e^{ir_1'\boldsymbol{k}_\perp'\cdot(\boldsymbol{\theta}_1+\boldsymbol{R}/r_1)}e^{-ir_2\boldsymbol{k}_\perp\cdot\boldsymbol{\theta_2}}e^{-ir_2'\boldsymbol{k}_\perp'\cdot(\boldsymbol{\theta}_2+\boldsymbol{S}/r_2)}$$
$$\times 2\pi\delta_D(r_1-r_2)2\pi\delta_D(r_1'-r_2'), \tag{5.57}$$
$$= \frac{1}{(2\pi)^4}\int\int d^2k_\perp d^2k_\perp' \,P(k_\perp)P(k_\perp')e^{ir_1\boldsymbol{k}_\perp\cdot\boldsymbol{\theta}_1}e^{ir_1'\boldsymbol{k}_\perp'\cdot(\boldsymbol{\theta}_1+\boldsymbol{R}/r_1)}e^{-ir_2\boldsymbol{k}_\perp\cdot\boldsymbol{\theta_2}}e^{-ir_2'\boldsymbol{k}_\perp'\cdot(\boldsymbol{\theta}_2+\boldsymbol{S}/r_2)}$$
$$\times \delta_D(r_1-r_2)\delta_D(r_1'-r_2'). \tag{5.58}$$

We may now insert this expression into Equation (5.47) to take advantage of the Dirac

delta functions:

$$\begin{aligned}
\langle A\rangle = & b_s^2 b_p^2 \int dr_1\, n_s(r_1)\mathcal{W}(r_1,\eta) \int dr_1'\, r_1'^2 n_p(r_1') \int dr_2\, n_s(r_2)\mathcal{W}(r_2,\eta) \int dr_2'\, r_2'^2 n_p(r_2') \\
& \times \frac{1}{(2\pi)^4} \int d^2\theta_1 \int d^2\theta_2 \int\int d^2k_\perp d^2k_\perp'\; P(k_\perp)P(k_\perp') e^{ir_1 \boldsymbol{k}_\perp\cdot\boldsymbol{\theta}_1} e^{ir_1'\boldsymbol{k}_\perp'\cdot(\boldsymbol{\theta}_1+\boldsymbol{R}/r_1)} \\
& \times e^{-ir_2\boldsymbol{k}_\perp\cdot\boldsymbol{\theta_2}} e^{-ir_2'\boldsymbol{k}_\perp'\cdot(\boldsymbol{\theta}_2+\boldsymbol{S}/r_2)} \delta_D(r_1-r_2)\delta_D(r_1'-r_2'), \qquad (5.59) \\
= & \frac{b_s^2 b_p^2}{(2\pi)^4} \int dr_1\, n_s(r_1)^2\mathcal{W}(r_1,\eta)^2 \int dr_1'\, r_1'^4 n_p(r_1')^2 \int\int d^2k_\perp d^2k_\perp'\; P(k_\perp)P(k_\perp') \\
& \times e^{i(r_1'/r_1)\boldsymbol{k}_\perp'\cdot\boldsymbol{R}} e^{-i(r_1'/r_1)\boldsymbol{k}_\perp'\cdot\boldsymbol{S}} \int d^2\theta_1\, e^{i(r_1\boldsymbol{k}_\perp+r_1'\boldsymbol{k}_\perp')\cdot\boldsymbol{\theta}_1} \int d^2\theta_2\, e^{-i(r_1\boldsymbol{k}_\perp+r_1'\boldsymbol{k}_\perp')\cdot\boldsymbol{\theta}_2}, \qquad (5.60) \\
= & \frac{b_s^2 b_p^2}{(2\pi)^4} \int dr_1\, n_s(r_1)^2\mathcal{W}(r_1,\eta)^2 \int dr_1'\, r_1'^4 n_p(r_1')^2 \int\int d^2k_\perp d^2k_\perp'\; P(k_\perp)P(k_\perp') \\
& \times e^{i(r_1'/r_1)\boldsymbol{k}_\perp'\cdot(\boldsymbol{R}-\boldsymbol{S})} (2\pi)^2 \delta_D^{(2)}(r_1\boldsymbol{k}_\perp + r_1'\boldsymbol{k}_\perp'), \qquad (5.61) \\
= & \frac{b_s^2 b_p^2}{(2\pi)^2} \int dr_1\, n_s(r_1)^2\mathcal{W}(r_1,\eta)^2 \int dr_1'\, r_1'^4 n_p(r_1')^2 \int d^2k_\perp P(k_\perp)P(r_1k_\perp/r_1') e^{-i\boldsymbol{k}_\perp\cdot(\boldsymbol{R}-\boldsymbol{S})}. \\
& \qquad (5.62)
\end{aligned}$$

Now, let $\boldsymbol{u} = r_1\boldsymbol{k}_\perp$, so that:

$$\langle A\rangle = \frac{b_s^2 b_p^2}{(2\pi)^4} \int dr_1\, n_s(r_1)^2\mathcal{W}(r_1,\eta)^2 \int dr_1'\, r_1'^4 n_p(r_1')^2 \int \frac{d^2u}{r_1^2} P\left(\frac{u}{r_1}\right) P\left(\frac{u}{r_1'}\right) e^{i\boldsymbol{u}\cdot(\boldsymbol{S}-\boldsymbol{R})/r_1}, \qquad (5.63)$$

which yields:

$$\langle A\rangle = \frac{b_s^2 b_p^2}{(2\pi)^4} \int dr_1\, n_s(r_1)^2\mathcal{W}(r_1,\eta)^2 \int dr_1' r_1'^4 n_p(r_1')^2 \int d^2u\, P\left(\frac{u}{r_1}\right) P\left(\frac{u}{r_1'}\right) e^{i\boldsymbol{u}\cdot(\boldsymbol{S}-\boldsymbol{R})/r_1}. \qquad (5.64)$$

We can proceed along similar lines for term B.

$$B = \frac{1}{(2\pi)^6}\int\int\int\int d^3k d^3k' d^3q d^3q'\ \langle\delta_{\boldsymbol{k}}\delta_{\boldsymbol{q'}}\rangle\langle\delta_{\boldsymbol{k'}}\delta_{\boldsymbol{q}}\rangle$$
$$\times\ e^{ir_1\boldsymbol{k}_\perp\cdot\boldsymbol{\theta}_1}e^{ir_1'\boldsymbol{k}_\perp'\cdot(\boldsymbol{\theta}_1+\boldsymbol{R}/r_1)}e^{ir_2\boldsymbol{q}_\perp\cdot\boldsymbol{\theta_2}}e^{ir_2'\boldsymbol{q}_\perp'\cdot(\boldsymbol{\theta}_2+\boldsymbol{S}/r_2)}e^{ir_1k_\shortparallel}e^{ir_1'k_\shortparallel'}e^{ir_2q_\shortparallel}e^{ir_2'q_\shortparallel'}, \tag{5.65}$$
$$= \frac{1}{(2\pi)^6}\int\int\int\int d^3k d^3k' d^3q d^3q'\ \delta_D^{(3)}(\boldsymbol{k}+\boldsymbol{q}')P(q')\delta_D^{(3)}(\boldsymbol{k}'+\boldsymbol{q})P(q)$$
$$\times\ e^{ir_1\boldsymbol{k}_\perp\cdot\boldsymbol{\theta}_1}e^{ir_1'\boldsymbol{k}_\perp'\cdot(\boldsymbol{\theta}_1+\boldsymbol{R}/r_1)}e^{ir_2\boldsymbol{q}_\perp\cdot\boldsymbol{\theta_2}}e^{ir_2'\boldsymbol{q}_\perp'\cdot(\boldsymbol{\theta}_2+\boldsymbol{S}/r_2)}e^{ir_1k_\shortparallel}e^{ir_1'k_\shortparallel'}e^{ir_2q_\shortparallel}e^{ir_2'q_\shortparallel'}, \tag{5.66}$$
$$= \frac{1}{(2\pi)^6}\int\int d^3k d^3k'\ P(k)P(k')e^{ir_1\boldsymbol{k}_\perp\cdot\boldsymbol{\theta}_1}e^{ir_1'\boldsymbol{k}_\perp'\cdot(\boldsymbol{\theta}_1+\boldsymbol{R}/r_1)}e^{-ir_2\boldsymbol{k}_\perp'\cdot\boldsymbol{\theta_2}}e^{-ir_2'\boldsymbol{k}_\perp\cdot(\boldsymbol{\theta}_2+\boldsymbol{S}/r_2)}$$
$$\times\ e^{ir_1k_\shortparallel}e^{ir_1'k_\shortparallel'}e^{-ir_2k_\shortparallel'}e^{-ir_2'k_\shortparallel}, \tag{5.67}$$
$$= \frac{1}{(2\pi)^6}\int\int d^3k d^3k'\ P(k)P(k')e^{ir_1\boldsymbol{k}_\perp\cdot\boldsymbol{\theta}_1}e^{ir_1'\boldsymbol{k}_\perp'\cdot(\boldsymbol{\theta}_1+\boldsymbol{R}/r_1)}e^{-ir_2\boldsymbol{k}_\perp'\cdot\boldsymbol{\theta_2}}e^{-ir_2'\boldsymbol{k}_\perp\cdot(\boldsymbol{\theta}_2+\boldsymbol{S}/r_2)}$$
$$\times\ e^{i(r_1-r_2')k_\shortparallel}e^{i(r_1'-r_2)k_\shortparallel'}. \tag{5.68}$$

We split the integrals, assuming small angles:

$$B = \frac{1}{(2\pi)^6}\int\int d^2k_\perp d^2k_\perp'\ P(k_\perp)P(k_\perp')e^{ir_1\boldsymbol{k}_\perp\cdot\boldsymbol{\theta}_1}e^{ir_1'\boldsymbol{k}_\perp'\cdot(\boldsymbol{\theta}_1+\boldsymbol{R}/r_1)}e^{-ir_2\boldsymbol{k}_\perp'\cdot\boldsymbol{\theta_2}}e^{-ir_2'\boldsymbol{k}_\perp\cdot(\boldsymbol{\theta}_2+\boldsymbol{S}/r_2)}$$
$$\times\int dk_\shortparallel\, e^{i(r_1-r_2')k_\shortparallel}\int dk_\shortparallel'\, e^{i(r_1'-r_2)k_\shortparallel'}, \tag{5.69}$$
$$= \frac{1}{(2\pi)^6}\int\int d^2k_\perp d^2k_\perp'\ P(k_\perp)P(k_\perp')e^{ir_1\boldsymbol{k}_\perp\cdot\boldsymbol{\theta}_1}e^{ir_1'\boldsymbol{k}_\perp'\cdot(\boldsymbol{\theta}_1+\boldsymbol{R}/r_1)}e^{-ir_2\boldsymbol{k}_\perp'\cdot\boldsymbol{\theta_2}}e^{-ir_2'\boldsymbol{k}_\perp\cdot(\boldsymbol{\theta}_2+\boldsymbol{S}/r_2)}$$
$$\times\ 2\pi\delta_D(r_1-r_2')2\pi\delta_D(r_1'-r_2), \tag{5.70}$$
$$= \frac{1}{(2\pi)^4}\int\int d^2k_\perp d^2k_\perp'\ P(k_\perp)P(k_\perp')e^{ir_1\boldsymbol{k}_\perp\cdot\boldsymbol{\theta}_1}e^{ir_1'\boldsymbol{k}_\perp'\cdot(\boldsymbol{\theta}_1+\boldsymbol{R}/r_1)}e^{-ir_2\boldsymbol{k}_\perp'\cdot\boldsymbol{\theta_2}}e^{-ir_2'\boldsymbol{k}_\perp\cdot(\boldsymbol{\theta}_2+\boldsymbol{S}/r_2)}$$
$$\times\ \delta_D(r_1-r_2')\delta_D(r_1'-r_2). \tag{5.71}$$

Plugging this into Equation (5.47) yields

$$\begin{aligned}\langle B\rangle = b_s^2 b_p^2 \int dr_1\, n_s(r_1)\mathcal{W}(r_1,\eta)\int dr_1'\, r_1'^2 n_p(r_1')\int dr_2\, n_s(r_2)\mathcal{W}(r_2,\eta)\int dr_2'\, r_2'^2 n_p(r_2')\\ \times \frac{1}{(2\pi)^4}\int d^2\theta_1\int d^2\theta_2\int\int d^2k_\perp d^2k_\perp'\, P(k_\perp)P(k_\perp')e^{ir_1\boldsymbol{k}_\perp\cdot\boldsymbol{\theta}_1}e^{ir_1'\boldsymbol{k}_\perp'\cdot(\boldsymbol{\theta}_1+\boldsymbol{R}/r_1)}\\ \times e^{-ir_2\boldsymbol{k}_\perp'\cdot\boldsymbol{\theta_2}}e^{-ir_2'\boldsymbol{k}_\perp\cdot(\boldsymbol{\theta}_2+\boldsymbol{S}/r_2)}\delta_D(r_1-r_2')\delta_D(r_1'-r_2), \qquad (5.72)\\ = \frac{b_s^2 b_p^2}{(2\pi)^4}\int dr_1\, r_1^2 n_s(r_1)\mathcal{W}(r_1,\eta)n_p(r_1)\int dr_1'\, r_1'^2 n_s(r_1')\mathcal{W}(r_1',\eta)n_p(r_1')\\ \times\int\int d^2k_\perp d^2k_\perp'\, P(k_\perp)P(k_\perp')e^{i(r_1'/r_1)\boldsymbol{k}_\perp'\cdot\boldsymbol{R}}e^{-i(r_1/r_1')\boldsymbol{k}_\perp\cdot\boldsymbol{S}}\\ \times\int d^2\theta_1\, e^{i(r_1\boldsymbol{k}_\perp+r_1'\boldsymbol{k}_\perp')\cdot\boldsymbol{\theta}_1}\int d^2\theta_2\, e^{-i(r_1\boldsymbol{k}_\perp+r_1'\boldsymbol{k}_\perp')\cdot\boldsymbol{\theta}_2}, \qquad (5.73)\\ = \frac{b_s^2 b_p^2}{(2\pi)^4}\int dr_1\, r_1^2 n_s(r_1)\mathcal{W}(r_1,\eta)n_p(r_1)\int dr_1'\, r_1'^2 n_s(r_1')\mathcal{W}(r_1',\eta)n_p(r_1')\\ \times\int\int d^2k_\perp d^2k_\perp'\, P(k_\perp)P(k_\perp')e^{i(r_1'/r_1)\boldsymbol{k}_\perp'\cdot\boldsymbol{R}}e^{-i(r_1/r_1')\boldsymbol{k}_\perp\cdot\boldsymbol{S}}(2\pi)^2\delta_D^{(2)}(r_1\boldsymbol{k}_\perp+r_1'\boldsymbol{k}_\perp'),\\ \qquad (5.74)\\ = \frac{b_s^2 b_p^2}{(2\pi)^2}\int dr_1\, r_1^2 n_s(r_1)\mathcal{W}(r_1,\eta)n_p(r_1)\int dr_1'\, r_1'^2 n_s(r_1')\mathcal{W}(r_1',\eta)n_p(r_1')\\ \times\int d^2k_\perp\, P(k_\perp)P(r_1k_\perp/r_1')e^{-i\boldsymbol{k}_\perp\cdot\boldsymbol{R}}e^{-i(r_1/r_1')\boldsymbol{k}_\perp\cdot\boldsymbol{S}}. \qquad (5.75)\end{aligned}$$

We set $\boldsymbol{u} = r_1\boldsymbol{k}_\perp$ again, so that:

$$\begin{aligned}\langle B\rangle = \frac{b_s^2 b_p^2}{(2\pi)^2}\int dr_1\, r_1^2 n_s(r_1)\mathcal{W}(r_1,\eta)n_p(r_1)\int dr_1'\, r_1'^2 n_s(r_1')\mathcal{W}(r_1',\eta)n_p(r_1')\\ \times\int d^2u\,\frac{1}{r_1^2}P\left(\frac{u}{r_1}\right)P\left(\frac{u}{r_1'}\right)e^{-i\boldsymbol{u}\cdot\boldsymbol{R}/r_1}e^{-i\boldsymbol{u}\cdot\boldsymbol{S}/r_1'}. \qquad (5.76)\end{aligned}$$

This yields

$$\begin{aligned}\langle B\rangle = \frac{b_s^2 b_p^2}{(2\pi)^2}\int dr_1\, n_s(r_1)\mathcal{W}(r_1,\eta)n_p(r_1)\int dr_1'\, r_1'^2 n_s(r_1')\mathcal{W}(r_1',\eta)n_p(r_1')\\ \times\int d^2u\, P\left(\frac{u}{r_1}\right)P\left(\frac{u}{r_1'}\right)e^{-i\boldsymbol{u}\cdot(\boldsymbol{R}/r_1+\boldsymbol{S}/r_1')} \qquad (5.77)\end{aligned}$$

Lastly, the denominator of the covariance is given by:

$$D_C = \int dr_1\, n_s(r_1)\mathcal{W}(r_1,\eta)\int dr_1'\, r_1'^2 n_p(r_1')\int dr_2\, r_2^2 n_s(r_2)\mathcal{W}(r_2,\eta)\int dr_2'\, r_2'^2 n_p(r_2') \times \int d^2\theta_1 \int d^2\theta_2, \tag{5.78}$$

$$= (4\pi)^2 \int dr_1\, n_s(r_1)\mathcal{W}(r_1,\eta)\int dr_1'\, r_1'^2 n_p(r_1')\int dr_2\, n_s(r_2)\mathcal{W}(r_2,\eta)\int dr_2'\, r_2'^2 n_p(r_2'). \tag{5.79}$$

Accordingly, with:

$$C(\boldsymbol{R},\boldsymbol{S}) = \frac{\langle N_C\rangle}{D_C}, \tag{5.80}$$

we obtain

$$C(\boldsymbol{R},\boldsymbol{S}) = \frac{b_s^2 b_p^2}{64\pi^4}\Bigg(\int dr_1\, n_s(r_1)^2\mathcal{W}(r_1,\eta)^2\int dr_1'\, r_1'^4 n_p(r_1')^2 \times \int d^2u\, P\left(\frac{u}{r_1}\right)P\left(\frac{u}{r_1'}\right)e^{i\boldsymbol{u}\cdot(\boldsymbol{S}-\boldsymbol{R})/r_1} + \int dr_1\, r_1^2 n_s(r_1)\mathcal{W}(r_1,\eta)n_p(r_1) \times \int dr_1'\, r_1'^2 n_s(r_1')\mathcal{W}(r_1',\eta)n_p(r_1')\int d^2u\, P\left(\frac{u}{r_1}\right)P\left(\frac{u}{r_1'}\right)e^{-i\boldsymbol{u}\cdot(\boldsymbol{R}/r_1+\boldsymbol{S}/r_1')}\Bigg) \times \left[\int dr_1 n_s(r_1)\mathcal{W}(r_1,\eta)\int dr_1' r_1'^2 n_p(r_1')\int dr_2 n_s(r_2)\mathcal{W}(r_2,\eta)\int dr_2' r_2'^2 n_p(r_2')\right]^{-1}. \tag{5.81}$$

We see that the covariance matrix has two distinct terms: the first integrates over the spectroscopic and photometric samples separately, whereas the second mixes the two samples.

5.4.3 Binning

Binning data leads us to the following representation of the correlation function in an annulus bounded by R_1, R_2:

$$W(R_1, R_2) = 2\int_{R_1}^{R_2} \frac{R\,dR}{\pi\,(R_2^2 - R_1^2)} \int \frac{d\phi}{2\pi} \langle w(\boldsymbol{R})\rangle. \tag{5.82}$$

Beginning with Equation 5.40, which gives:

$$\langle w(\boldsymbol{R})\rangle = \frac{b_s b_p}{2\pi} w_p(\boldsymbol{R}) \frac{\int dr\, r^2 n_s(r)\mathcal{W}(r,\eta) n_p(r)}{\int dr\, n_s(r)\mathcal{W}(r,\eta)\int dr'\, r'^2 n_p(r')}, \tag{5.83}$$

$$= \frac{b_s b_p}{(2\pi)^2}\int d^2k'_\perp\, P(k'_\perp) e^{i\boldsymbol{k}'_\perp\cdot\boldsymbol{R}} \frac{\int dr\, r^2 n_s(r)\mathcal{W}(r,\eta) n_p(r)}{\int dr\, n_s(r)\mathcal{W}(r,\eta)\int dr'\, r'^2 n_p(r')}, \tag{5.84}$$

and writing $\boldsymbol{k}_\perp{}' \cdot \boldsymbol{R} = k'_\perp R\cos(\phi)$, we obtain the following representation in terms of the Bessel function J_0:

$$W(R_1, R_2) = \frac{b_s b_p}{4\pi^4\,(R_2^2 - R_1^2)} \frac{\int dr\, r^2 n_s(r)\mathcal{W}(r,\eta) n_p(r)}{\int dr\, n_s(r)\mathcal{W}(r,\eta)\int dr'\, r'^2 n_p(r')} \int d^2k'_\perp\, P(k'_\perp) \times \int_{R_1}^{R_2} R\,dR \int d\phi\, e^{ik'_\perp R\cos(\phi)}, \tag{5.85}$$

$$W(R_1, R_2) = \frac{b_s b_p}{4\pi^4\,(R_2^2 - R_1^2)} \frac{\int dr\, r^2 n_s(r)\mathcal{W}(r,\eta) n_p(r)}{\int dr\, n_s(r)\mathcal{W}(r,\eta)\int dr'\, r'^2 n_p(r')} \int d^2k'_\perp\, P(k'_\perp) \times \int_{R_1}^{R_2} R\,dR\, J_0(k'_\perp R). \tag{5.86}$$

Now, the integral over R can be done by making use of the properties of Bessel functions, leading to a final result of:

$$W(R_1, R_2) = \frac{b_s b_p}{4\pi^4\,(R_2^2 - R_1^2)} \frac{\int dr\, r^2 n_s(r)\mathcal{W}(r,\eta) n_p(r)}{\int dr\, n_s(r)\mathcal{W}(r,\eta)\int dr'\, r'^2 n_p(r')} \times \int d^2k'_\perp\, P(k'_\perp) \left[\frac{R_2 J_1(k'_\perp R_2) - R_1 J_1(k'_\perp R_1)}{k'_\perp}\right]. \tag{5.87}$$

We also compute the binned covariance. In this case we have two terms to consider:

$$C_1 \sim \int d^2u\, P\left(\frac{u}{r_1}\right) P\left(\frac{u}{r_1'}\right) e^{i\boldsymbol{u}\cdot(\boldsymbol{S}-\boldsymbol{R})/r_1}, \tag{5.88}$$

$$C_2 \sim \int d^2u\, P\left(\frac{u}{r_1}\right) P\left(\frac{u}{r_1'}\right) e^{-i\boldsymbol{u}\cdot(\boldsymbol{R}/r_1+\boldsymbol{S}/r_1')}. \tag{5.89}$$

Accordingly, for the first term we find:

$$C_{1,b} \sim 4\int_{R_1}^{R_2} \frac{R\,dR}{\pi\left(R_2^2-R_1^2\right)} \int \frac{d\phi_R}{2\pi} \int_{S_1}^{S_2} \frac{S\,dS}{\pi\left(S_2^2-S_1^2\right)} \int \frac{d\phi_S}{2\pi} \times \int d^2u\, P\left(\frac{u}{r_1}\right) P\left(\frac{u}{r_1'}\right) e^{i\boldsymbol{u}\cdot(\boldsymbol{S}-\boldsymbol{R})/r_1}, \tag{5.90}$$

which, with $\boldsymbol{u}\cdot\boldsymbol{R} = uR\cos(\phi_R)$ and $\boldsymbol{u}\cdot\boldsymbol{S} = uS\cos(\phi_S)$, becomes:

$$C_{1,b} \sim \frac{1}{\pi^4\left(R_2^2-R_1^2\right)\left(S_2^2-S_1^2\right)} \int d^2u\, P\left(\frac{u}{r_1}\right) P\left(\frac{u}{r_1'}\right) \times \int R\,dR \int d\phi_R\, e^{iuR\cos(\phi_R)/r_1} \int S\,dS \int d\phi_S\, e^{-iuS\cos(\phi_S)/r_1}, \tag{5.91}$$

$$\sim \frac{1}{\pi^4\left(R_2^2-R_1^2\right)\left(S_2^2-S_1^2\right)} \int d^2u\, P\left(\frac{u}{r_1}\right) P\left(\frac{u}{r_1'}\right) \int R\,dR\, J_0\left(\frac{uR}{r_1}\right) \int S\,dS\, J_0\left(\frac{uS}{r_1}\right), \tag{5.92}$$

$$\sim \frac{1}{\pi^4\left(R_2^2-R_1^2\right)\left(S_2^2-S_1^2\right)} \int d^2u\, P\left(\frac{u}{r_1}\right) P\left(\frac{u}{r_1'}\right) \left[\frac{r_1^2}{u^2}\right] \left[R_2 J_1\left(\frac{uR_2}{r_1}\right) - R_1 J_1\left(\frac{uR_1}{r_1}\right)\right] \times \left[S_2 J_1\left(\frac{uS_2}{r_1}\right) - S_1 J_1\left(\frac{uS_1}{r_1}\right)\right]. \tag{5.93}$$

For the second term,

$$C_{2,b} \sim 4 \int_{R_1}^{R_2} \frac{R\,dR}{\pi\,(R_2^2 - R_1^2)} \int \frac{d\phi_R}{2\pi} \int_{S_1}^{S_2} \frac{S\,dS}{\pi\,(S_2^2 - S_1^2)} \int \frac{d\phi_S}{2\pi} \times \int d^2u\, P\left(\frac{u}{r_1}\right) P\left(\frac{u}{r_1'}\right) e^{-i\boldsymbol{u}\cdot(\boldsymbol{R}/r_1 + \boldsymbol{S}/r_1')}, \tag{5.94}$$

$$\sim \frac{1}{\pi^4\,(R_2^2 - R_1^2)\,(S_2^2 - S_1^2)} \int d^2u\, P\left(\frac{u}{r_1}\right) P\left(\frac{u}{r_1'}\right) \times \int R\,dR \int d\phi_R\, e^{-iuR\cos(\phi_R)/r_1} \int S\,dS \int d\phi_S\, e^{-iuS\cos(\phi_S)/r_1'}, \tag{5.95}$$

$$\sim \frac{1}{\pi^4\,(R_2^2 - R_1^2)\,(S_2^2 - S_1^2)} \int d^2u\, P\left(\frac{u}{r_1}\right) P\left(\frac{u}{r_1'}\right) \int R\,dR\, J_0\left(\frac{uR}{r_1}\right) \int S\,dS\, J_0\left(\frac{uS}{r_1'}\right), \tag{5.96}$$

$$\sim \frac{1}{\pi^4\,(R_2^2 - R_1^2)\,(S_2^2 - S_1^2)} \int d^2u\, P\left(\frac{u}{r_1}\right) P\left(\frac{u}{r_1'}\right) \left[\frac{r_1 r_1'}{u^2}\right] \times \left[R_2 J_1\left(\frac{uR_2}{r_1}\right) - R_1 J_1\left(\frac{uR_1}{r_1}\right)\right] \left[S_2 J_1\left(\frac{uS_2}{r_1'}\right) - S_1 J_1\left(\frac{uS_1}{r_1'}\right)\right]. \tag{5.97}$$

Thus, the binned covariance becomes (c.f. Eq. 5.81), with C a function of four quantities R_1, R_2, S_1, S_2:

$$\begin{aligned} C = & \frac{b_s^2 b_p^2 \left[\int dr_1\, n_s(r_1) \mathcal{W}(r_1,\eta) \int dr_1'\, r_1'^2 n_p(r_1') \int dr_2\, n_s(r_2) \mathcal{W}(r_2,\eta) \int dr_2'\, r_2'^2 n_p(r_2')\right]^{-1}}{64\pi^8\,\left[(R_2^2 - R_1^2)\,(S_2^2 - S_1^2)\right]^2} \\ & \times \left(\int dr_1\, r_1^2 n_s(r_1)^2 \mathcal{W}(r_1,\eta)^2 \int dr_1'\, r_1'^4 n_p(r_1')^2 \int \frac{d^2u}{u^2}\, P\left(\frac{u}{r_1}\right) P\left(\frac{u}{r_1'}\right) \right. \\ & \quad \times \left[R_2 J_1\left(\frac{uR_2}{r_1}\right) - R_1 J_1\left(\frac{uR_1}{r_1}\right)\right] \left[S_2 J_1\left(\frac{uS_2}{r_1}\right) - S_1 J_1\left(\frac{uS_1}{r_1}\right)\right] \\ & + \int dr_1\, r_1^3 n_s(r_1) \mathcal{W}(r_1,\eta) n_p(r_1) \int dr_1'\, r_1'^3 n_s(r_1') \mathcal{W}(r_1',\eta) n_p(r_1') \int \frac{d^2u}{u^2}\, P\left(\frac{u}{r_1}\right) P\left(\frac{u}{r_1'}\right) \\ & \left. \times \left[R_2 J_1\left(\frac{uR_2}{r_1}\right) - R_1 J_1\left(\frac{uR_1}{r_1}\right)\right] \left[S_2 J_1\left(\frac{uS_2}{r_1'}\right) - S_1 J_1\left(\frac{uS_1}{r_1'}\right)\right] \right). \end{aligned} \tag{5.98}$$

5.5 Results

We compute the projected correlation function $w(R)$ using the Landy-Szalay estimator with a binning of 5 h^{-1}Mpc; the result is plotted in Figure 5.1. We fit two computed projected correlation functions, one derived using a CAMB power spectrum (Lewis, Challinor, & Lasenby 2000) that includes the BAO, and the other a smooth, BAO-less power spectrum derived using the prescriptions of Eisenstein & Hu (1998), to the data. In both theoretical prescriptions of the correlation function, we include a nuisance parameter in the form of an additive constant w_0, which corresponds to excess power at very large scales and which is left a free parameter.

Accordingly, we fit to a function of the form $w = aw_c + w_0$, where w_c is the calculated correlation function and a and w_0 are parameters to be found. Prior to fitting, we normalize w_c to the value of the data at $R = 27.5$ h^{-1}Mpc. We obtain a $\chi^2/\mathrm{ndf} = 23.339/23 = 1.015$ for the BAO curve and a $\chi^2/\mathrm{ndf} = 26.891/23 = 1.169$ for the no BAO curve, with $\Delta\chi^2 = 3.6$. In both cases, w_0 is a little under 3×10^{-4}, indicating only a modest level of systematics. Thus, our results indicate a 1.9σ preference for the BAO.

The results in Figure 5.1 align well with the prediction for the correlation function with BAO at intermediate-to-large scales. We note that while we do not have to consider redshift-space distortions with w, since we do not account for where the photometric galaxies are located along the line of sight, there are non-linear corrections that could have some impact at small scales ($R \lesssim 10$ h^{-1}Mpc), but these are not expected to yield major changes at large scales. Accordingly, our measurements yield a feature consistent

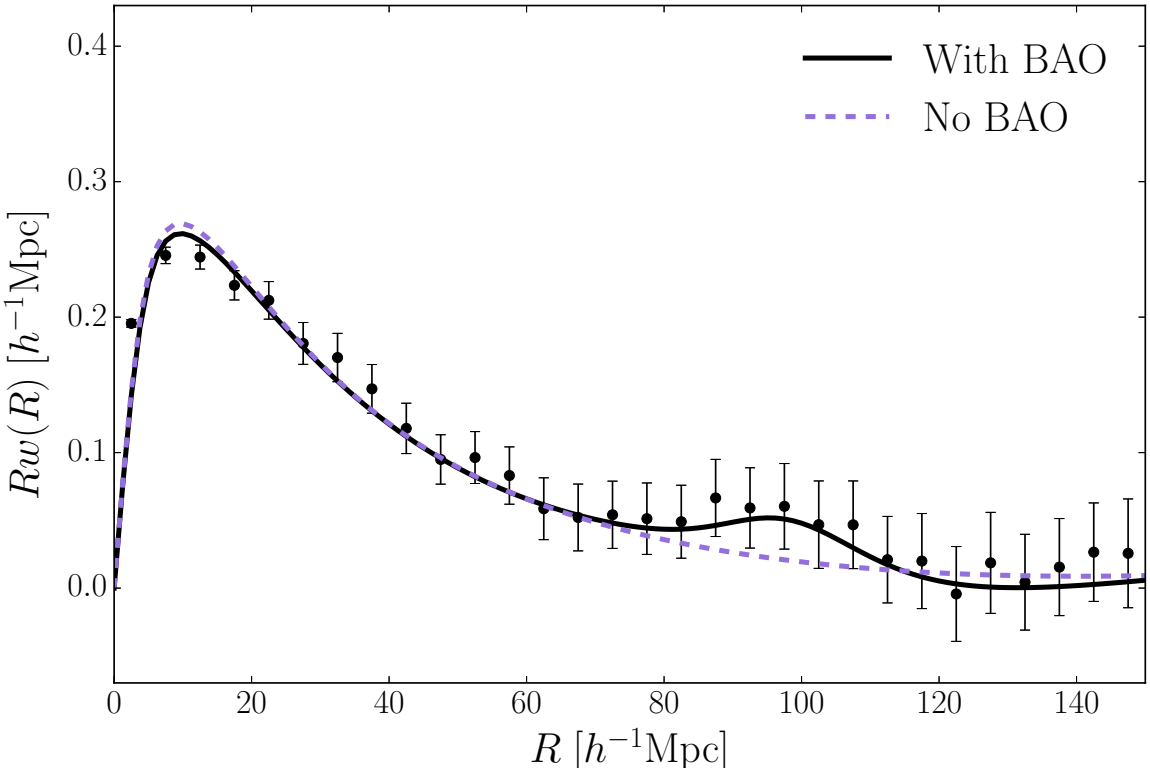

Figure 5.1.—: The projected correlation function w plotted against two theoretical curves: the solid black line is the predicted projected correlation function in the presence of BAO, while the dashed violet curve is the expectation without BAO. The data show a bump near 100 h^{-1}Mpc consistent with the BAO signal.

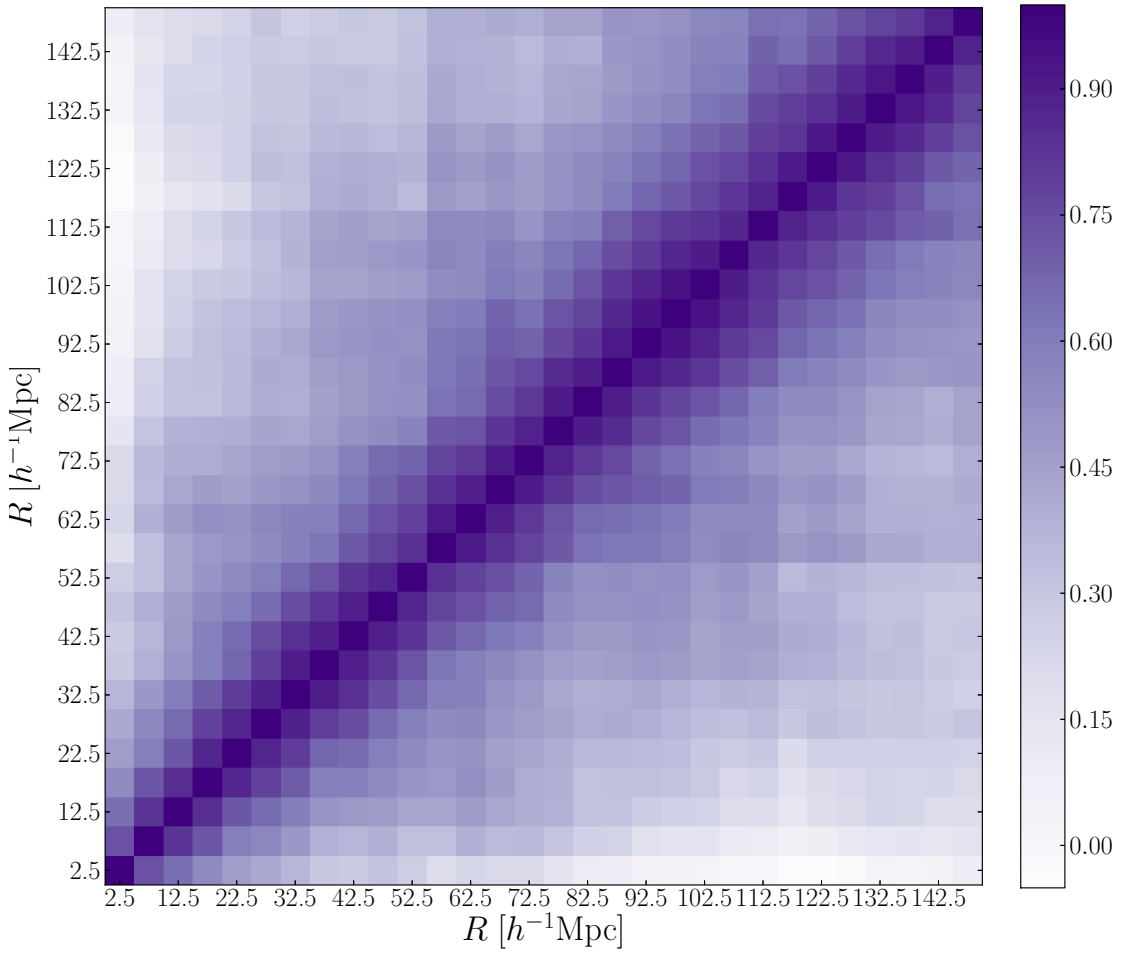

Figure 5.2.—: The reduced covariance matrix for the cross-correlation, estimated from the Voronoi jackknife samples and used to fit theoretical curves to w.

with the BAO signal at $R \sim 100\ h^{-1}$Mpc in the projected correlation function.

5.6 Summary and Conclusions

In this work, we have laid out a new method for detecting the BAO in sparse spectroscopic datasets by cross-correlating the spectroscopy with photometry, for which greater densities of galaxies can be attained at far smaller cost. We analytically computed the projected correlation function and presented an explicit form for the covariance matrix, which can be calculated numerically and used to fit models to the data. We then applied the method to high-redshift data from SDSS.

We find that this new method can reveal the BAO signal in sparse data. This implies that cross-correlations of spectroscopy and photometry will provide a viable means with which to extend BAO measurements to higher redshifts even before the completion of major future surveys. Of particular interest may be the application of this method to detect the BAO in the clustering of high redshift quasars observed by present and upcoming surveys like the extended Baryon Oscillation Spectroscopic Survey (eBOSS) and the Dark Energy Spectroscopic Instrument (DESI). The eBOSS quasar sample, for example, is expected to have an average $nP = 0.040$ (Zhao et al. 2016) over the redshift range $0.6 < z < 2.2$, which would make this method an effective way to detect the BAO in that sample.

5.7 Acknowledgments

We would like to thank Aaron Bray for providing us with the photometric data files used in this paper and for generating the corresponding random catalog. We additionally thank Lehman Garrison for generating the CAMB power spectrum used to calculate the theoretical BAO curve in Figure 5.1.

This work was supported by U.S. Department of Energy Grant No. DE-SC0013718, and made use of tools from the Python packages NumPy (van der Walt, Colbert, & Varoquaux 2011), SciPy (Oliphant 2007), and Matplotlib (Hunter 2007), and also relied on ROOT (Brun & Rademakers 1997; see also http://root.cern.ch/).

This paper relies on data from SDSS-III. Funding for SDSS-III has been provided by the Alfred P. Sloan Foundation, the Participating Institutions, the National Science Foundation, and the U.S. Department of Energy Office of Science. The SDSS-III web site is http://www.sdss3.org/.

SDSS-III is managed by the Astrophysical Research Consortium for the Participating Institutions of the SDSS-III Collaboration including the University of Arizona, the Brazilian Participation Group, Brookhaven National Laboratory, Carnegie Mellon University, University of Florida, the French Participation Group, the German Participation Group, Harvard University, the Instituto de Astrofisica de Canarias, the Michigan State/Notre Dame/JINA Participation Group, Johns Hopkins University, Lawrence Berkeley National Laboratory, Max Planck Institute for Astrophysics, Max Planck Institute for Extraterrestrial Physics, New Mexico State University, New York University, Ohio State University, Pennsylvania State University, University of

Portsmouth, Princeton University, the Spanish Participation Group, University of Tokyo, University of Utah, Vanderbilt University, University of Virginia, University of Washington, and Yale University.

Chapter 6

Detectability of Local Group Dwarf Galaxy Analogues at High Redshifts

Anna Patej & Abraham Loeb, 2015, *The Astrophysical Journal Letters*, 815, L28

6.1 Introduction

Local Group dwarf galaxies allow investigation into a wide range of astrophysical and cosmological processes; in addition to being representative of the most populous type of galaxy in the universe, their nearness enables detailed investigations of their stellar populations (for a recent overview, see McConnachie 2012). Due to their low masses and typically old stellar populations, many of these dwarfs are believed to have had the majority of their stars produced at early cosmic times and then had further star formation suppressed by reionization at redshifts $z \sim 6 - 10$ (e.g, Bullock et al. 2000; Ricotti & Gnedin 2005; Loeb & Furlanetto 2013). Observational arguments in favor of

this interpretation for some of the dwarfs have been based on their statistical properties (Bovill & Ricotti 2009) and star formation histories (Brown et al. 2014; Weisz et al. 2014; Weisz, Johnson, & Conroy 2014). In this scenario, wherein some of these galaxies formed most of their stars at early cosmic times and are accordingly "fossils" of those times, some of the present-day dwarfs should be similar to their progenitors at higher redshifts.

The advent of optical and infrared space-based telescopes – the *Hubble Space Telescope* (*HST*) and the *Spitzer Space Telescope* – has allowed for the identification of numerous high-redshift ($z \gtrsim 6$) galaxies, whose properties, including their sizes, star formation rates, and masses, have now been examined in detail (e.g., Stark et al. 2009; Labbé et al. 2010; Oesch et al. 2010; Bouwens et al. 2011; Ellis et al. 2013; Ono et al. 2013). However, current observations are missing a population of fainter galaxies that are needed to reionize the universe at these high redshifts (e.g., Alvarez et al. 2012; Finkelstein et al. 2012; Bouwens et al. 2015; Robertson et al. 2015). Discovering some of these fainter galaxies will be within the purview of future observatories like the *James Webb Space Telescope* (*JWST*).

Part of this population of fainter galaxies is likely to consist of the progenitors of galaxies like the Local Group dwarfs. Boylan-Kolchin et al. (2015) used an analysis of the UV luminosities of the dwarfs to determine that *JWST* should be able to detect progenitors of galaxies like the Large Magellanic Cloud. Here, we compare the physical properties of the local dwarfs and the high-redshift galaxies that have already been detected, and place them in the context of the predicted detection limits for *JWST* to examine the fraction of dwarf progenitors – and thus the fraction of missing light – that may be observable in the near future. Throughout our discussion, we use the standard cosmological parameters $\Omega_m = 0.3$, $\Omega_\Lambda = 0.7$, and $H_0 = 70$ km/s/Mpc.

6.2 Data

We obtain data for over 100 local galaxies from McConnachie (2012), including their V band Vega magnitude m_V, half-light radius r, ellipticity ϵ, and average metallicity $\langle$[Fe/H]$\rangle$. To provide direct comparison with the high-redshift data, we convert r_h to the circularized half-light radius, $r_h = r\sqrt{1-\epsilon}$, that is commonly employed. We select only the 87 galaxies that have all these quantities measured in McConnachie (2012), and note in particular that this excludes the Large and Small Magellanic Clouds (LMC and SMC).

We use metallicity as an input to the Flexible Stellar Population Synthesis (FSPS) code (Conroy et al. 2009; Conroy & Gunn 2010) to scale the galaxies back to $z = 6, 7$. Following the results of Weisz et al. (2014), who analyzed the star formation histories (SFHs) of a subsample of 38 of these dwarfs, we remove those galaxies whose SFHs indicate that the majority of their stellar populations were formed later than these redshifts. We keep those whose SFHs are consistent with at least 50% (within errors) of the stars having been formed prior to $z = 6, 7$, as well as all the remaining galaxies from McConnachie (2012) whose SFHs have not yet been measured, for a total of 73 galaxies. We use a delayed tau-model with $\tau = 0.2$ Gyr, which assumes an early starburst such that nearly all the stars we see today already existed at the redshifts of interest. The code also calculates the evolution to $z = 0$, from which we take the predicted V band magnitude and compare it to m_V from McConnachie (2012) to obtain a correction for the stellar mass of each galaxy; we then use these values to correct the $z = 6$, 7 magnitudes since we assume that all the stars we see today were already present at those high redshifts.

The corresponding parameters for observed $z = 6$ and $z = 7$ galaxies are obtained from several sources. The *Spitzer* IRAC 3.6 μm fluxes of a sample of $z \sim 6$ galaxies are based on Gonzalez et al. (2012), and the 4.5 μm fluxes of $z \sim 7$ galaxies are taken from Labbé et al. (2010). We adopt the 2σ lower and upper limits on the fluxes, corrected to S/N = 5, which gives $F_{3.6} = [38.9, 667.0]$ nJy and $F_{4.5} = [13.3, 637.5]$ nJy. Oesch et al. (2010) provides a value of $r_h = 0.7 \pm 0.3$ kpc for detected galaxies at these redshifts, measured from near-infrared observations using *HST*. We again adopt the 2σ bounds on this quantity; accordingly, the range of observed sizes that we use is $0.1 - 1.3$ kpc.

The future *JWST* mission's NIRCam imager will have two filters, F356W and F444W, which will cover the bandwidth of the *Spitzer* filters above. For the purposes of this comparison, we will assume that the *Spitzer* 3.6 μm filter is identical to F356W and the 4.5 μm filter is identical to F444W.

6.3 Comparison of Physical Parameters

We use the FSPS-derived fluxes and the sizes r_h to calculate the surface brightness in Jy/arcsec^2 for the dwarfs at $z = 6$ and $z = 7$. We selected those galaxies with cumulative SFHs $\gtrsim 0.5$ (within the error profile) at early times from Weisz et al. (2014) and used $\tau = 0.2$ Gyr to scale them, as discussed in Section 6.2, as well as all the remaining galaxies that do not have measured SFHs. We additionally plot the region bounded by the 2σ limits on the surface brightness and half-light radius for galaxies detected at $z \sim 6$ and $z \sim 7$, using *Spitzer* 3.6 μm and 4.5 μm fluxes, respectively. Figure 6.1 shows these regions alongside the scaled galaxies selected from Weisz et al. (2014) and the remaining galaxies from McConnachie (2012). From this, we see that virtually none of the local

dwarf analogues have been detected yet.

Nevertheless, the sizes of the dwarfs and the high redshift galaxies agree extremely well, excluding the extreme smallest and faintest objects. However, we do not include in our comparison a scaling of r_h with redshift. Luminous galaxies at higher redshifts have been observed to have their sizes scaled by a factor of $(1+z)^{-s}$, where s is in the range of $1.0-1.5$ (e.g., Oesch et al. 2010; Mosleh et al. 2012). There is some indication, however, that at the lowest luminosities yet studied, the half-light radius remains approximately constant with redshift (see Figure 12 of Ono et al. 2013). Our results are consistent with the notion that the Local Group galaxies had roughly the same size at high redshifts as they have at present.

6.4 Predictions for *JWST*

JWST will rely on the NIRCam imager (Rieke et al. 2005; Beichman et al. 2012) to obtain photometry of high-redshift galaxies. We use the prototype exposure time calculator (ETC) for NIRCam[1] to compute the signal-to-noise ratio for the dwarf galaxies scaled back to high redshifts. We assume a total of 100 hours of exposure time; with such a set-up, the ETC predicts that a point source flux of 1.0 nJy can be detected in F356W and 2.0 nJy in F444W.

We can then calculate the minimum surface brightness for the local galaxy analogues in each band. We assume that, as is currently done with *HST*/*Spitzer* observations of high redshift galaxies, the size of the galaxies is measured from bands at shorter

[1]http://jwstetc.stsci.edu/etc/input/nircam/imaging/

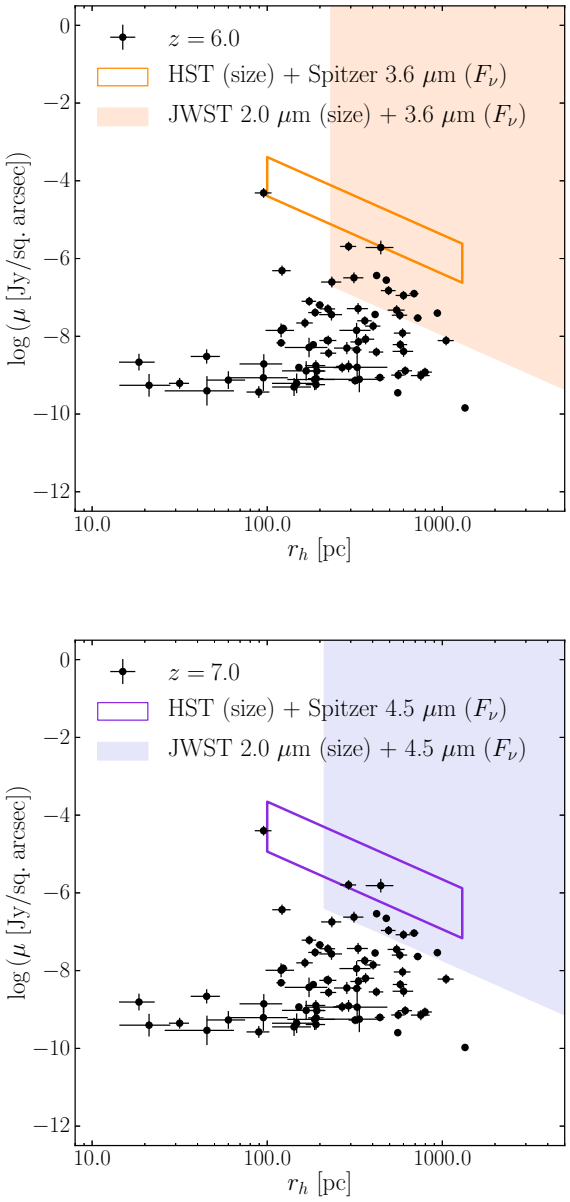

Figure 6.1.—: The surface brightness-size relation for $z \sim 6$ (left) and $z \sim 7$ (right) galaxies using *Spitzer* 3.6 μm and 4.5 μm fluxes, respectively, as well as sizes measured from *HST*. The region bounded by solid lines indicates the portion of the parameter space that has been observed by current programs. The shaded region indicates the part of the parameter space that should be accessible to *JWST*, with the size limit coming the diffraction limited radius in the 2.0 μm filter (see Section 6.4).

wavelengths. Accordingly, in Figure 6.1, we also plot a shaded region bounded by the diffraction-limited radius in the 2.0 μm filter at these redshifts and by the surface brightness corresponding to the S/N=5 fluxes calculated by the ETC. We caution, however, that when comparing the sizes care must be taken, as the data for the galaxies uses the half-light radius, whereas the minimum size prediction for *JWST* is given by the radius of a high redshift object in the diffraction limit.

From Figure 6.1, we can see that *JWST* can be expected to discover some of the local dwarfs if their stars already formed at early cosmic times. In particular, we predict that roughly 60-65% of the combined light of this subsample of dwarfs (corresponding to a detection of 9/73 dwarfs at 4.5 μm and 13/73 dwarfs at 3.6 μm) will be accessible to *JWST*. However, due to the selection criteria we imposed in Section 6.2, some of the brightest dwarf galaxies in the Local Volume were omitted from our analysis, including the Magellanic Clouds and Fornax; if such galaxies were able to be captured by our procedure, these fractions could be higher. This differs from Boylan-Kolchin et al. (2015) primarily due to our uniform assumption that the galaxies we analyze formed most of their stars at very early times. If it is the case that significant star formation occurs late in the galaxy's evolution, then there will not be enough light emitted to render the galaxy detectable even by *JWST*. Accordingly, the predicted fluxes will need to be scaled by the fraction of stars formed by $z \sim 6, 7$ once more of the galaxies have their star formation histories analyzed.

We can compare some of our results for individual galaxies directly to the predictions of Boylan-Kolchin et al. (2015) in their Figure 4, which shows the predicted detectability at $z \sim 7$ of a few Local Group dwarfs from the UV luminosity function. None of the galaxies from McConnachie (2012) whose progenitors we predict to be detectable at

$z \sim 7$ are included in the sample of Boylan-Kolchin et al. (2015). Of the dwarfs that Boylan-Kolchin et al. (2015) studied, our analysis includes Canes Venatici I, Draco, Leo T, Sculptor, and Ursa Minor; the remainder of their dwarfs were excluded in our analysis due to their incompatible SFHs or lack of required r_h or m_V data. We find that the progenitors of these galaxies are not expected to be detectable at high redshifts by *JWST*, which agrees with the predictions of Boylan-Kolchin et al. (2015).

6.5 Additional Prospects

Our calculated fluxes are predicated upon the assumption that the stellar populations of the $z = 0$ dwarfs are the modern analogues of the stars at $z \sim 6 - 7$. However, these stars may be supplemented by PopIII-like stars, which are predicted to have masses in the range $10 - 1000 M_{\odot}$ and short lifetimes (Abel, Bryan, & Norman 2002; Prescott et al. 2009; Cassata et al. 2013; Loeb & Furlanetto 2013; Sobral et al. 2015). Accordingly, in Figure 6.2 we consider the scenario in which the dwarf galaxies are 10 times more luminous at high redshifts due to an ancient population of stars that no longer exists, which would represent extremely optimistic prospects for detectability.

In this case, we find that some of the dwarf progenitors could be among the galaxies already found with *HST* and *Spitzer*. The fraction of the light of the sample of dwarfs considered here that would potentially be detectable by *JWST* would increase to $\sim$67%. This scenario can be distinguished from the fiducial one based on spectroscopy; several theoretical works have indicated that such a massive stars would have strong helium line emission, which would distinguish these stellar populations (Bromm et al. 2001; Tumlinson at al. 2001; Schaerer 2003). However, this is a highly optimistic estimate,

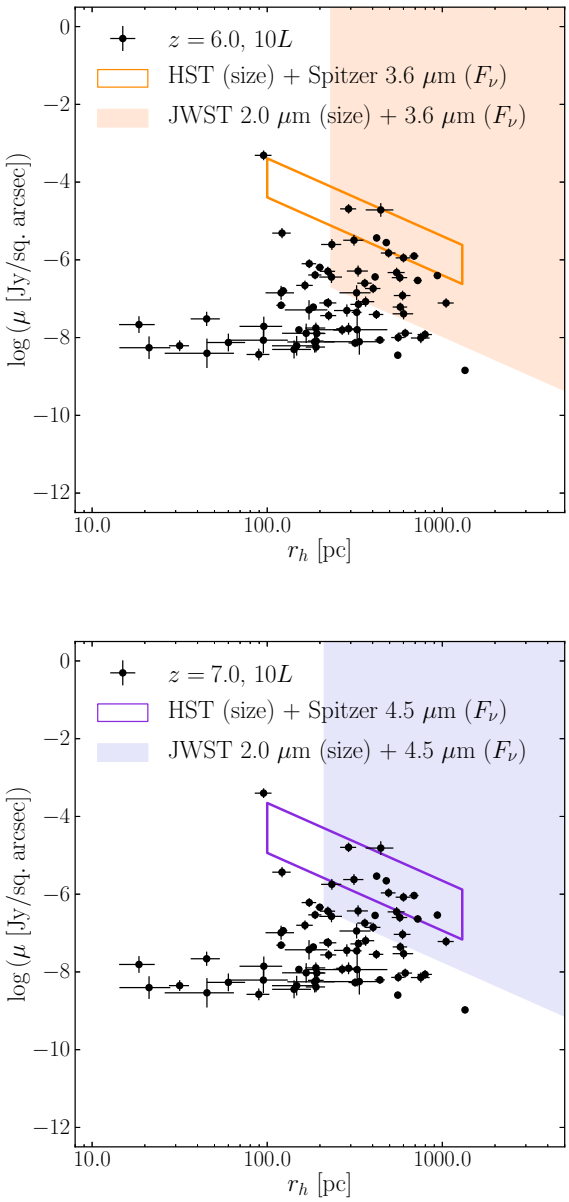

Figure 6.2.—: Same as Figure 6.1, but assuming the ancient stars were 10 times more luminous than those in the dwarfs today.

considering that it would require dominance of Population III stars at these redshifts.

An alternative source of an increase in surface brightness at early times may be provided by tidal stripping. The simulations of Peñarrubia, Navarro, & McConnachie (2008) illustrate the effect of tidal stripping on dwarf galaxies by massive halos. This effect decreases both the sizes and surface brightnesses of the dwarf galaxies. If tidal stripping has affected some of the dwarfs, then it is likely that at higher redshifts they were both brighter and larger, which would make the analogues of these galaxies more likely to be detectable, although observations suggest that that the population of dwarfs significantly affected is small (e.g., Kirby et al. 2013).

In addition to the enhanced capabilities of *JWST* relative to *HST* and *Spitzer*, we note that further gains in sensitivity can be made using gravitational lensing (Mashian & Loeb 2013; Atek et al. 2015). Lensing has already permitted the discovery of high redshift galaxies even smaller than the sizes considered here (e.g., Kawamata et al. 2015); this technique using *JWST* is likely to be able to probe a larger sample of dwarf progenitors.

6.6 Conclusions

We have compared the physical properties of Local Group dwarf galaxies to high-redshift galaxies. We find that the sizes of the two populations agree very well, but when translated to higher redshifts, these dwarfs are too faint to be detected at present. However, in a deep field, the upcoming *JWST* mission should be able to detect analogues of the brightest of these objects, assuming that their stars formed early. The number of

detectable galaxies increases if we assume a population of ancient, massive stars in these galaxies at high redshifts; spectroscopy and number counts will enable us to distinguish these two scenarios. Additionally, gravitational lensing and the effects of tidal stripping can amplify the potential for analogues of these galaxies to be detected at high redshifts.

6.7 Acknowledgments

We would like to thank Charlie Conroy and Matt Walker for helpful comments on a draft of this paper. We are also grateful to Charlie Conroy for useful discussions regarding the FSPS code.

This work was supported by the National Science Foundation Graduate Research Fellowship under Grant No. DGE-1144152 and by NSF Grant No. AST-1312034.

This analysis made use of NumPy (van der Walt, Colbert, & Varoquaux 2011) and Matplotlib (Hunter 2007).

Chapter 7

Conclusions and Future Endeavors

In this thesis, we have broadly addressed distributions of baryonic matter in three distinct regimes: cluster scales, large scales, and at the extremes of the universe – the nearby Local Group and the most distant galaxies ever discovered. In the first two chapters after the introduction, we focused on the outskirts of galaxy clusters, the current frontier in galaxy cluster astrophysics. In Chapters 4 and 5, we moved from the small scales of clusters to large scales, where the distributions of galaxies provide a competitive cosmological probe in the form of the BAO method. Lastly, in Chapter 6, we considered the detectability of the progenitors of the Local Group dwarf galaxies at high redshifts with *JWST*.

More specifically, in Chapter 2, we described a new model for galaxy cluster gas profiles that is derived from only a few simple physical and cosmological conditions on galaxy clusters, including the predictions of a virial shock on the outskirts of the gas profile and a corresponding steep dark matter jump. We found that our model compares well with observations of the interior regions of galaxy clusters in spite of its simplicity.

After the publication of this work, Lau et al. (2015) also found good agreement between the results of their simulations of the gas and dark matter behavior in the cluster outskirts and the predictions of our model. However, the predictions for the outskirts remain to be tested observationally, as the virial shock has yet to be detected. Deep *Chandra* imaging now exists of the outskirts of Abell 133 and 1795 (Vikhlinin et al. in prep), which may yield hints of this feature. Future work can attempt to extend our model by incorporating additional physics of galaxy cluster gas.

In Chapter 3, we addressed the existence of steep density jumps in cluster outskirts, which are longstanding predictions of analytical models of structure formation and recent simulations. Under the assumption that the cluster member galaxies follow similar collisionless dynamics as the dark matter, the cluster member distribution should show a steep density jump as well. We constructed the projected cluster member number density profiles of a sample of 58 galaxy clusters using a combination of photometry and spectroscopy and fit them with two profiles, one that includes a density jump and one without. We find that some of the clusters do strongly prefer the model that includes the density jump, providing substantial evidence in favor of the existence of the jump.

However, we found that the strength of the signal increases with the security of the cluster member identification, highlighting the need for additional spectroscopy of the cluster outskirts to constrain the location and amplitude of the feature. With these estimates, the density jump could be used as a physically-motivated indicator of galaxy cluster size (e.g., More, Diemer, & Kravtsov 2015) and moreover provide an important test of the common assumption that the individual cluster galaxies in the outskirts are collisionless.

In Chapter 4, we tested whether red and blue galaxies trace the same large-scale structure. We found that this is indeed the case, detecting only minute amounts of stochasticity on intermediate scales, which constrains a key systematic in using galaxy redshift surveys for cosmology. Additionally, we established the utility of the smooth Xu et al. (2010) statistic in analyzing the stochasticity.

In Chapter 5, we described a new method of detecting the BAO in sparse spectroscopic data sets. Our method uses the cross-correlation of the spectroscopic sample with a much denser photometric sample of galaxies to enhance the BAO signal. We detected the BAO signal using this method with sparse $z > 0.6$ SDSS CMASS galaxy data and dense SDSS photometry. This approach will prove useful for future work attempting to measure the BAO at high redshifts, particularly using quasar and OIII emitter samples from DESI and Euclid, respectively.

Lastly, in Chapter 6, we compared the properties of the Local Group dwarf galaxies and the high redshift galaxies discovered using *Hubble* and *Spitzer*. We verified that the progenitors of the dwarfs are too faint to have been discovered by these present observatories, but that the upcoming *JWST* will have slightly better prospects, and should be able to detect the progenitors of a handful of the brightest local galaxies.

Accordingly, in tracing the distributions of baryons from the small scales of galaxy clusters to the large scales of filaments and voids and beyond in this thesis, we have pushed the limits of available datasets. We explored the topic of density jumps in galaxy clusters, which have only recently begun to be probed in detail due to the difficulty of observing and simulating the outskirts where these features are predicted to appear. On large scales, we proposed a new method for obtaining useful BAO measurements when

datasets are sparse, as with high redshift quasars. We also considered the potential of a future observatory to detect small and faint galaxies at very high redshifts that current observatories cannot probe. These investigations all point towards an exciting near-term future in astrophysics, as upcoming datasets are likely to empower innovative inroads into these questions.

References

Abel, T., Bryan, G. L., & Norman, M. L. 2002, Science, 295, 93

Abell, G. O. 1958, ApJS, 3, 211

Ade, P. A. R. et al. (Planck Collaboration), 2015, arXiv: 1502.01589

Adhikari, S., Dalal, N., & Chamberlain, R. T. 2014, JCAP, 11, 019

Ahn, C. P., et al. 2012, ApJS, 203, 21

Akaike, H. 1974, IEEE Transactions on Automatic Control, 19, 716

Alam, S., et al. 2015, ApJS, 219, 12

Allen, S. W., Evrard, A. E., & Mantz, A. B. 2011, ARA&A, 49, 409

Alvarez, M. A., Finlator, K., & Trenti, M. 2012, ApJL, 759, L38

Anderson, L., et al. 2012, MNRAS, 427, 3435

Anderson, L., et al. 2014, MNRAS, 441, 24

Ascasibar, Y., & Diego, J. M. 2008, MNRAS, 383, 369

Atek, H., et al. 2015, arXiv:1509.06764

Bahcall, N. A., & Kulier, A. 2014, MNRAS, 439, 2505

Bardeen, J. M., et al. 1986, ApJ, 304, 15

Becker, M. R., & Kravtsov, A. V. 2011, ApJ, 740, 25

Beichman, C. A., et al. 2012, SPIE, 8442, 2

Bertschinger, E. 1985, ApJS, 58, 39

Blanton, M. 2000, ApJ, 544, 63

Bleem, L., et al. 2015, ApJS, 216, 27

Bolton, A. S., et al. 2012, AJ, 144, 144

de Boor, C. 2001, A Practical Guide to Splines, Revised Edition (New York: Springer-Verlag)

Bouwens, R. J., et al. 2011, ApJ, 737, 90

Bouwens, R. J., et al. 2015, arXiv:1503.08228

Bovill, M. S. & Ricotti, M. 2009, ApJ, 693, 1859

Boylan-Kolchin, M., et al. 2015, MNRAS, 453, 1503

Broderick, A., et al. 2011, ApJ, 735, 110

Bromm, V., Kudritzki, R. P., Loeb, A. 2001, ApJ, 552, 464

Brown, T. M., et al. 2014, ApJ, 796, 91

Brun, R., & Rademakers, F. 1997, Nucl. Inst. & Meth. in Phys. Res. A, 389, 81

Bryan, G. L, & Norman, M. L. 1998, ApJ, 495, 80

Budzynski, J. M., et al. 2012, MNRAS, 423, 104

Bulbul, G. E., et al. 2010, ApJ, 720, 1038

Bullock, J. S., Kravtsov, A. V., & Weinberg, D. H. 2000, ApJ, 539, 517

Burnham, K. P., & Anderson, D. R. 2002, Model Selection and Multimodal Inference (Springer-Verlag, New York)

Burnham, K. P., & Anderson, D. R. 2004, Sociol. Method. Res., 33, 261

Carlstrom, J. E., Holder, G. P., & Reese, E. D. 2002, ARA&A, 40, 643

Cassata, P., et al. 2013, A&A, 556, 68

Cavaliere, A. G., Gursky, H., & Tucker, W. H. 1971, Nature, 231, 437

Cavaliere, A., & Fusco-Femiano, R. 1976, A&A, 49, 137

Cavaliere, A., Menci, N., & Tozzi, P. 1997, ApJ, 484, 21

Coil, A. L., et al. 2008, ApJ, 672, 153

Cole, S., et al. 2005, MNRAS, 362, 505

Coles, P. 1993, MNRAS, 262, 1065

Colless, M., et al. 2001, MNRAS, 328, 1039

Conroy, C., Gunn, J., & White, M. 2009, ApJ, 699, 486

Conroy, C. & Gunn, J. 2010, ApJ, 712, 833

Croton, D. J., Norberg, P., Gaztañaga, E., & Baugh, C. M. 2007, MNRAS, 379, 1562

Davis, M., Efstathiou, G., Frenk, C. S., & White, S. D. M. 1985, ApJ, 292, 371

Dawson, K. S., et al. 2013, AJ, 145, 10

Dawson, K. S., et al. 2016, AJ, 151, 44

Dekel, A., & Lahav, O. 1999, ApJ, 520, 24

Diemer, B., & Kravtsov, A. V. 2014, ApJ, 789, 1

Doi, M., et al. 2010, AJ, 139, 1628

Dressler, A. 1980, ApJ, 236, 351

Einasto, J. 1965, TrAlm, 5, 87

Eisenstein, D., & Hu, W. 1998, ApJ, 496, 605

Eisenstein, D. J., et al. 2005, ApJ, 633, 560

Eisenstein, D. J., et al. 2011, AJ, 142, 72

Ellis, R., et al. 2013, ApJ, 763, 7

Ettori, S., et al. 2013, SSRv, 177, 119

Ferrer, D., et al. in prep.

Fillmore, J. A., & Goldreich, P. 1984, ApJ, 281, 1

Finkelstein, S. L., et al. 2012, ApJ, 758, 2

Fukugita, M. et al. 1996, AJ, 111, 1748

Geller, M. J., & Huchra, J. P. 1989, Science, 246, 897

Gladders, M. D., & Yee, H. K. C. 2000, AJ, 120, 2148

Gonzalez, V., et al. 2012, ApJ, 755, 148

Gunn, J. E., et al. 1998, AJ, 116, 3040

Gunn, J. E., et al. 2006, AJ, 131, 2332

Guo, H., et al. 2013, ApJ, 767, 122

Gruen, D., et al. 2014, MNRAS, 442, 1507

Gursky, H., et al. 1971, ApJ, 167, 81

Haines, C. P., et al., 2013, ApJ, 775, 126

Hamaus, N., et al. 2010, PhRvD, 82, 043515

Hansen, S. M., et al. 2005, ApJ, 633, 122

Hao, J., et al. 2010, ApJS, 191, 254

Hasselfield, M., et al. 2013, JCAP, 07, 008

Hoekstra, H., et al. 2012, MNRAS, 427, 1298

Hunter, J. D. 2007, Computing in Science & Engineering, 9, 90

Just, D. W., et al. 2015, arXiv: 1506.02051

Kaiser, N. 1984, ApJ, 284, 9

Karachentsev, I. D., et al. 2014, ApJ, 782, 4

Kawamata, R., et al. 2015, ApJ, 804, 103

Kirby, E. N., et al. 2013, ApJ, 779, 102

Kocsis, B., Haiman, Z., & Frei, Z. 2005, ApJ, 623, 632

Kravtsov, A. V., & Borgani, S. 2012, ARA&A, 50, 353

Kubo, J. M., et al. 2007, ApJ, 671, 1466

Labbé, I., et al. 2010, ApJL, 716, 103

Landau, L., & Lifshitz, E. 1987, Course of Theoretical Physics, Vol. 6: Fluid Mechanics (New York)

Landy, S. D., & Szalay, A. S. 1993, ApJ, 412, 64

Lau, E. T., et al. 2015, ApJ, 806, 68

Leccardi, A., & Molendi, S. 2008, A&A, 486, 359

Levi, M., et al. (DESI Collaboration), 2013, arXiv: 1308:0847

Lewis, A., Challinor, A., & Lasenby, A. 2000, ApJ, 538, 473

Liddle, A. R. 2007, MNRAS, 377, L74

Lin, Y-T., Mohr, J. J., & Stanford, S. A. 2004, ApJ, 610, 745

Loeb, A., & Furlanetto, S. R. 2013, The First Galaxies in the Universe (Princeton University Press)

Ludlow, A. D., et al. 2013, MNRAS, 432, 1103

Lupton, R., Gunn, J.E., Ivezic, Z., Knapp, G., & Kent, S. 2001, Astronomical Data Analysis Software and Systems X, v.238, 269

Mahdavi, A., et al. 2013, ApJ, 767, 116

Martino, R., et al. 2014, MNRAS, 443, 2342

Mashian, N., & Loeb, A. 2013, JCAP, 12, 017

Masters, K. L. et al. 2011, MNRAS, 418, 1055

McConnachie, A.W., 2012, AJ, 144, 4

Mehrtens, N., et al. 2012, MNRAS, 423, 1024

Metchnik, M., & Pinto, P. in prep.

Miyazaki, S., et al. 2007, ApJ, 669, 714

Mohr, J., Mathiesen, B., & Evrard, A. 1999, ApJ, 517, 627

Montero-Dorta, A. D., & Prada, F. 2009, MNRAS, 399, 1106

Moore, B., et al. 1999, MNRAS, 310, 1147

More, S., Diemer, B., & Kravtsov, A. 2015, arXiv: 1504.05591

Mosleh, M., et al. 2012, ApJ, 756, 12

Navarro, J. F., Frenk, C. S., & White, S. D. M. 1997, ApJ, 490, 493

Newman, A. B., et al. 2013, ApJ, 765, 25

Nuza, S. E., et al. 2013, MNRAS, 432, 743

Oesch, P. A., et al. 2010, ApJ, 709, 21

Oguri, M., et al. 2009, ApJ, 699, 1038

Oliphant, T. E. 2007, Computing in Science & Engineering, 9, 10

Ono, Y., et al. 2013, ApJ, 777, 155

Ostriker, J. P., Bode, P., & Babul, A. 2005, ApJ, 634, 964

Padmanabhan, N., White, M., & Eisenstein, D. J. 2007, MNRAS, 376, 1702

Padmanabhan, N., et al. 2008, ApJ, 674, 1217

Peñarrubia, J., Navarro, J. F., & McConnachie, A. W. 2008, ApJ, 673, 226

Pier, J. R., et al. 2003, AJ, 125, 1559

Piffaretti, R., et al. 2011, A&A, 534, 109

Pointecouteau, E., et al. 2004, A&A, 423, 33

Pratt, G. W., et al. 2007, A&A, 461, 71

Prescott, M. K. M, Dey, A., Jannuzi, B. T. 2009, ApJ, 702, 554

Press, W. H., & Schechter, P. 1974, ApJ, 187, 425

Reid, B., et al. 2015, arXiv:1509.06529

Reinsch, C. H. 1967, Numerische Mathematik 10, 177

Retana-Montenegro, E., et al. 2012, A&A, 540, 70

Richard, J., et al. 2009, A&A, 498, 37

Ricotti, M., & Gnedin, N. Y. 2005, ApJ, 629, 259

Rieke, M. J., Kelly, D., & Horner, S. 2005, SPIE 5904, 1

Reiprich, et al., 2013, SSRv, 177, 195

Rines, K., et al. 2013, ApJ, 767, 15, 2013

Robertson, B. E., Ellis, R. S., Furlanetto, S. R., & Dunlop, J. S. 2015, ApJL, 802, L19

Ross, A. J., et al. 2014, MNRAS, 437, 1109

Rykoff, E. S., et al. 2014, ApJ, 785, 104

Saha, P., & Read, J. I. 2009, ApJ, 690, 154

Schaal, K. & Springel, V. 2015, MNRAS, 446, 3992

Schaerer, D. 2003, A&A, 397, 527

Schaller, M., et al. 2014, arXiv: 1409.8297

Scherrer, R. J., & Weinberg, D. H. 1998, ApJ, 504, 607

Schlegel, D. J., Finkbeiner, D. P., & Davis, M. 1998, ApJ, 500, 525

Schwarz, G. 1978, The Annals of Statistics, 6, 461

Seljak, U., & Warren, M. S. 2004, MNRAS, 355,129

Skibba, R. A., et al. 2014, ApJ, 784, 128

Smee, S. A., et al. 2013, AJ, 146, 32

Smith, J. A., et al. 2002, AJ, 123, 2121

Sobral, D., et al. 2015, ApJ, 808, 139

Stark, D. P., et al. 2009, ApJ, 697, 1493

Sunyaev, R. A., & Zel'dovich, Y. B. 1972, CoASP, 4, 173

Suzuki N. et al., 2012, ApJ, 746, 85S

Swanson, M. E. C., Tegmark, M., Blanton, M., & Zehavi, I. 2008, MNRAS, 385, 1635

Takeuchi, T. T. 2000, Ap&SS, 271, 213

Tan, M. Y. J., & Biswas, R. 2012, MNRAS, 419, 3292

Tegmark, M. & Bromley, B. C. 1999, ApJL, 518, L69

Trentham, N., & Tully, R.B. 2009, MNRAS, 398, 722

Tully, R. B. 2010, arXiv: 1010.3787

Tully, R. B. 2015, arXiv: 1503.03134

Tumlinson, J., Giroux, M. L., & Shull, J. M. 2001, ApJ, 550, 1

Vikhlinin, A., et al. 2005, ApJ, 628, 655

Vikhlinin, A., et al. 2006, ApJ, 640, 691

Vikhlinin, A., et al. 2009a, ApJ, 692, 1033

Vikhlinin, A., et al. 2009b, ApJ, 692, 1060

Voges, W., et al. 1999, A&A, 349, 389

Voit, G. M. 2005, Rev. Mod. Phys., 77, 207

van der Walt, S., Colbert, S. C., & Varoquaux, G. 2011, Computing in Science & Engineering, 13, 22

Wang, Y., Yang, X., Mo, H. J., van den Bosch, F. C. 2007, ApJ, 664, 608

Weaver, B., et al. 2015, PASP, 127, 397

Weinberg, D. H., et al. 2013, PhR, 530, 87

Weisz, D. R., et al. 2014, ApJ, 789, 148

Weisz, D. R., Johnson, B. D., & Conroy, C. 2014, ApJL, 794, L3

Wild, V., et al. 2005, MNRAS, 356, 247

Wittman, D., et al. 2006, ApJ, 643, 128

Wright, C. O., & Brainerd, T. G. 2000, ApJ, 534, 34

Xu, X., et al. 2010, ApJ, 718, 1224

York, D. G., et al. 2000, AJ, 120, 1579

Zehavi, I., et al. 2005, ApJ, 621, 22

Zehavi, I., et al. 2011, ApJ, 736, 59

Zhao, G-B., et al. 2016, MNRAS, 457, 2377